AD-A121 322 ARAP'S SECOND-ORDER CLOSURE MODEL: COMPARISON WITH A NUMBER OF COMPLEX TU..(U) AERONAUTICAL RESEARCH ASSOCIATES OF PRINCETON INC NJ W S KEWELLEN ET AL. 1/2

UNCLASSIFIED APR 82 ARAP-469 AFOSR-TR-82-0970 F/G 20/4 NL

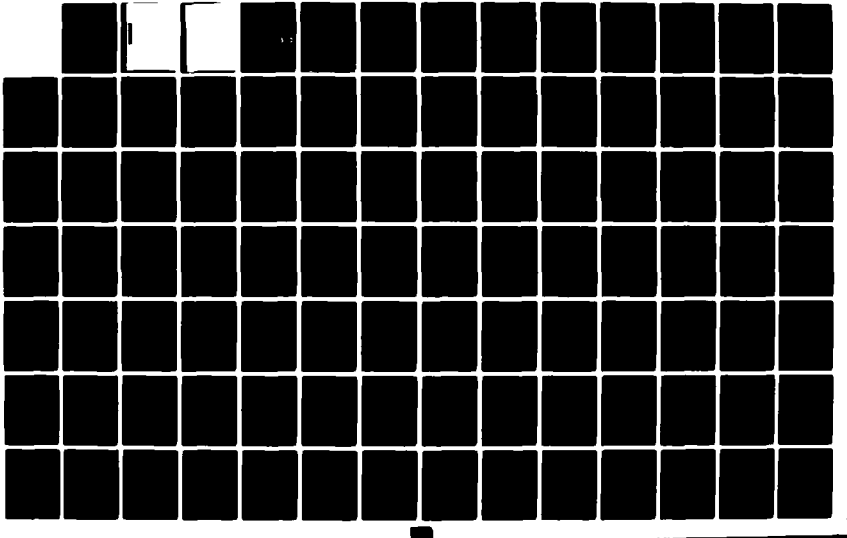

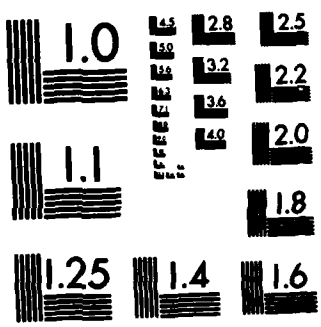

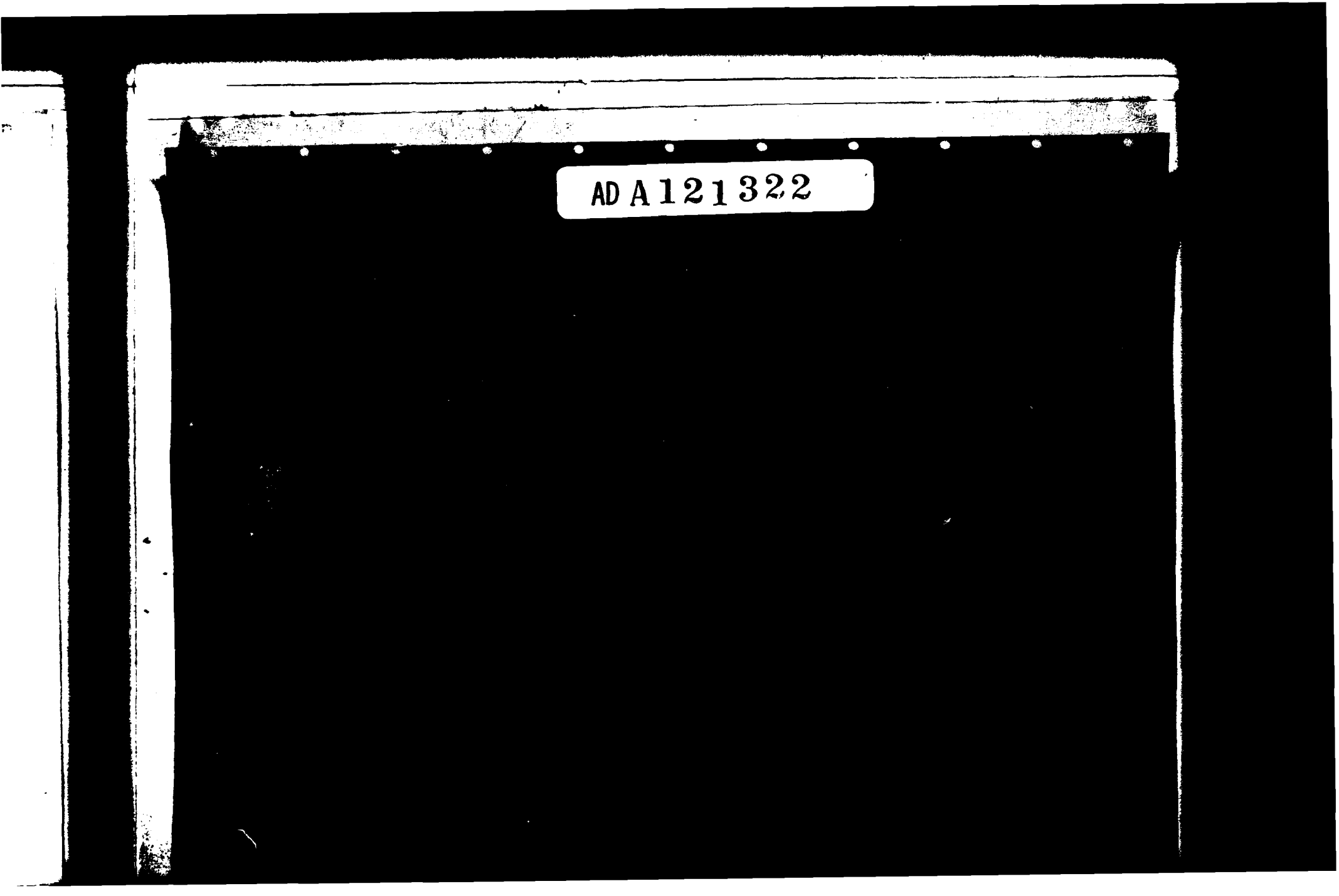

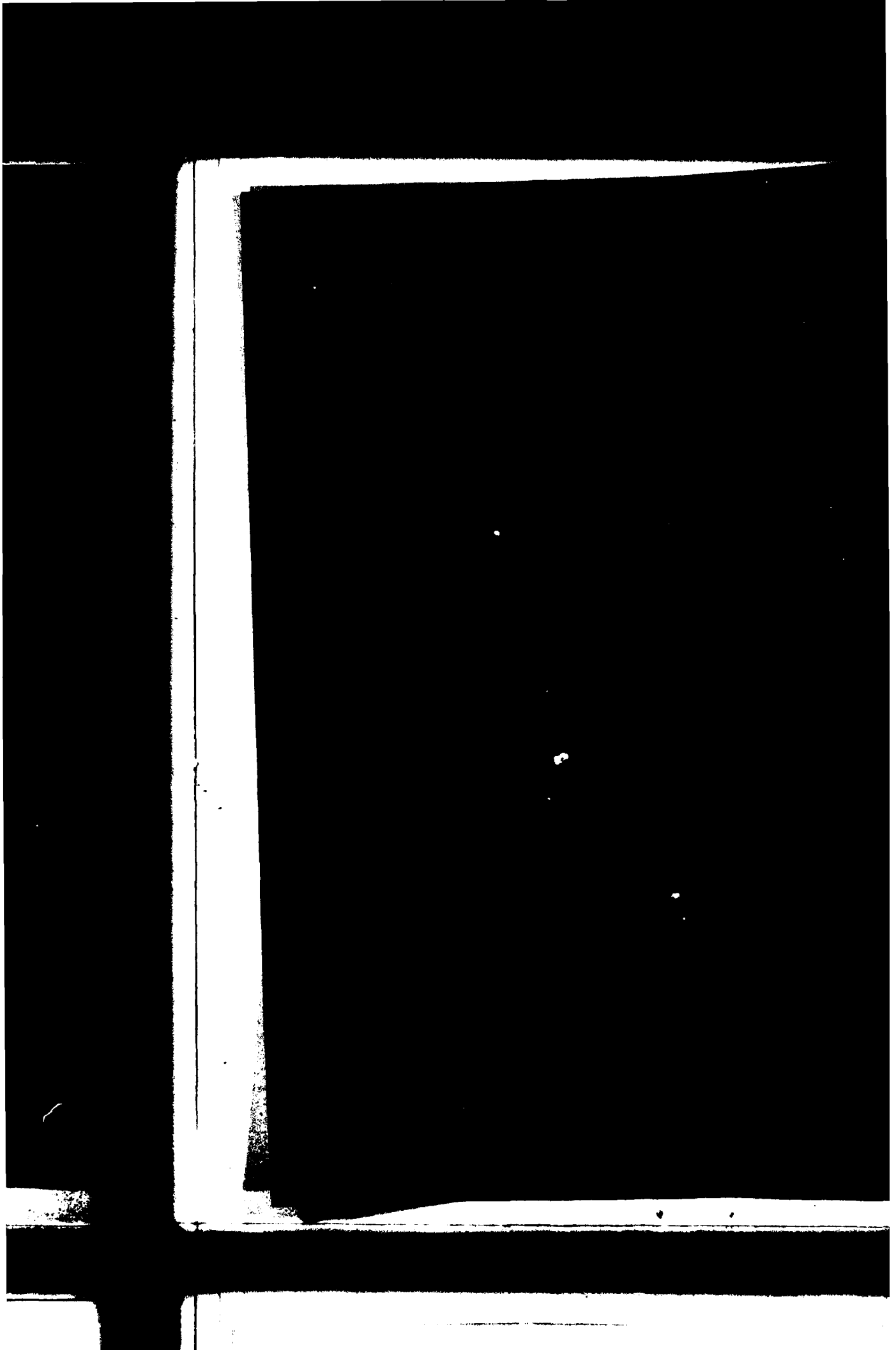

Unclassified

SECURITY CLASSIFICATION OF THIS PAGE (When Data Entered)

REPORT DOCUMENTATION PAGE		READ INSTRUCTIONS BEFORE COMPLETING FORM
1. REPORT NUMBER AFOSR-TR- 82-0970	2. GOVT ACCESSION NO. A121322	3. RECIPIENT'S CATALOG NUMBER
4. TITLE (and Subtitle) A.R.A.P.'s Second-Order-Closure Model: Comparison With a Number of Complex Turbulent Flows		5. TYPE OF REPORT & PERIOD COVERED Scientific Report 1 Mar 1981 - 30 Apr 1982 6. PERFORMING ORG. REPORT NUMBER A.R.A.P. Report No. 469
7. AUTHOR(s) Coleman duP. Donaldson, W. Stephen Lewellen, Brian Quinn, Roger D. Sullivan, R. Ian Sykes, and Ashok K. Varma		8. CONTRACT OR GRANT NUMBER(s) F49620-81-C-0057
9. PERFORMING ORGANIZATION NAME AND ADDRESS Aeronautical Research Associates of Princeton, Inc. 50 Washington Road, P.O. Box 2229 Princeton, New Jersey 08540		10. PROGRAM ELEMENT, PROJECT, TASK AREA & WORK UNIT NUMBERS 61102F 2307/A2
11. CONTROLLING OFFICE NAME AND ADDRESS Air Force Office of Scientific Research/NA Bldg. 410 Bolling Air Force Base, DC 20332		12. REPORT DATE April 1982 13. NUMBER OF PAGES 104
14. MONITORING AGENCY NAME & ADDRESS(if different from Controlling Office)		15. SECURITY CLASS. (of this report) Unclassified 15a. DECLASSIFICATION/DOWNGRADING SCHEDULE

16. DISTRIBUTION STATEMENT (of this Report)

Approved for public release; distribution unlimited.

17. DISTRIBUTION STATEMENT (of the abstract entered in Block 20, if different from Report)

18. SUPPLEMENTARY NOTES

19. KEY WORDS (Continue on reverse side if necessary and identify by blo

20. ABSTRACT (Continue on reverse side if necessary and identify by block number)

The flows computed by A.R.A.P. for the AFOSR-HTTM-Stanford Conference on Complex Turbulent Flows are reviewed and discussed. Eighteen different flows were simulated using A.R.A.P.'s full Reynolds stress model. These flows ranged in complexity from simple homogeneous decay to fully elliptic, unsteady flows behind a backward facing step. The results are generally quite good, demonstrating that a wide range of problems can be handled by Reynolds stress closure models. However, there are some notable exceptions. The

cont

DD FORM 1 JAN 73 1473 EDITION OF 1 NOV 65 IS OBSOLETE

Unclassified

SECURITY CLASSIFICATION OF THIS PAGE (When Data Entered)

cont → probable reasons for the discrepancies are indicated and directions for model improvements are suggested.

TABLE OF CONTENTS

1. INTRODUCTION

In the course of the last dozen years, A.R.A.P. has frequently been faced with the need to make predictive computations of turbulent flows in regimes for which physical understanding was sketchy. Examples (Donaldson[1], Lewellen[2]) include flows in the atmosphere with temperature and humidity gradients and flows in the ocean with temperature and salinity gradients. Thus we have tried to make a turbulence model as general as possible, without unduly sacrificing simplicity, by using Reynolds stress closure. Another goal has been to design the model so that it collapses to simpler models for flows that can be adequately treated thereby.

Our codes can be expected to produce accurate results for flows with scales that are not of greatly disparate size in different directions and for which the turbulent spectra are similar and can be described by two parameters, an integral scale and a dissipative scale. Our current research is directed toward developing equations for a tensor of second rank, called the scale tensor, derived from the two-point correlation equations. (If correlations of a scalar with the velocity are also involved in the flow, there is, in addition, a scale vector to be considered.) We believe that the use of such equations in conjunction with suitably modified Reynolds stress closure equations would give results applicable to an even wider class of flows since such equations contain information about eddy structure.

In making computations for the AFOSR-HTTM-Stanford Conference on Complex Turbulent Flows we used operational codes to calculate a variety of turbulent flows in order to demonstrate their generality. The 18 cases represent a compromise between this desire for a broad verification set and the necessity of keeping costs in line. They range from the simple homogeneous flows to the true predictive case of the flow downstream of a backward facing step with the wall opposite the step at a 6^{o} angle. Five of the cases are compressible, the rest incompressible.

We used two main programs for our computations: ARB (Sullivan and Varma[3], Sullivan[4]) and WAKE (Hirsh[5]). They both use the same Reynolds stress modeling (Lewellen[2]) (except that ARB has additional modeling for terms that occur only in compressible flow) with the same values of the coefficients. However, the turbulence scale, Λ, is computed differently. ARB uses an

algebraic formula, while WAKE uses a differential equation to determine Λ. We recognize that any such differential equation with constant coefficients cannot be correct (Donaldson and Sandri[6]). Nevertheless such equations are more useful than one might expect in much the same way that eddy viscosity is a much more useful concept than one might expect.

As programs, ARB and WAKE differ considerably in that ARB is parabolic with one space dimension and is used only for boundary layers, whereas WAKE is parabolic with two space dimensions and is used for three-dimensional flows or time-dependent two-dimensional flows. Thus WAKE can handle two-dimensional elliptic problems. The boundary layers that ARB computes can be on flat plates or bodies of revolution with an arbitrary distribution of cross-sectional area (the body can be rotating or not). A variation of ARB called RSL has no provision for rotating bodies, but can do unbounded shear layers as well as boundary layers. (RSL also has provision for calculating multi-species reacting flows.) RSL was used in this project only for Case 0311 (mixing layer).

Another difference between the two programs involves wall conditions: ARB computes all the way to the wall with no special provision except that the formula for Λ makes it proportional to the distance from the wall when that distance is small, whereas WAKE uses the law of the wall to establish boundary conditions some distance off the wall.

WAKE was used to compute Cases 0421 and 0422 (P2). These separated flows have been calculated as elliptic, unsteady flows. The flow is free to develop two-dimensional unsteady eddies which are resolved by the computation. The influence of the smaller three-dimensional turbulence is incorporated by the turbulence closure model.

The homogeneous cases were done by an ordinary differential equation solver using the equations to which the WAKE equations reduce under those conditions.

In the classification scheme set up for the conference, the method descriptor for ARB is RSTN where RS indicates one-point Reynolds stress closure, T indicates no additional differential equation, and N indicates a no-slip condition at the wall with no modification of the equations at or near the wall. For the RSL program (used for the mixing layer) the descriptor is

RSTC where C indicates that a designation of the wall treatment is not relevant. The descriptor for WAKE is RSLZ where L indicates an extra differential equation for the scale and Z indicates that the law of the wall is used, without special treatment, near a wall. The descriptor for the ordinary differential equation version of WAKE, used for the homogeneous cases, is RSLC.

2. DESCRIPTION OF CASES AND RESULTS

The Table lists the cases we did along with the method descriptors, the approximate value of y^+ for the first point off the wall, the approximate number of mesh points, and the approximate CPU computing time on a VAX 11/780.

Many of the cases lacked sufficient data on the initial conditions to show Reynolds stress modeling to good advantage. Nevertheless the results were generally as good as or better than those submitted by others. Figures 1-80 are reproductions of the plots submitted to the conference. Open symbols represent experimental data; the computed results are indicated by plus signs, in some cases with curves faired through them. The 18 cases and the figures belonging to them are discussed below in related groups.

2.1 Incompressible Boundary Layers

Case 0612 is a standard flat-plate boundary-layer flow. Since this flow was used to establish the values of some of our modeling parameters, we expected good results and as seen in Figures 1-3 that is what we got.

The results for Case 0141, a flat-plate boundary-layer flow with adverse pressure gradient, are shown in Figures 4-7. To get the initial conditions for the ARB run it was necessary to interpolate the experimental mean velocity (as a function of y) between two x stations since in the experiment the turbulence correlations were obtained at a different set of x stations. This extra step illustrates one of the many unforeseen problems that added considerably to the effort expended on this project. Although c_f doesn't drop quite as rapidly as experiment shows (Figure 4) our profile results are quite reasonable.

Case 0241 is a flat-plate boundary-layer flow with blowing. The lack of complete initial conditions is reflected in the initial rapid drop in c_f (Figure 8) but downstream the agreement is very good. On the other hand the profile variables track well right from the start as shown in Figures 9, 10 and 11.

A.R.A.P. Computations for the 1981 Stanford Conference

Case	Short Description	Method Descriptor	y^+	Mesh Points	CPU Time
0141	B.L., $\frac{\partial p}{\partial x} > 0$	RSTN	3	30	3 min
0241	B.L., Blowing	RSTN	1	40	3 min
0242	B.L., $\frac{\partial p}{\partial x} > 0$ Suction	RSTN	1	35	3 min
0244	B.L., Suction	RSTN	2	25	3 min
0311	Mixing Layer	RSTC	-	25	3 min
0371	Homogeneous Isotropic	RSLC	-	-	10 sec
0373	Homogeneous Relaxing	RSLC	-	-	10 sec
0374	Homogeneous Plain Strain	RSLC	-	-	10 sec
0375	Homogeneous Axisym. Strain	RSLC	-	-	10 sec
0376	Homogeneous Shear	RSLC	-	-	10 sec
0421	Back Step	RSLZ	30	40×60	10 hours
0422(P2)	Back Step Predictive	RSLZ	30	40×60	10 hours
0612	Flat Plate B.L.	RSTN	1	40	3 min
8101	Compressible B.L., c_f vs. M	RSTN	1	35	3 min
8201	Compressible B.L., c_f vs. T_w	RSTN	1	35	3 min
8301	Compressible B.L., Blowing $\frac{\partial p}{\partial x} < 0$	RSTN	1	40	3 min
8403	Compressible B.L., $\frac{\partial p}{\partial x} > 0$	RSTN	6	30	3 min
8411	Compressible B.L., $\frac{\partial p}{\partial x} > 0$	RSTN	2	40	3 min

Case 0242 is a flat-plate boundary-layer flow with suction and adverse pressure gradient. Here c_f is about 7% below the experimental values even far downstream (Figure 12). However the momentum balance equation

$$\frac{c_f}{2} = \frac{d\theta}{dx} - \frac{v_w}{u_e} + (\delta^* + 2\theta)\frac{1}{u_e}\frac{du_e}{dx}$$

is in this case dominated by the term $v_w/u_e = -.004$ which has a stated experimental error of ±6%. This same discrepancy is reflected in the plots for momentum and displacement thickness (Figures 13 and 14). However, Figure 15 shows that the velocity profiles are reasonably well computed.

Case 0244 is a group of flat-plate boundary-layer flows with a variety of suction rates. The mean velocity profiles are excellently reproduced as seen in Figure 16, but the velocity correlations shown in Figures 17-19 are not as good.

2.2 Incompressible Shear Layer

Case 0311 is the flow in a planar mixing layer. Figure 20 shows the spread of the layer, L, as a function of distance downstream, x. It is likely that the discrepancy in the rate of increase of L for small x is due to the algebraic scale formulation which doesn't adequately represent the situation near the initial station. Downstream the rate of increase of L matches the data very well.

2.3 Compressible Boundary Layers

Case 8101 consists of a comparison of an empirical correlation of experimental results with computed values of the skin friction as a function of Mach number for the boundary layer on an insulated flat plate. In Figure 21 the solid line gives the empirical correlation while the plus signs show the computed results, which are seen to be somewhat high for the larger Mach numbers. This is perhaps due to the fact that the extension of our Reynolds stress modeling to compressible flow introduces new parameters that might be empirically adjusted. No funding has been acquired to accomplish this task so the coefficients of the new terms have been set equal to the coefficients of similar terms for incompressible flow or set to zero. The recovery factor and

velocity profile for this case are shown in Figures 22 and 23.

Case 8201 consists of a comparison of an empirical correlation of experimental results with computed values of the skin friction as a function of wall temperature for the boundary layer on a flat plate at a Mach number of five. In Figure 24 the solid line gives the empirical correlation while the plus signs show the computed results, which are seen to have considerably less variation over the range of wall temperatures. It should be pointed out that at least some of the experimental data fall well below the correlation known as "Van Driest II" at Tw/Taw = .2 (Hopkins and Inouye[7]) as does our calculation. A velocity profile for this case is shown in Figure 25.

Case 8301 is a supersonic flat-plate boundary-layer flow with blowing and favorable pressure gradient. Suprisingly our group was the only one to submit results for this case before the conference. Our results, as shown in Figures 26, 27 and 28, were comparable to but somewhat better than for Cases 0242 and 0244.

Case 8403 is a supersonic boundary-layer flow on the inside of a cylinder with adverse pressure gradient. Actually it consists of several sub-cases since experimental data were presented for several unit Reynolds numbers for each of several centerbodies producing different pressure gradients. Time and money permitted us to do only two of these sub-cases. The skin friction was somewhat underpredicted as shown in Figures 29 and 30. The computed shape parameter does not show (Figures 31 and 32) the wide variation present in the data, but it can be verified that oblique waves in the supersonic field cause this variation. Thus it is not a boundary-layer phenomenon and so is not reproduced by ARB which is a boundary-layer program. The mean flow was reproduced excellently (Figures 33 and 34) but the turbulence level was generally high (Figures 35-38).

Case 8411 is a supersonic flat-plate boundary-layer flow with adverse pressure gradient. Figure 39 shows a good fit of the calculated coefficient of friction with the experimental results. The calculated momentum thickness, on the other hand, is quite low downstream (Figure 40) although the shape parameter and velocity profiles as shown in Figures 41 and 42 are very good. Assuming there is no problem in the experimental values, this indicates that our calculation of the density distribution is somewhat off.

2.4 Homogeneous Flows

The results for Case 0371, the decay of isotropic turbulence, are shown in Figure 43. Like Case 0612 this flow was used to establish values for some of our parameters so we expected and got good results.

Case 0373 is the return to isotropy after distorting strain. Our results indicate the return is much too rapid in the axisymmetric flows (Figures 44-51). This may be due in part to our neglect of rapid pressure terms which forces a higher coefficient on the Rotta terms. However, some of the flows return so slowly that the inclusion of rapid strain terms would not give good agreement. Furthermore, in the two-dimensional plane strain case, our results (Figures 52-54) are very good indeed. It appears that some account of structure of the eddies is necessary for accurate prediction of these flows; the axisymmetric strain may produce highly elongated vortices aligned with the flow which could be very stable, and hence persist for a long time.

Case 0374 is plane-strain flow. As shown in Figures 55-60, our results were generally reasonable.

Case 0375 is axisymmetric-strain flow. Our results (Figures 61-70) were comparable to those of Case 0374.

Case 0376 is shear flow. Our results were good for the low strain case (Figures 71-74) but showed somewhat larger discrepancies in the high strain case (Figures 75-78).

These homogeneous test cases demonstrate that although the simple Rotta term used in our model for return-to-isotropy is adequate for many flows, it can lead to significant error in some circumstances such as the axisymmetric flows of Figures 44-51. In order to improve the generality of this model for such flows, it will be necessary to use a more sophisticated model of the pressure-strain terms. In fact, we suspect that it will be necessary to incorporate some information about the anisotropic nature of the eddy length scale.

2.5 Flows Behind A Backward-Facing Step

Case 0421 is the flow behind a backward-facing step with the upper wall horizontal. We obtained an unsteady two-dimensional solution, i.e., some of the turbulence energy is contained in the two-dimensional eddies. In fact, if the length-scale equation was not modified, most of the energy ended in the resolved eddies. This is unrealistic, since we know there is significant three-dimensional motion, so we applied a lower limit to the length scale, forcing the modeled stresses to contain significant energy. Profiles of turbulence quantities then include both resolved and modeled components, averaged over a time period which covers several flow times through the box. The results were good, as shown in Figures 79 and 80. The mean streamlines are shown in Figure 81 and instantaneous streamlines at several times in Figure 82. The division of turbulence between the 2-D resolved eddies and the 3-D modeled turbulence is shown in Figures 83 and 84.

Case 0422 (also known as Case P2) is the flow behind a backward-facing step with the upper wall at an angle. It was predictive, that is the experimental results were not made available until after the computations were done. Due to time and money restraints, we were able to do the calculation for only one roof angle, 6^{0}. Actually we used the same domain as for Case 0421, but estimated a velocity at the top assuming uniform flow through the channel with increasing cross-section due to the sloping roof and also the separation bubble which was assumed to extend over 10 step heights. This calculated velocity was used to give a stream function condition on the horizontal upper boundary of the integration domain. The displacement thickness on the upper boundary was accounted for by a 0.5^{0} reduction in the slope of the roof.

The comments above about Case 0421 apply to this case too, and the results again were good, as shown in Figures 85 and 86. The predicted reattachment point was X/H = 7.2 compared with the experimental value of X/H = 8.3.

3. CONCLUSIONS

We are encouraged by these results. We believe they demonstrate that a wide range of problems can be handled by Reynolds stress closure models even with a scale equation that is very primitive. It is our belief that the direction to be taken is the development of tensor (and vector) scale equations and the proper coupling of this information into the Reynolds stress equations. This view is strengthened by the results of the calculations of return to isotropy mentioned above.

There are really compelling reasons at this time for having predictive capabilities for stratified flows. When one considers turbulence in such flows, it is clear that significant efforts in Reynolds stress closure modeling should be expended in the months ahead and, in all probability, for some years to come.

In the conference proceedings, Professor Kline argues persuasively for a zonal modeling approach to complex turbulent flows. This approach certainly has some merit, but we believe it can also easily by oversold. A zonal approach works best when it is possible to show from a more universal, fundamental approach under what conditions the appropriate zonal approximations are valid. Without the guidance from the more universal model, the zonal model can only be used if, at least, a rough estimate of the solution is available from experiment or other means. Too much emphasis on zonal models will prove to be costly because of the increased experimental burden.

It may be argued that with the increased computing power that will be available before long, predictive calculations will be carried out directly from the Navier-Stokes equations and there will be no need for Reynolds stress closure with or without tensor scale equations. However, as the computing power grows, some of it will be devoted to extending the complexity or the number of flows that can be handled instead of to increasing the accuracy or respectability of the methods. It is our belief that Reynolds stress closure will be very useful in the foreseeable future, and attempts to extend its scope should be encouraged.

REFERENCES

1. Donaldson, C. duP., Atmospheric Turbulence and the Dispersal of Atmospheric Pollutants, AMS Workshop on Micrometeorology (ed. D. A. Haugen) Science Press, Boston (1973) pp. 313-390.

2. Lewellen, W. S., Use of Invariant Modeling, Handbook of Turbulence (eds. Walter Frost and Trevor H. Moulden) Plenum Publishing Corporation (1977) Vol. 1, pp. 237-280.

3. Sullivan, R. D. and Varma, A. K., ARB: A Program to Compute the Turbulent Boundary Layer on an Arbitrary Body of Revolution, Aeronautical Research Associates of Princeton, Inc., A.R.A.P. Report No. 317 (1978).

4. Sullivan, R. D., ARB: A Supplementary Manual, Aeronautical Research Associates of Princeton, Inc., A.R.A.P. Tech. Memo. 80-16 (1980).

5. Hirsh, J. E., Vortex Interactions and Decay in Aircraft Wakes: The WAKE Computer Program Programmer Manual, Aeronautical Research Associates of Princeton, Inc., A.R.A.P. Report No. 400 (1979).

6. Donaldson, C. duP. and Sandri, G., On the Inclusion of Information on Eddy Structure in Second-Order-Closure Models of Turbulent Flows, presented and published in the the Proceedings of the AGARD Symposium on Fluid Dynamics of Jets with Applications to V/STOL, Lisbon, Portugal, AGARD-CP-308, November, 1981.

7. Hopkins, E. J. and Inouye, M., An Evaluation of Theories for Predicting Turbulent Skin Friction and Heat Transfer on Flat Plates at Supersonic and Hypersonic Mach Numbers, AIAA Journal 9, 6, pp. 993-1003 (1971).

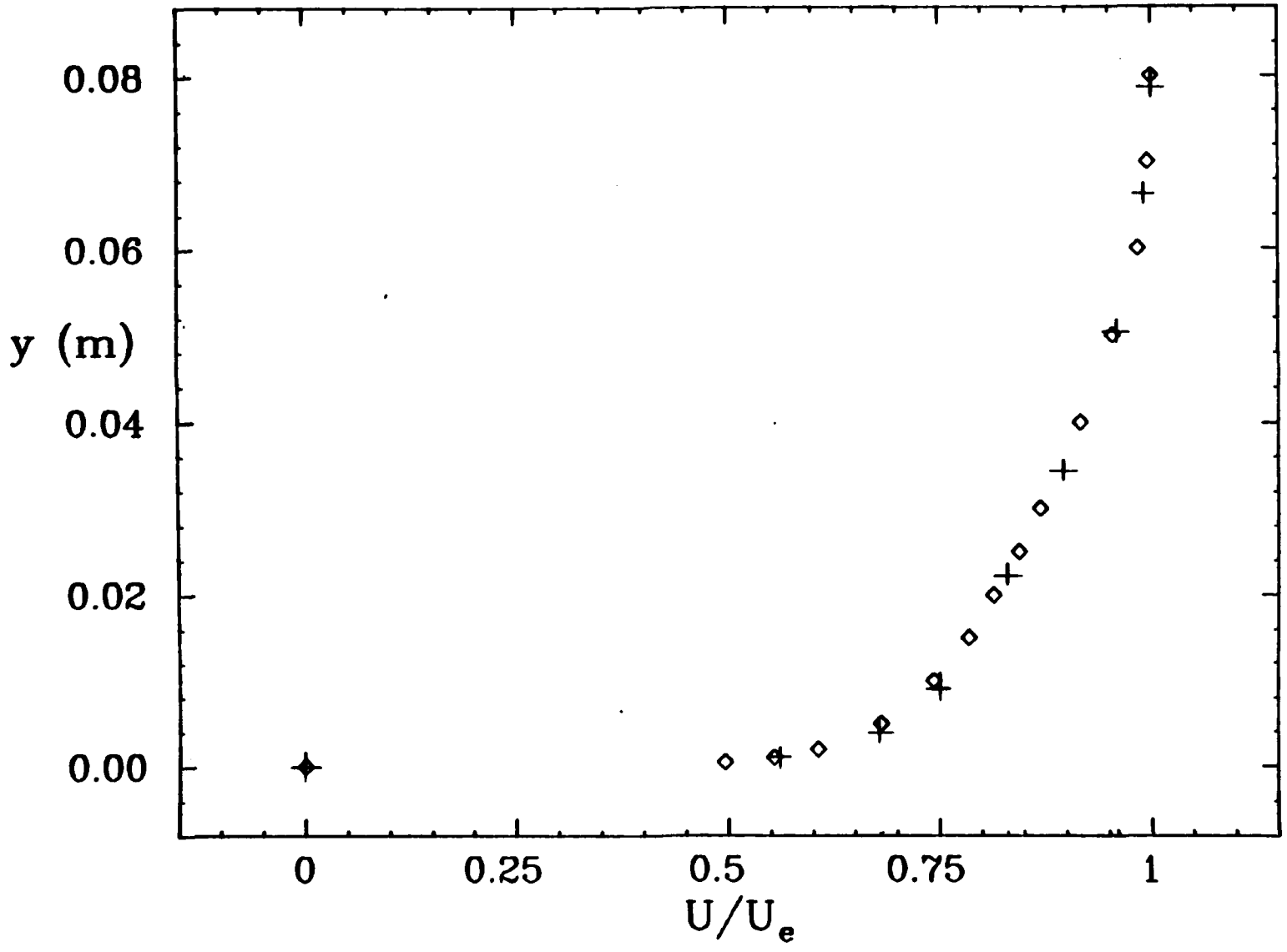

Figure 1. Case 0612 (Standard flat-plate boundary layer) Mean velocity profile.

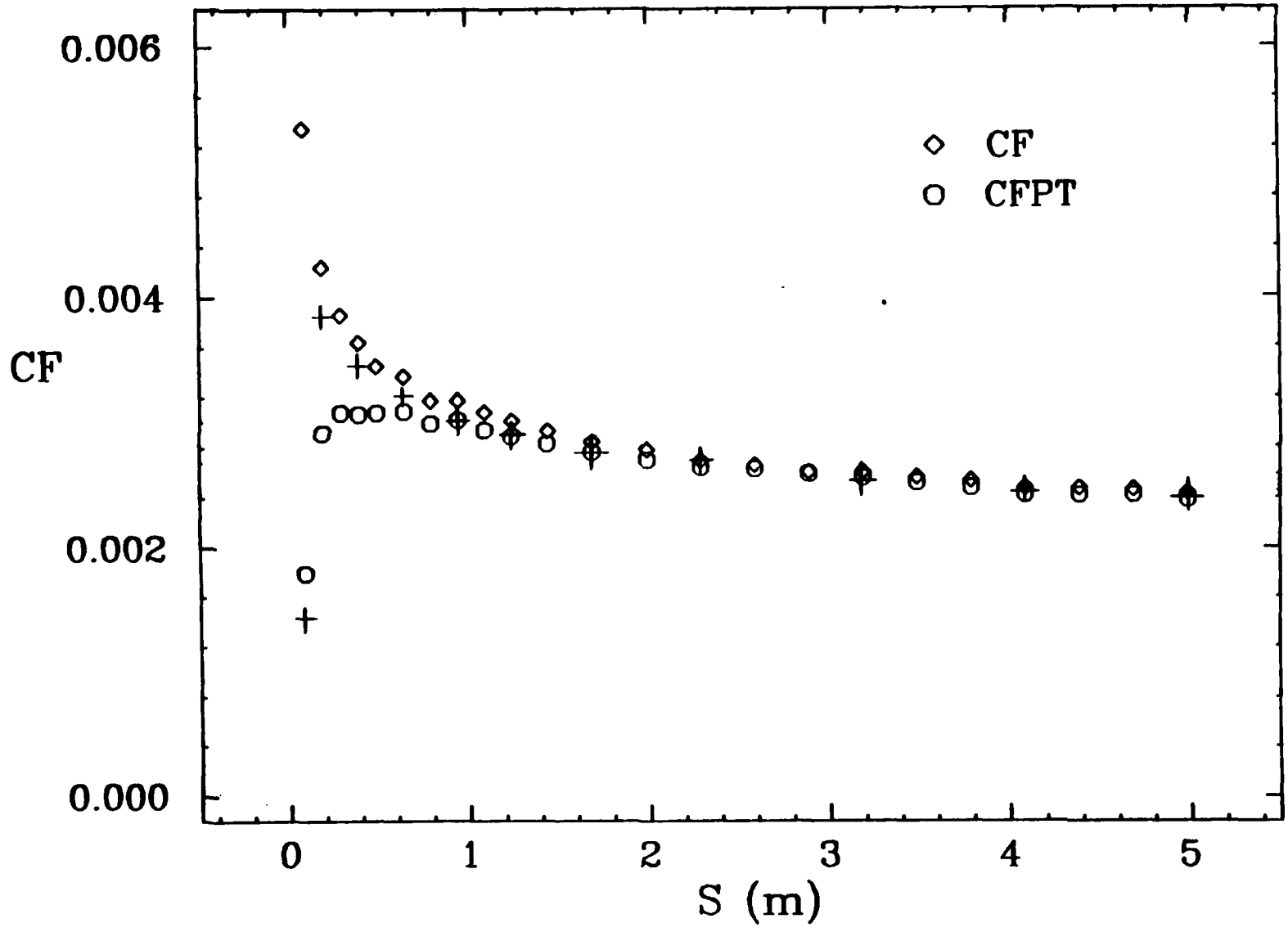

Figure 2. Case 0612 (Standard flat-plate boundary layer) Coefficient of friction.

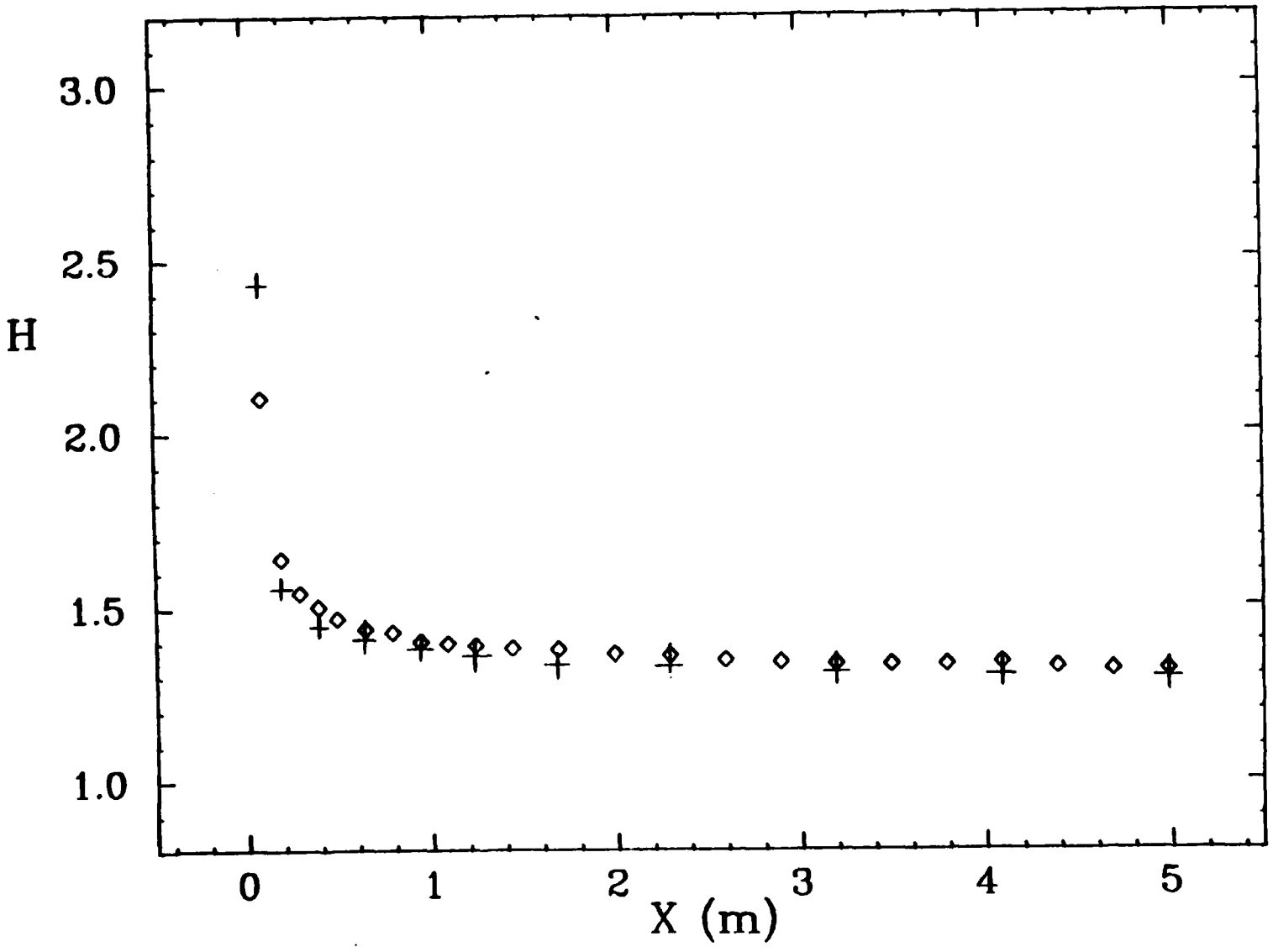

Figure 3. Case 0612 (Standard flat-plate boundary layer) Shape factor.

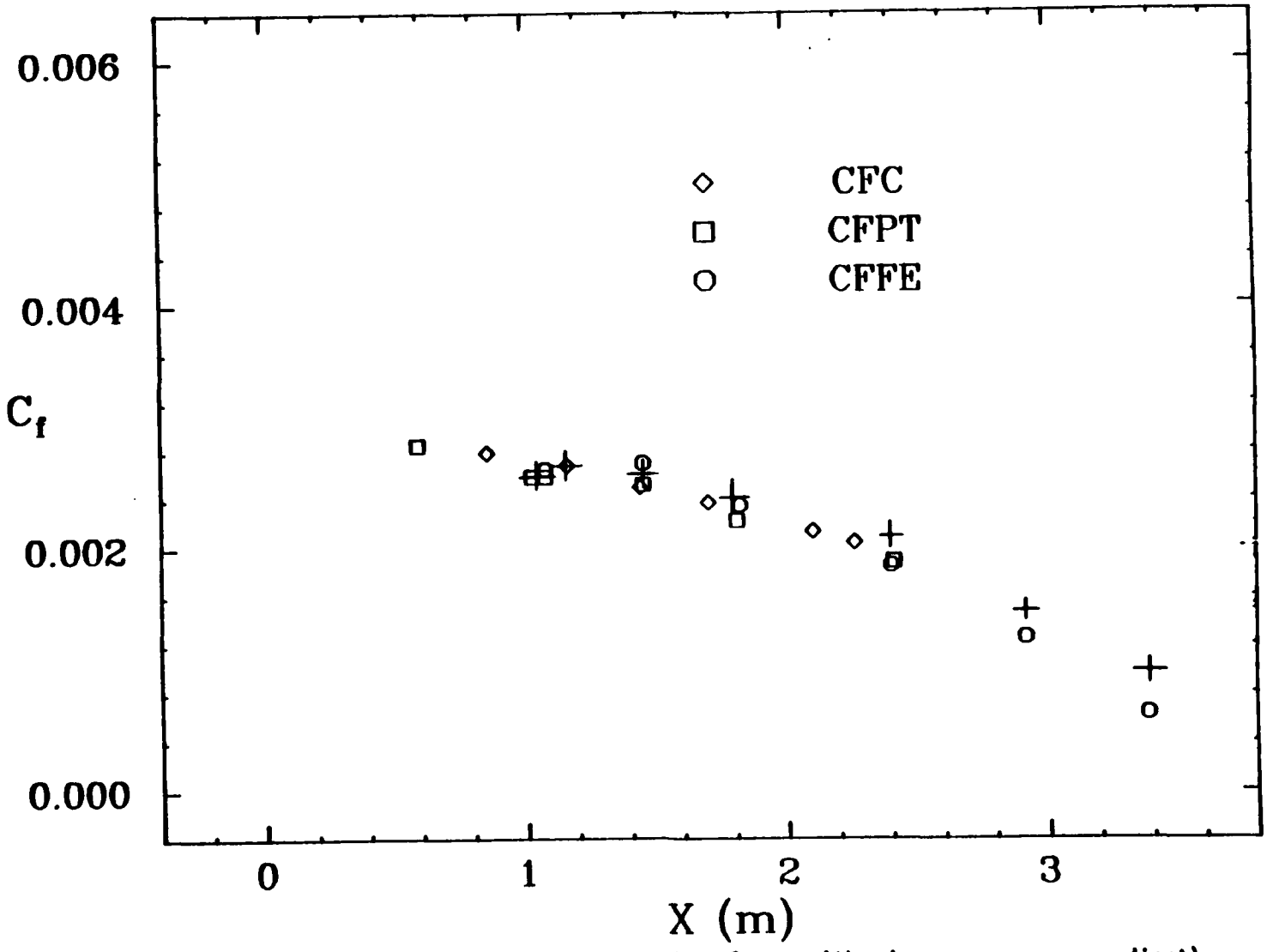

Figure 4. Case 0141 (Flat-plate boundary layer with adverse pressure gradient) Coefficient of friction.

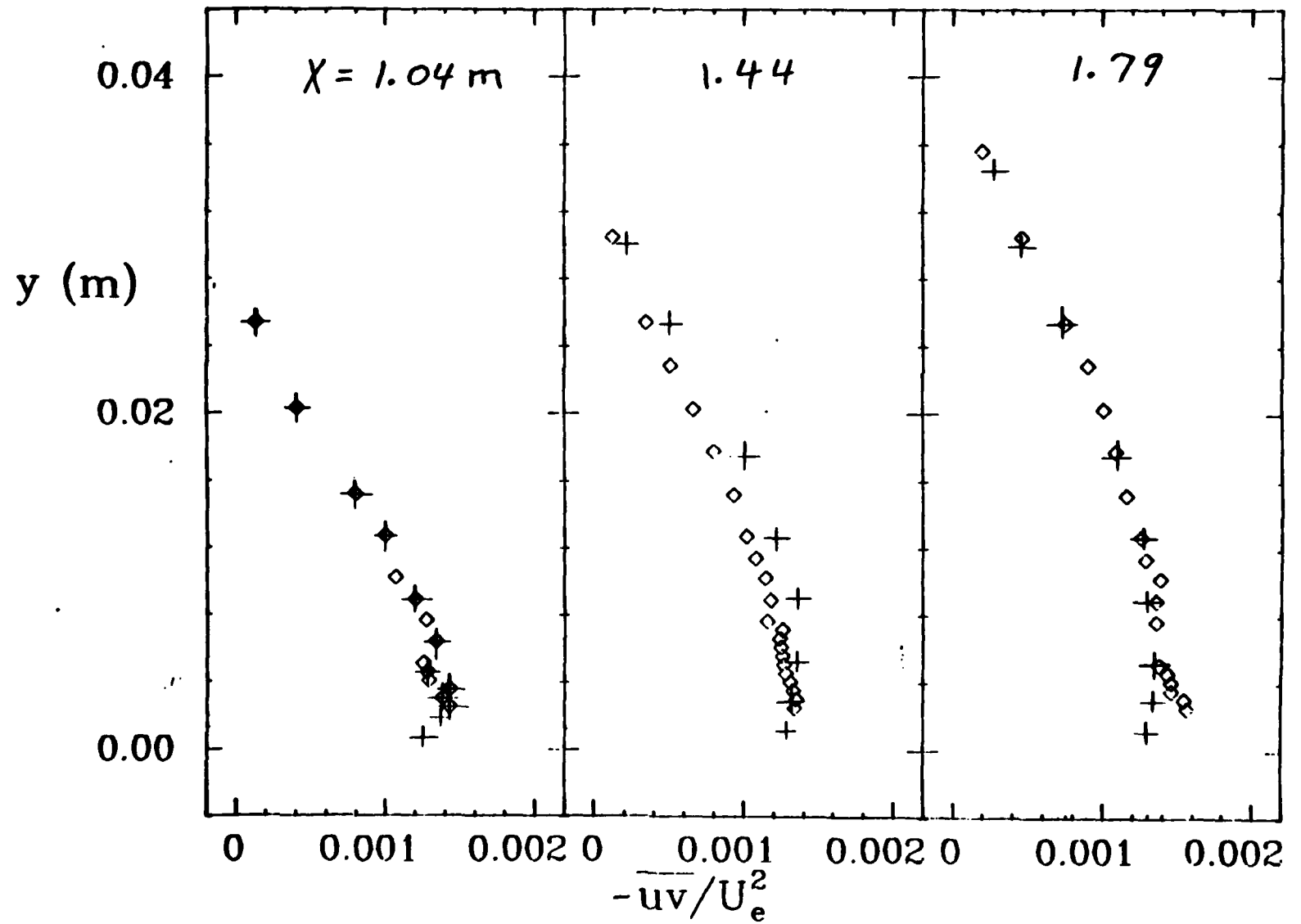

Figure 5. Case 0141 (Flat-plate boundary layer with adverse pressure gradient) Turbulent stress profiles.

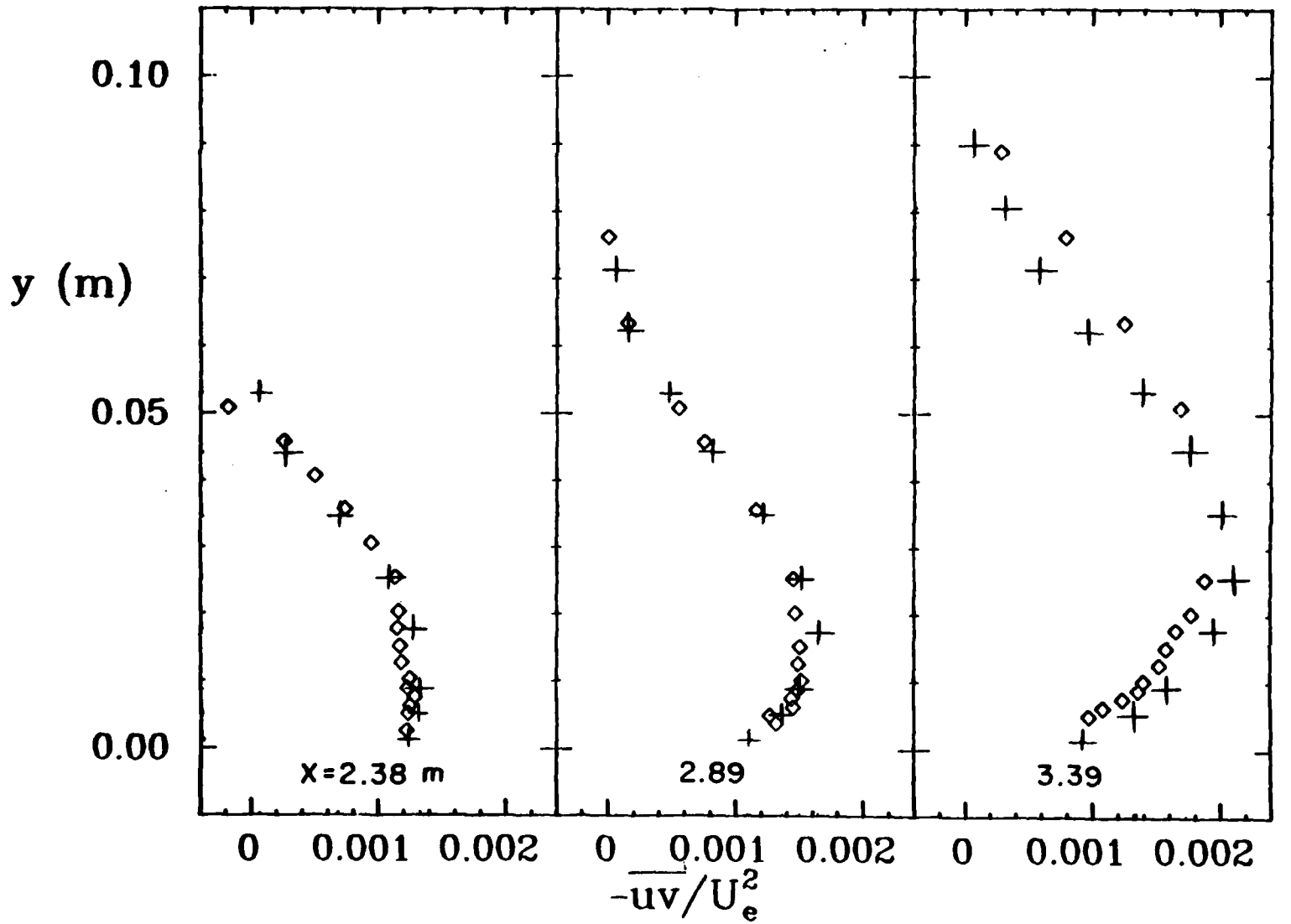

Figure 6. Case 0141 (Flat-plate boundary layer with adverse pressure gradient) Turbulent stress profiles.

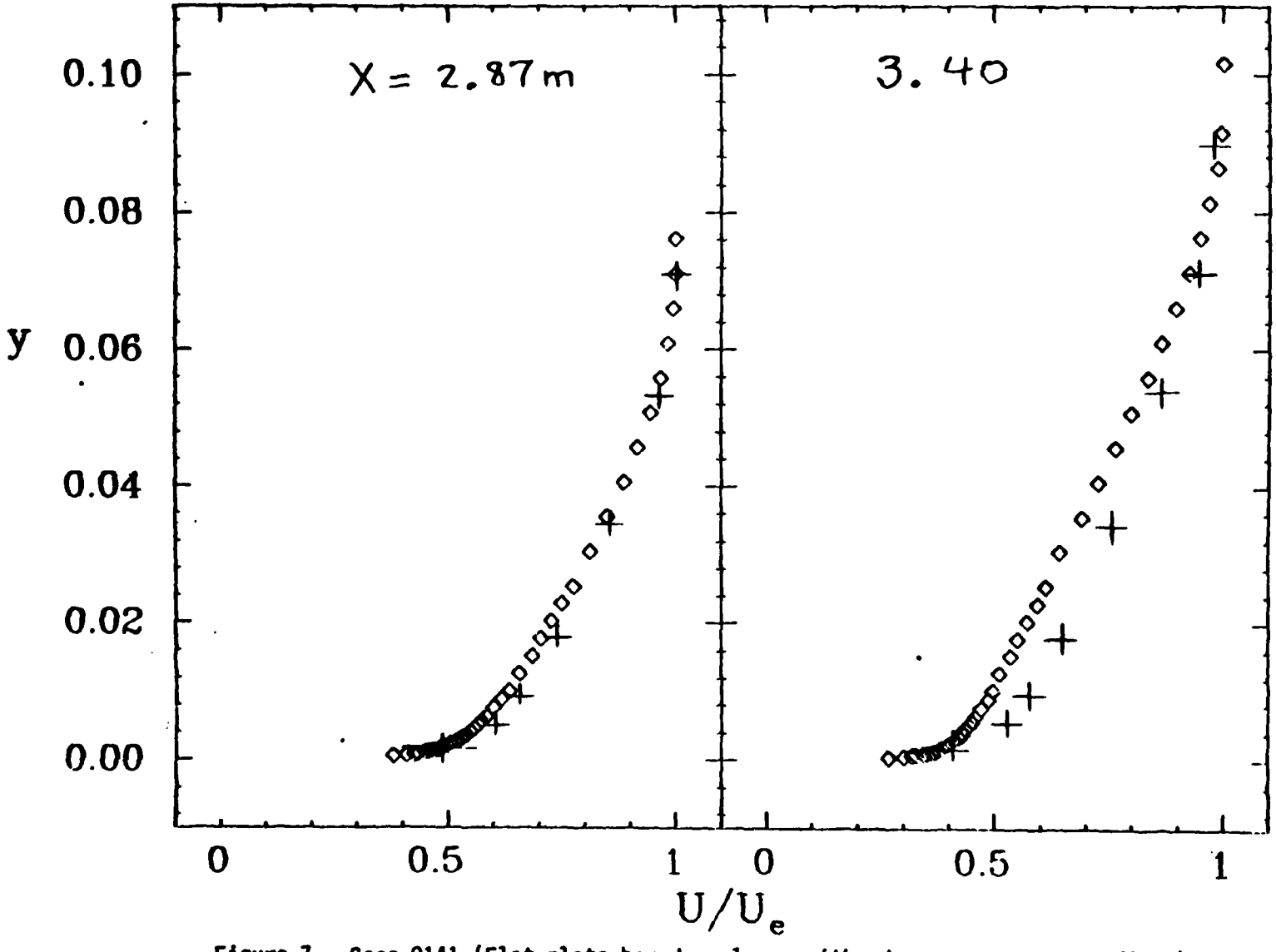

Figure 7. Case 0141 (Flat-plate boundary layer with adverse pressure gradient) Mean velocity profiles.

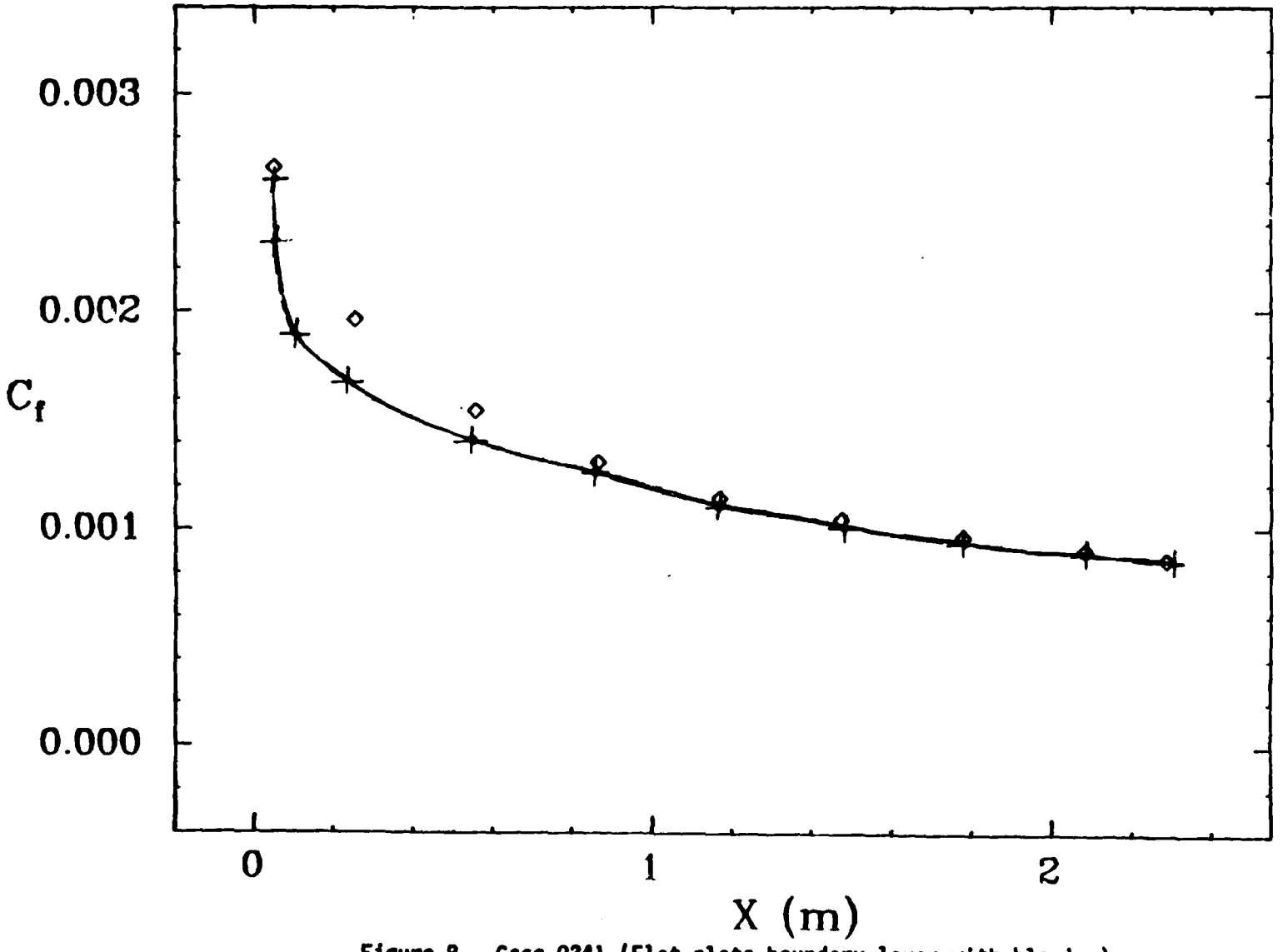

Figure 8. Case 0241 (Flat-plate boundary layer with blowing) Coefficient of friction.

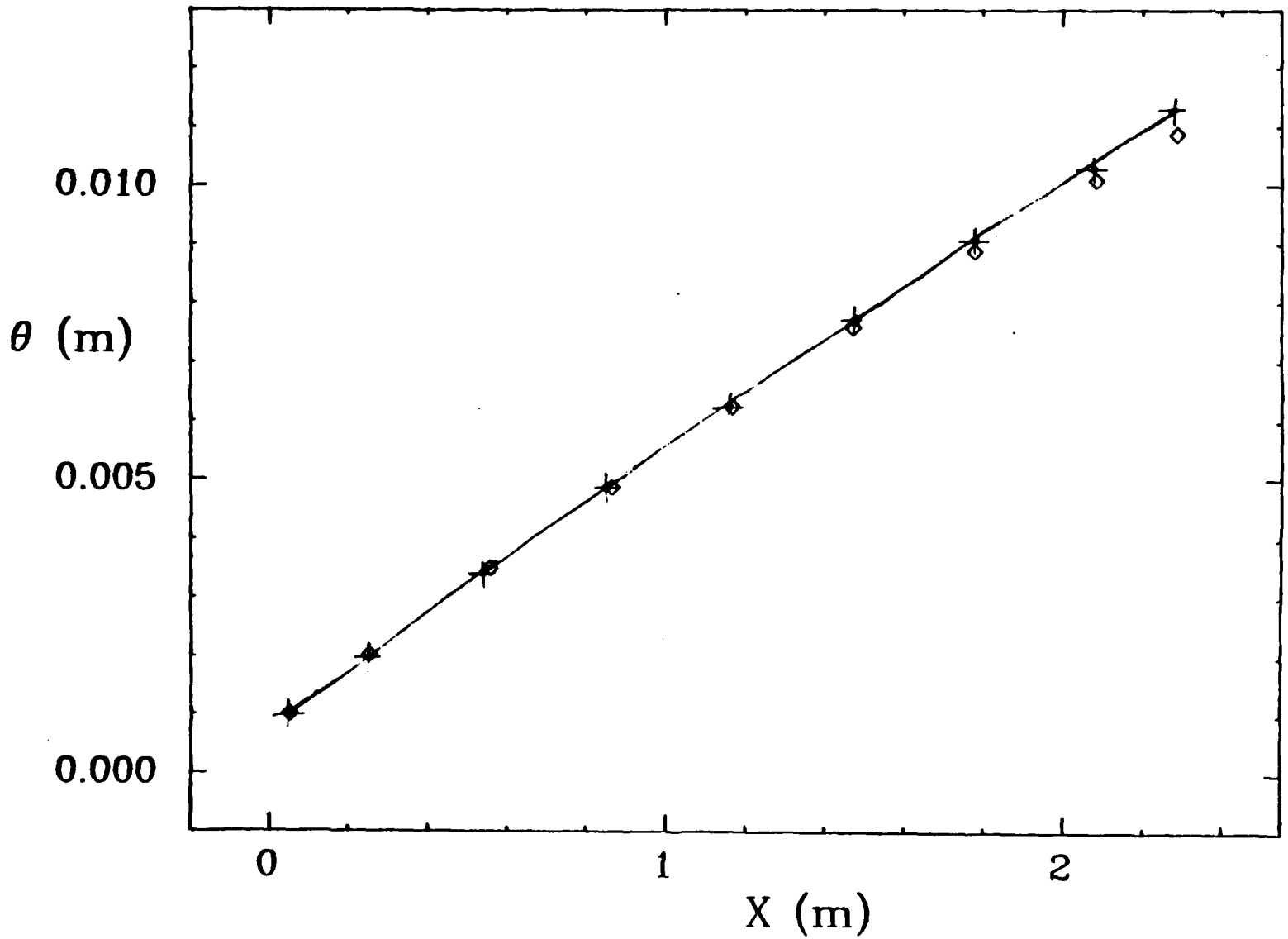

Figure 9. Case 0241 (Flat-plate boundary layer with blowing) Momentum thickness.

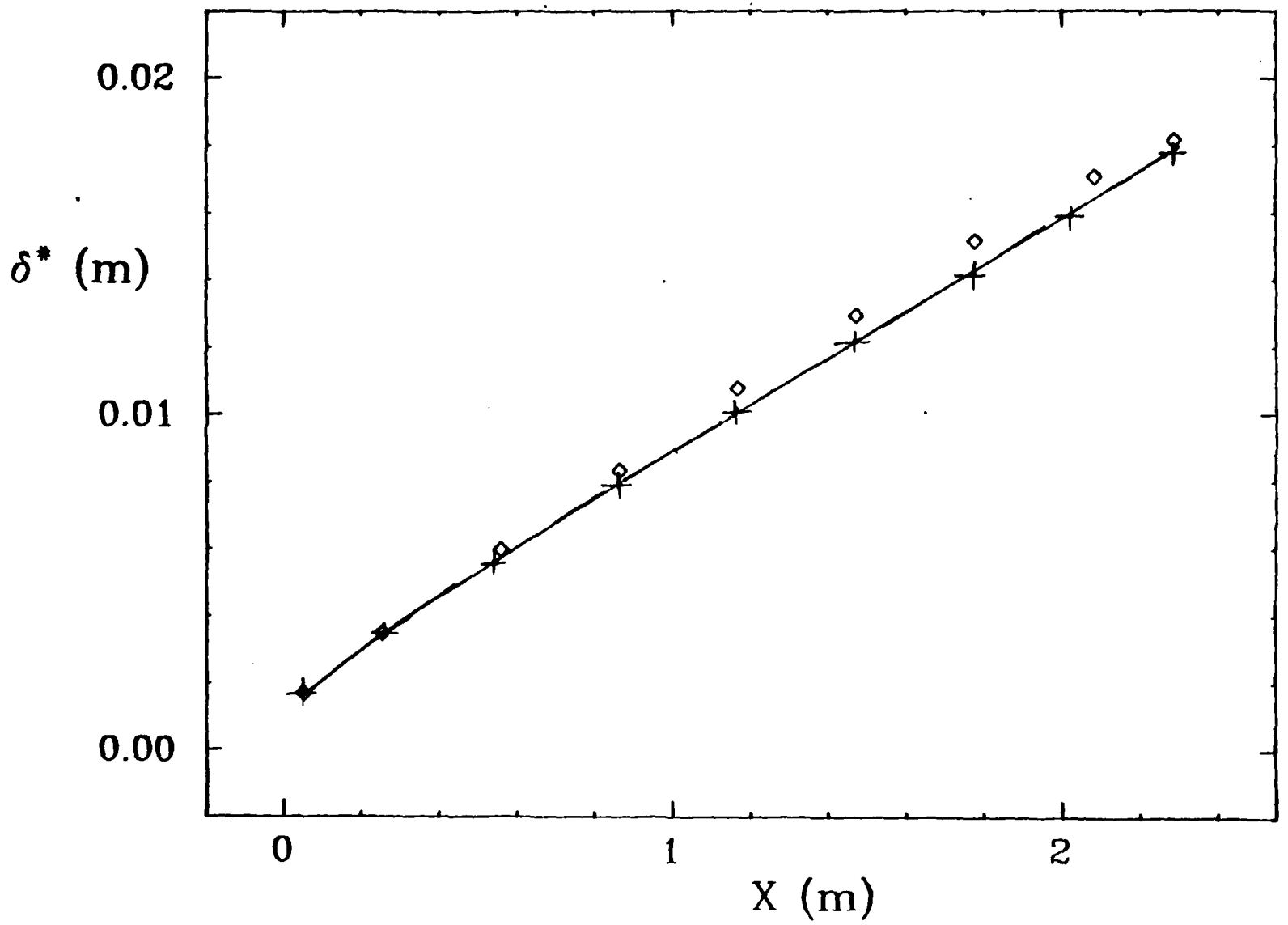

Figure 10. Case 0241 (Flat-plate boundary layer with blowing) Displacement thickness.

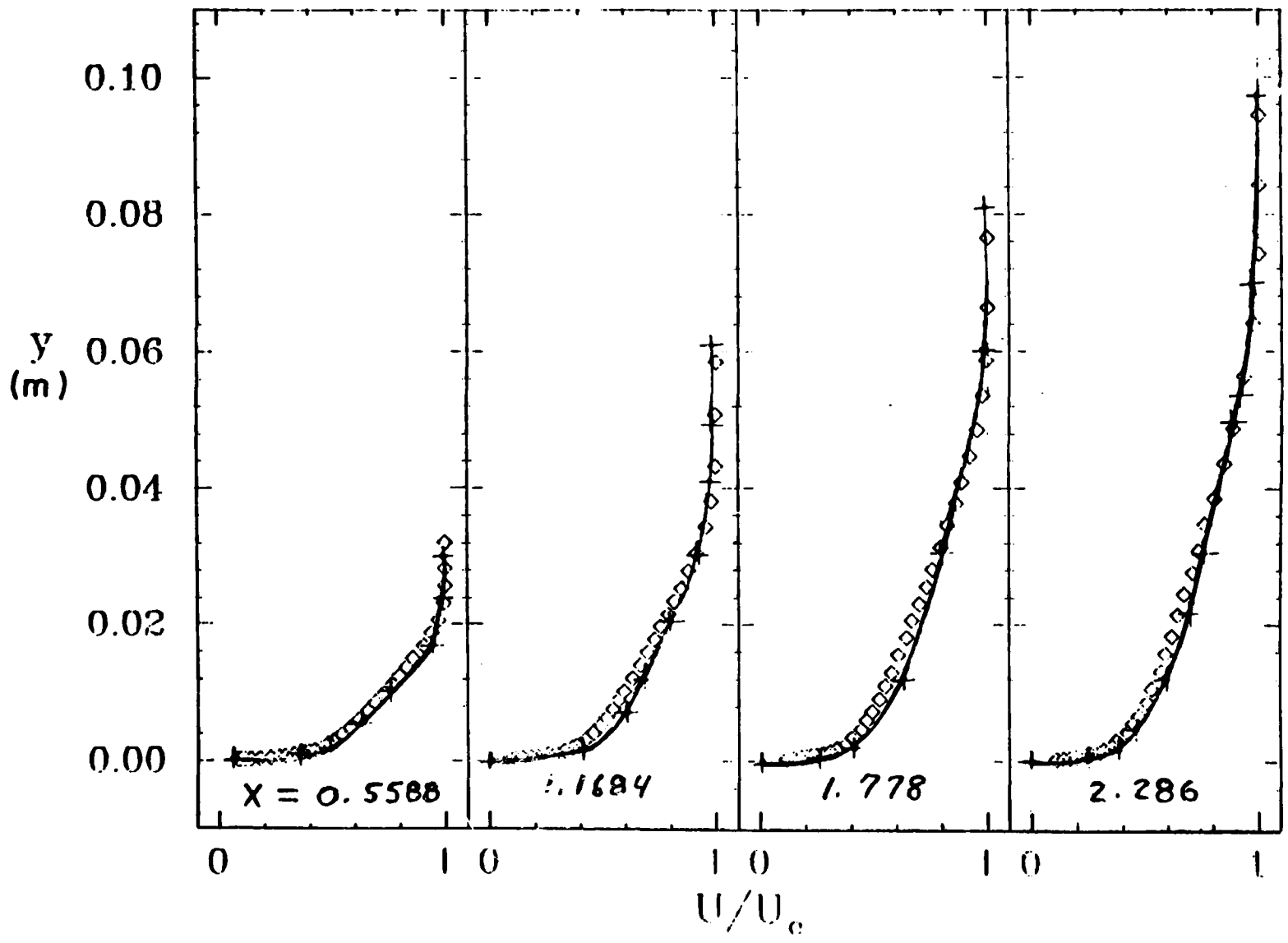

Figure 11. Case 024' (Flat-plate boundary layer with blowing)
Mean velocity profiles.

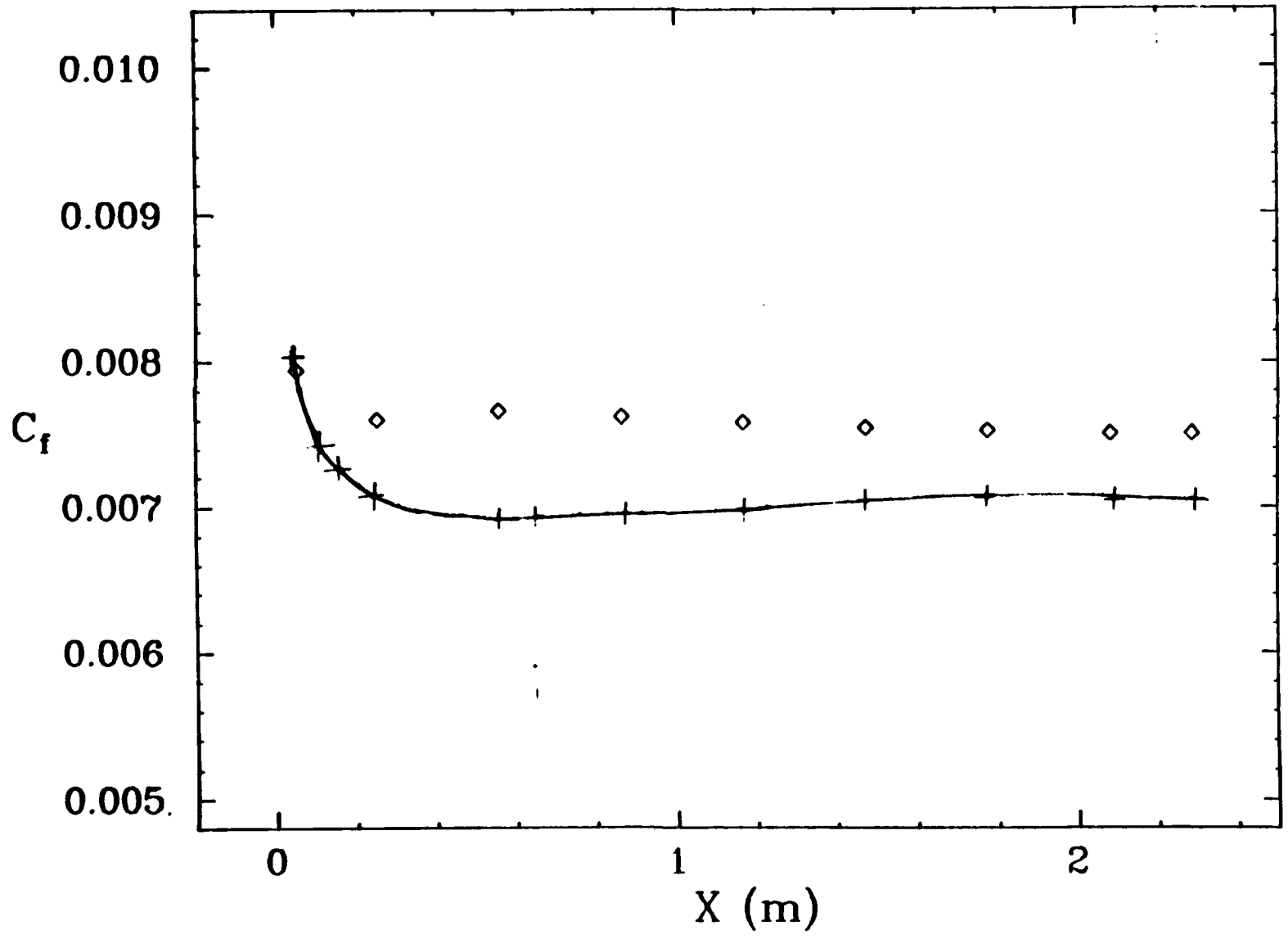

Figure 12. Case 0242 (Flat-plate boundary layer with adverse pressure gradient and suction) Coefficient of friction.

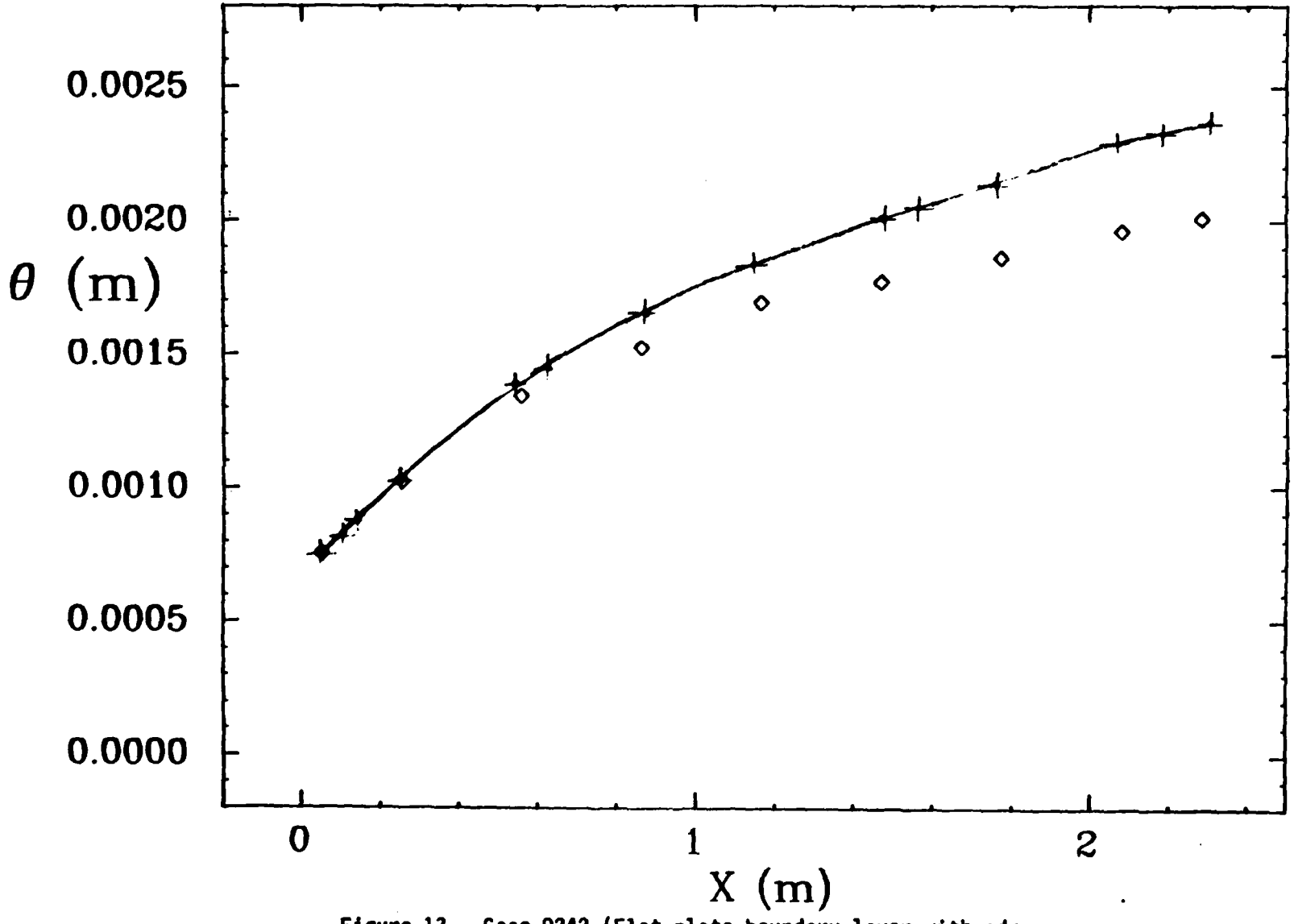

Figure 13. Case 0242 (Flat-plate boundary layer with adverse pressure gradient and suction) Momentum thickness.

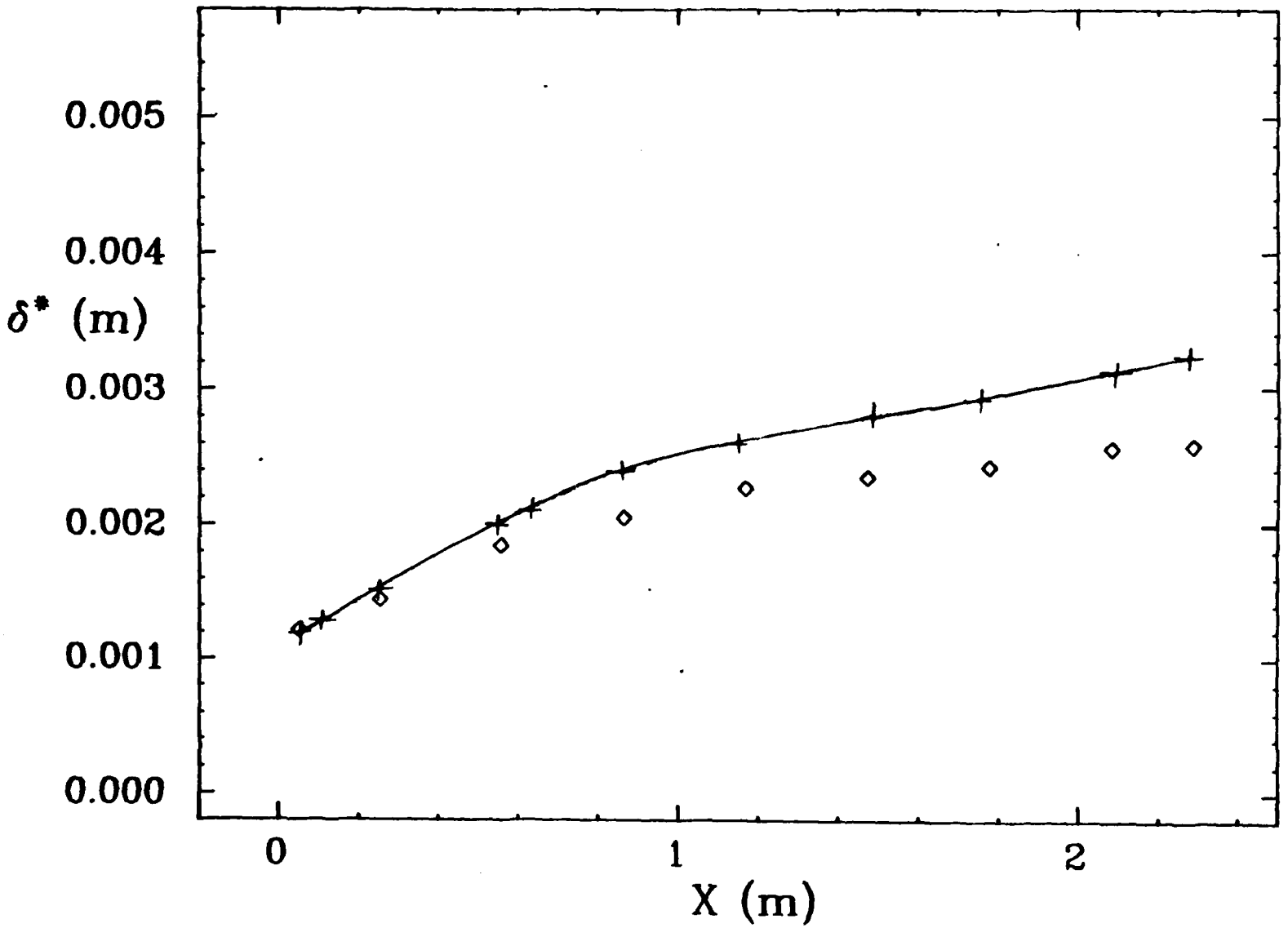

Figure 14. Case 0242 (Flat-plate boundary layer with adverse pressure gradient and suction) Displacement thickness.

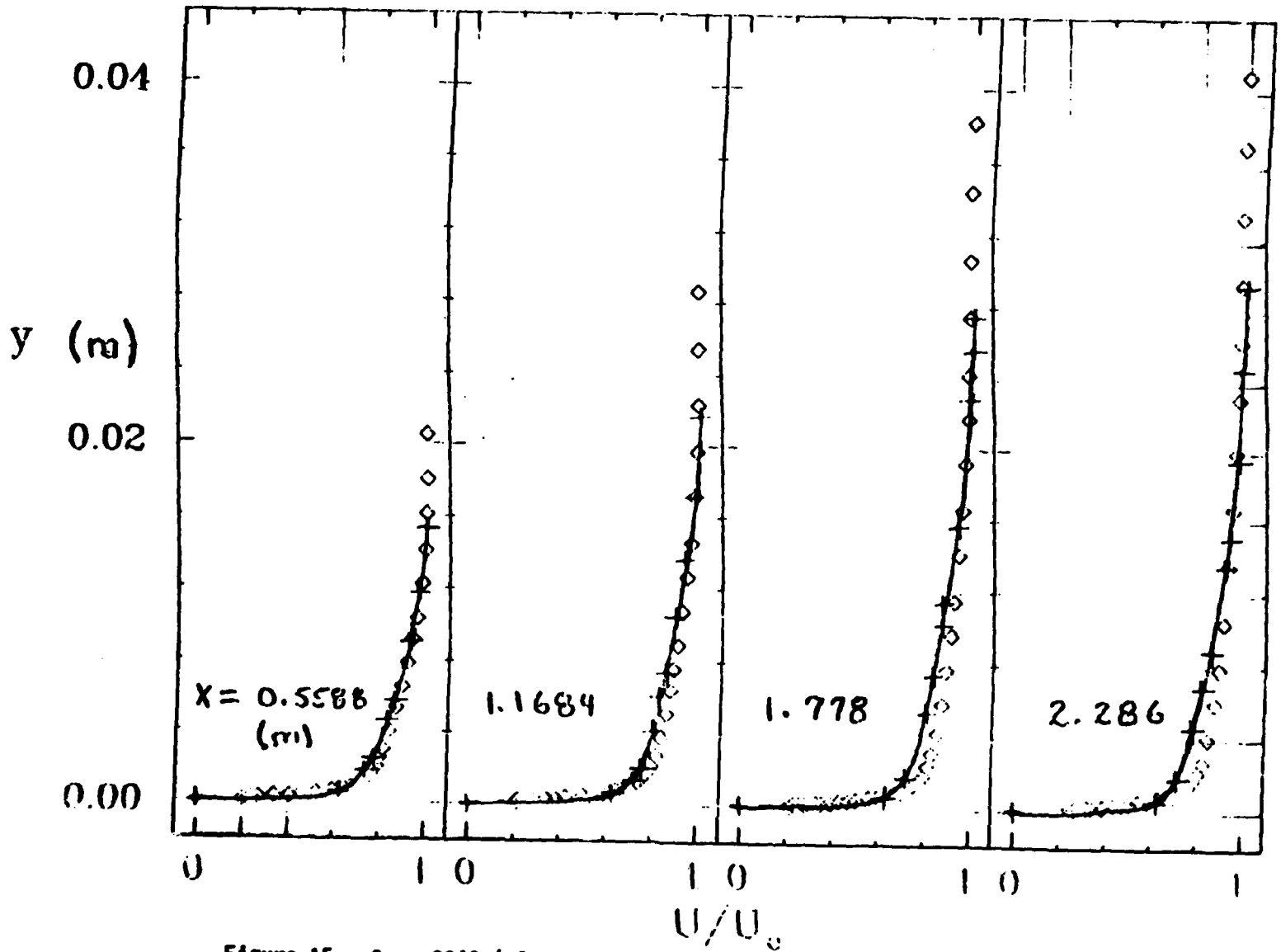

Figure 15. Case 0242 (Flat-plate boundary layer with adverse pressure gradient and suction) Mean velocity profiles.

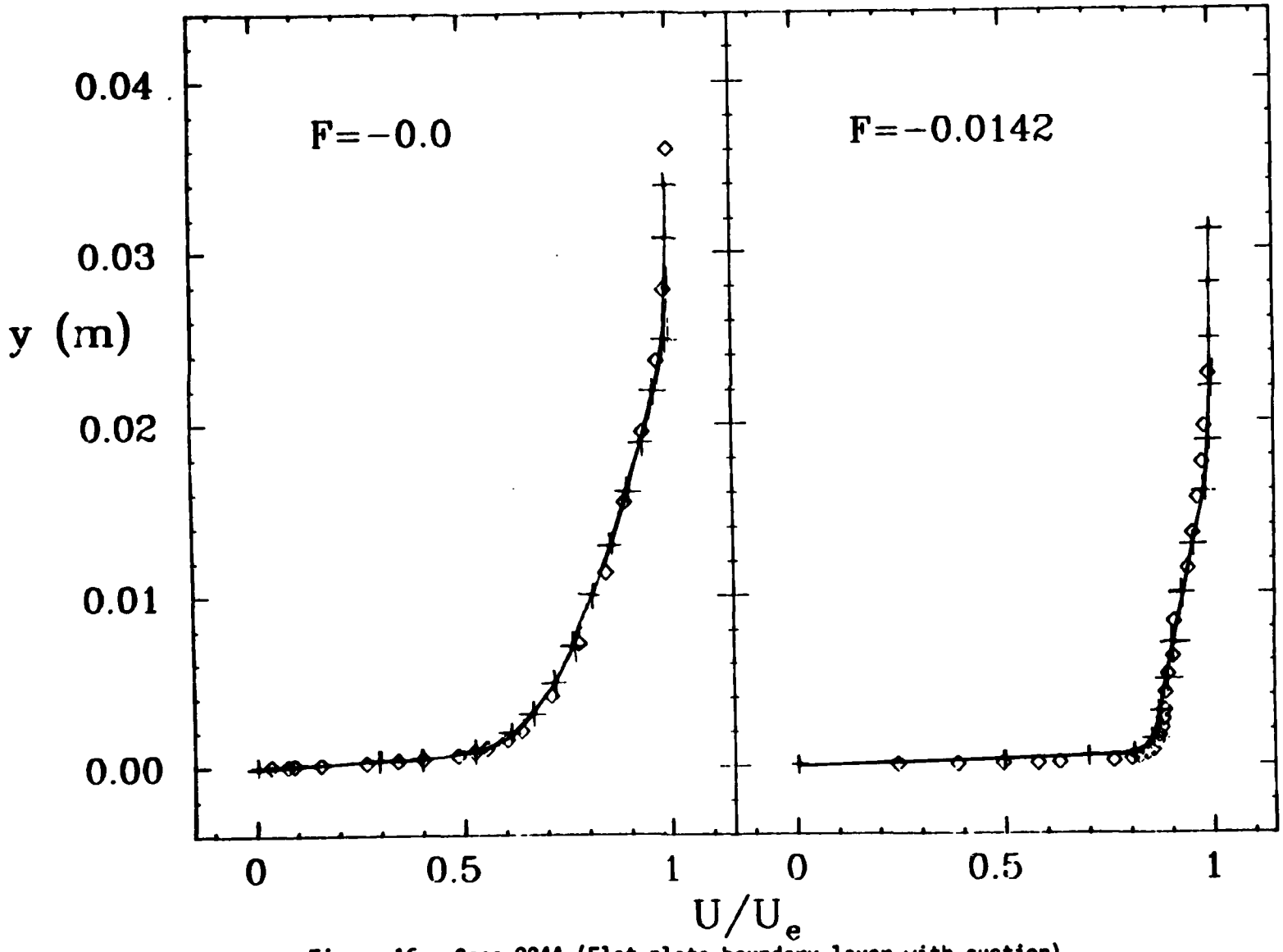

Figure 16. Case 0244 (Flat-plate boundary layer with suction) Mean velocity profiles.

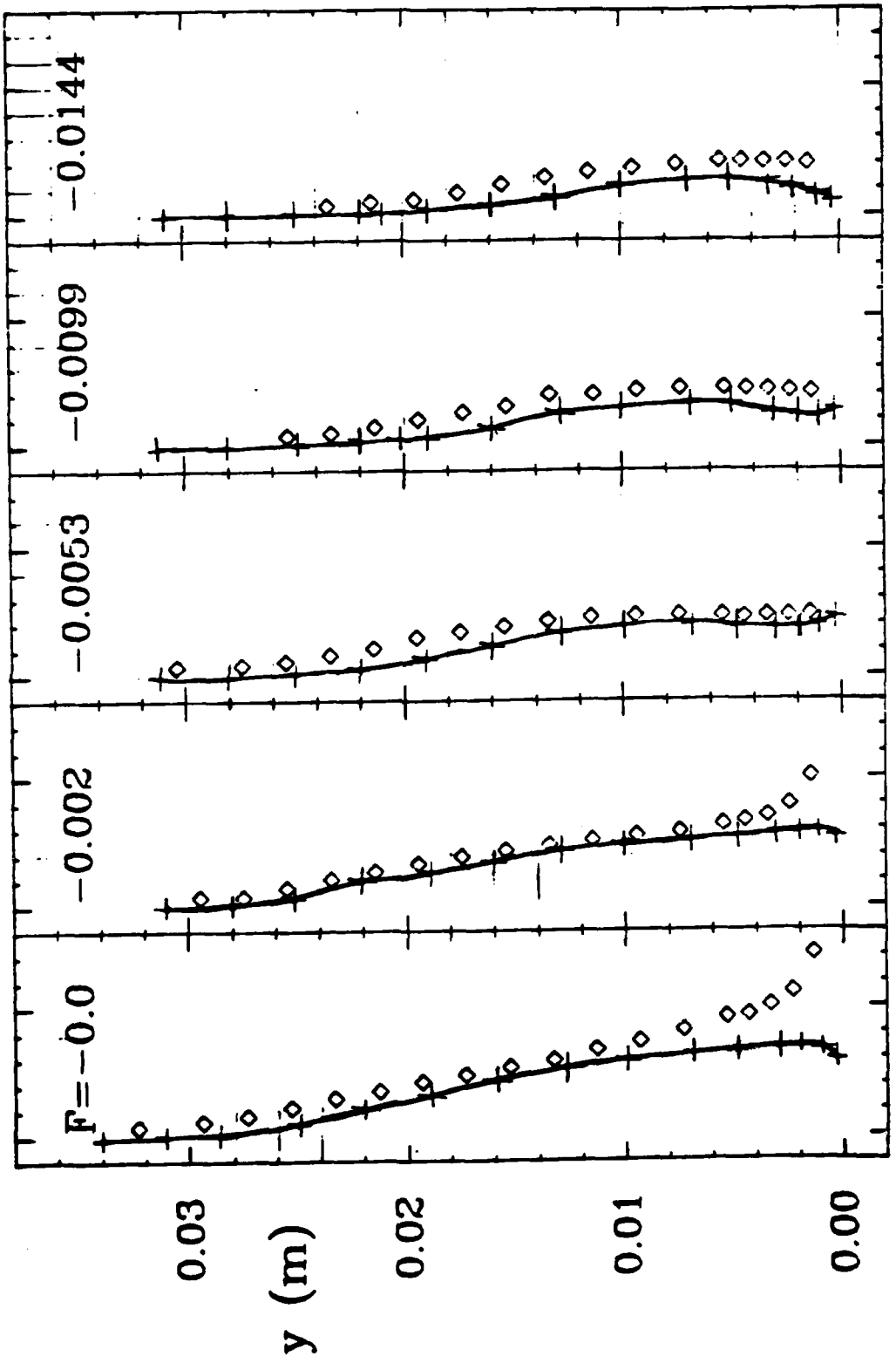

Figure 17. Case 0244 (Flat-plate boundary layer with suction) Turbulence profiles.

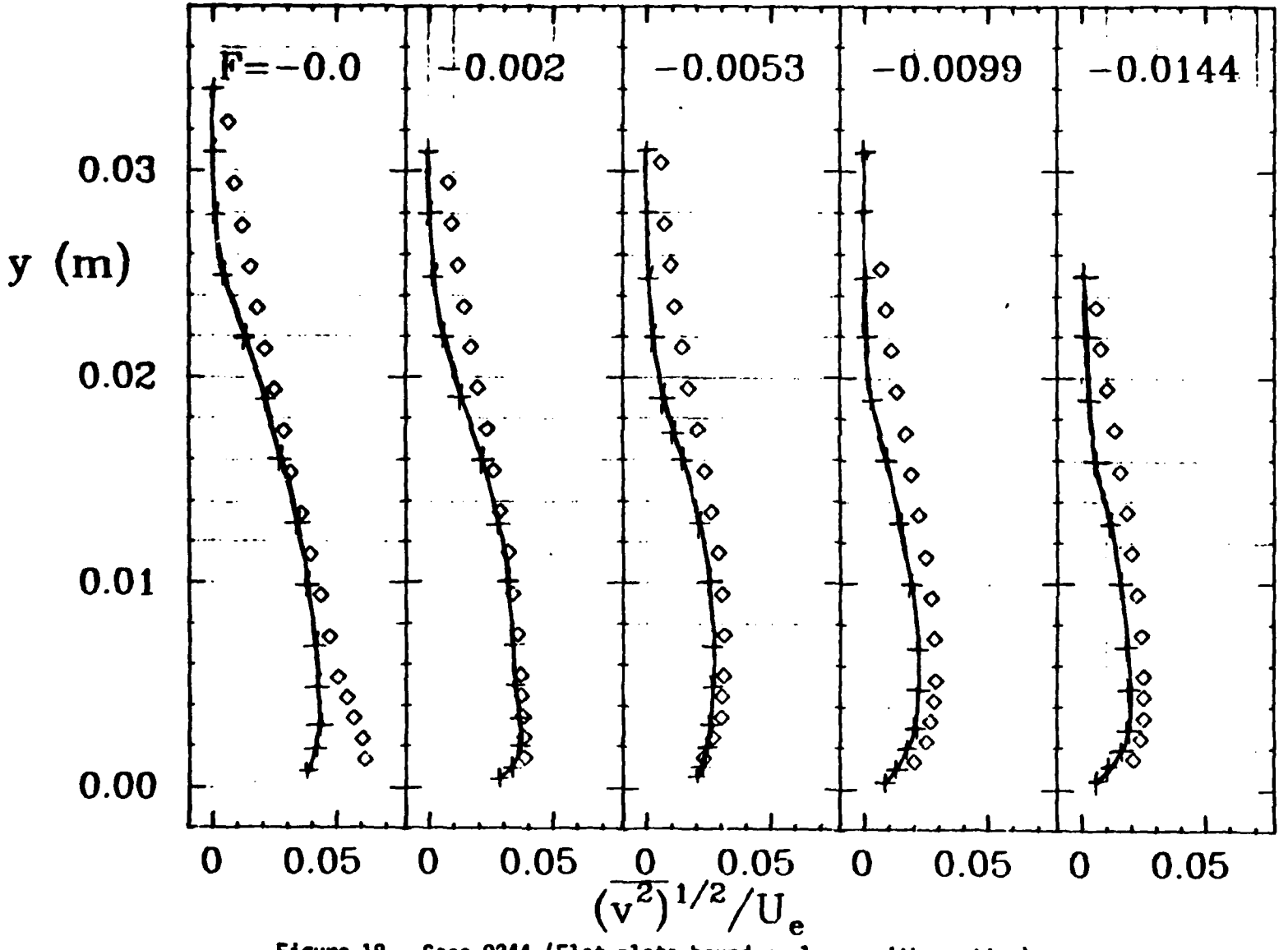

Figure 18. Case 0244 (Flat-plate boundary layer with suction) Turbulence profiles.

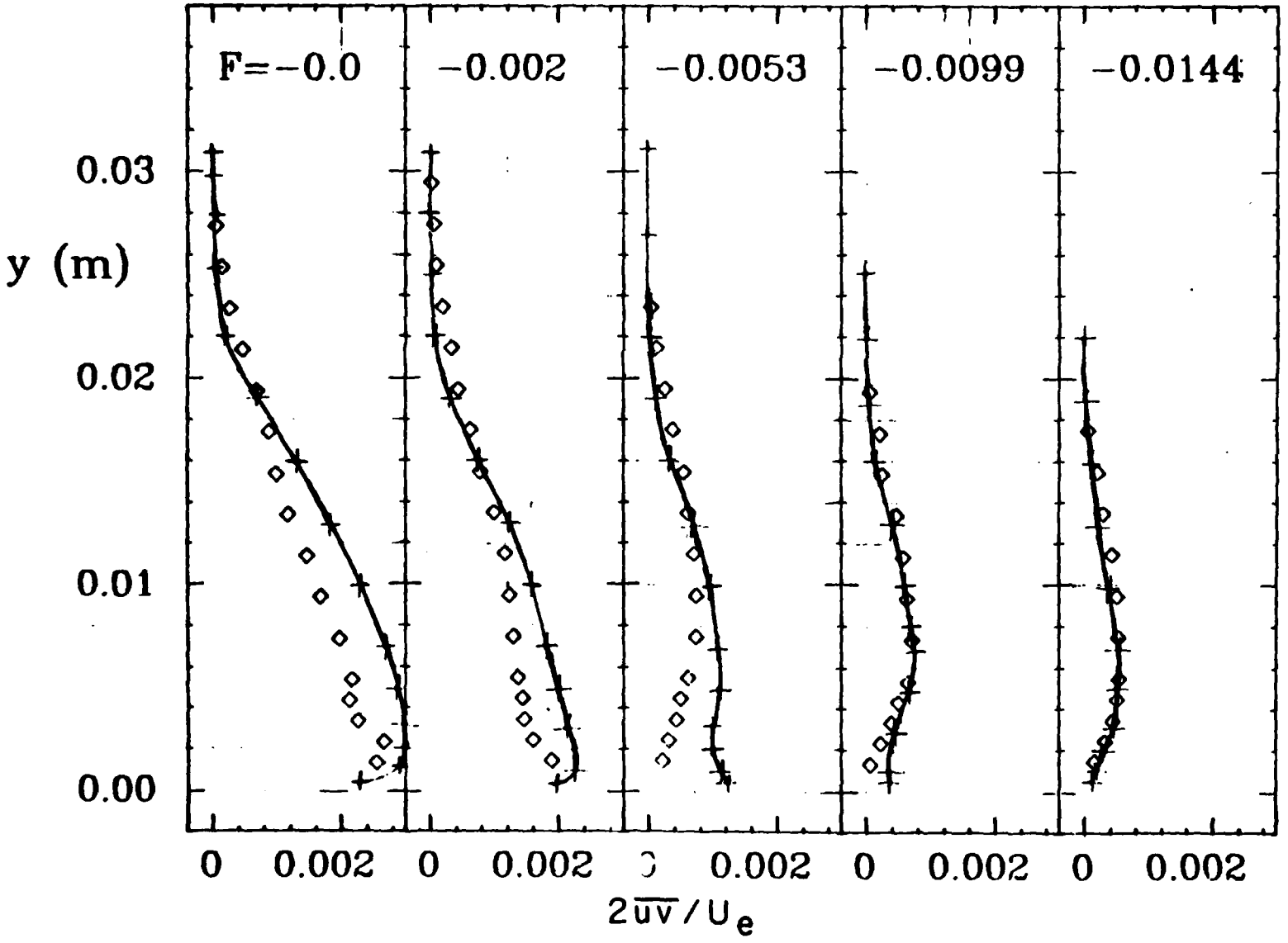

Figure 19. Case 0244 (Flat-plate boundary layer with suction)
Turbulent stress profiles.

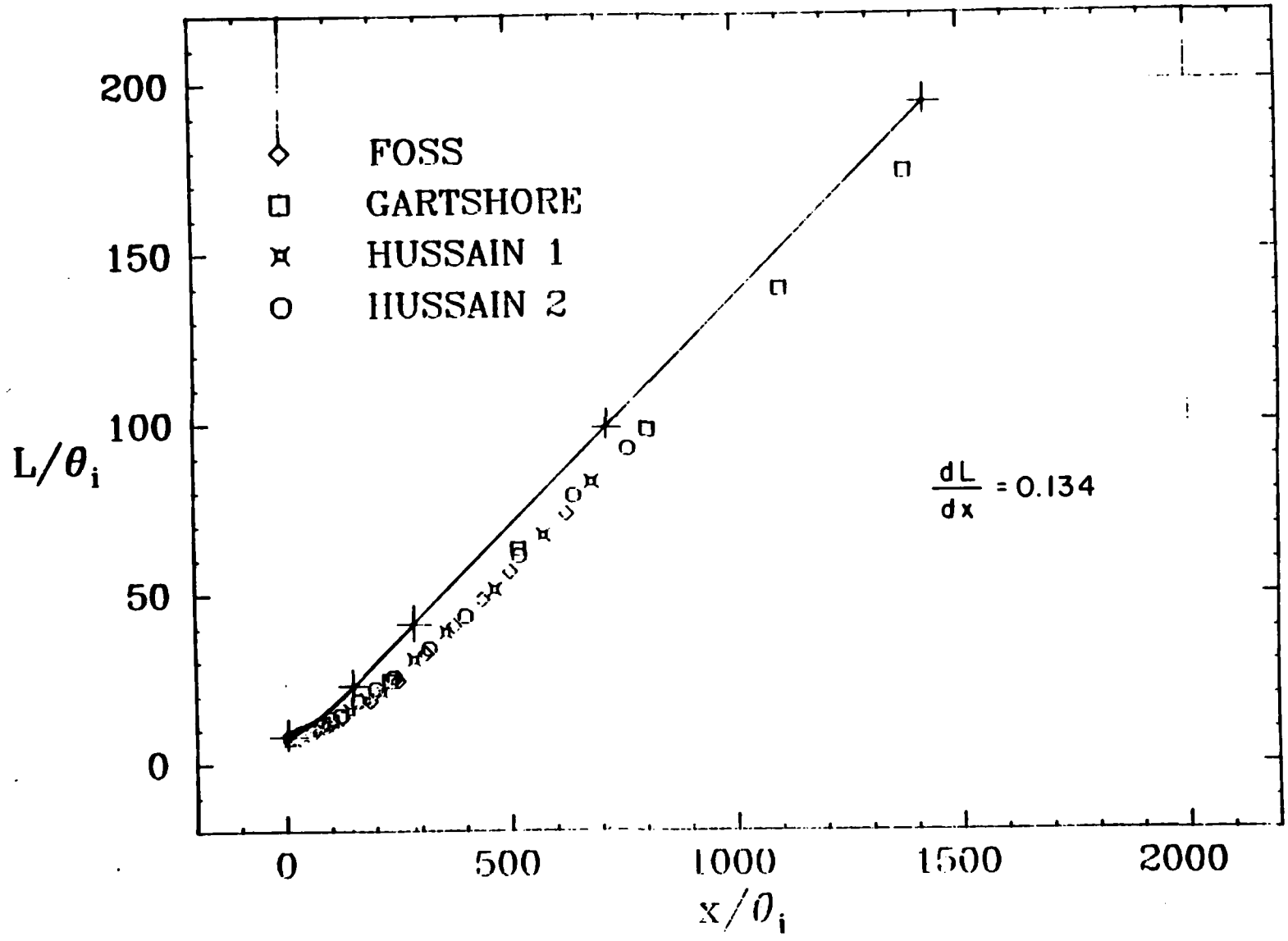

Figure 20. Case 0311 (Mixing layer) Spread of the layer.

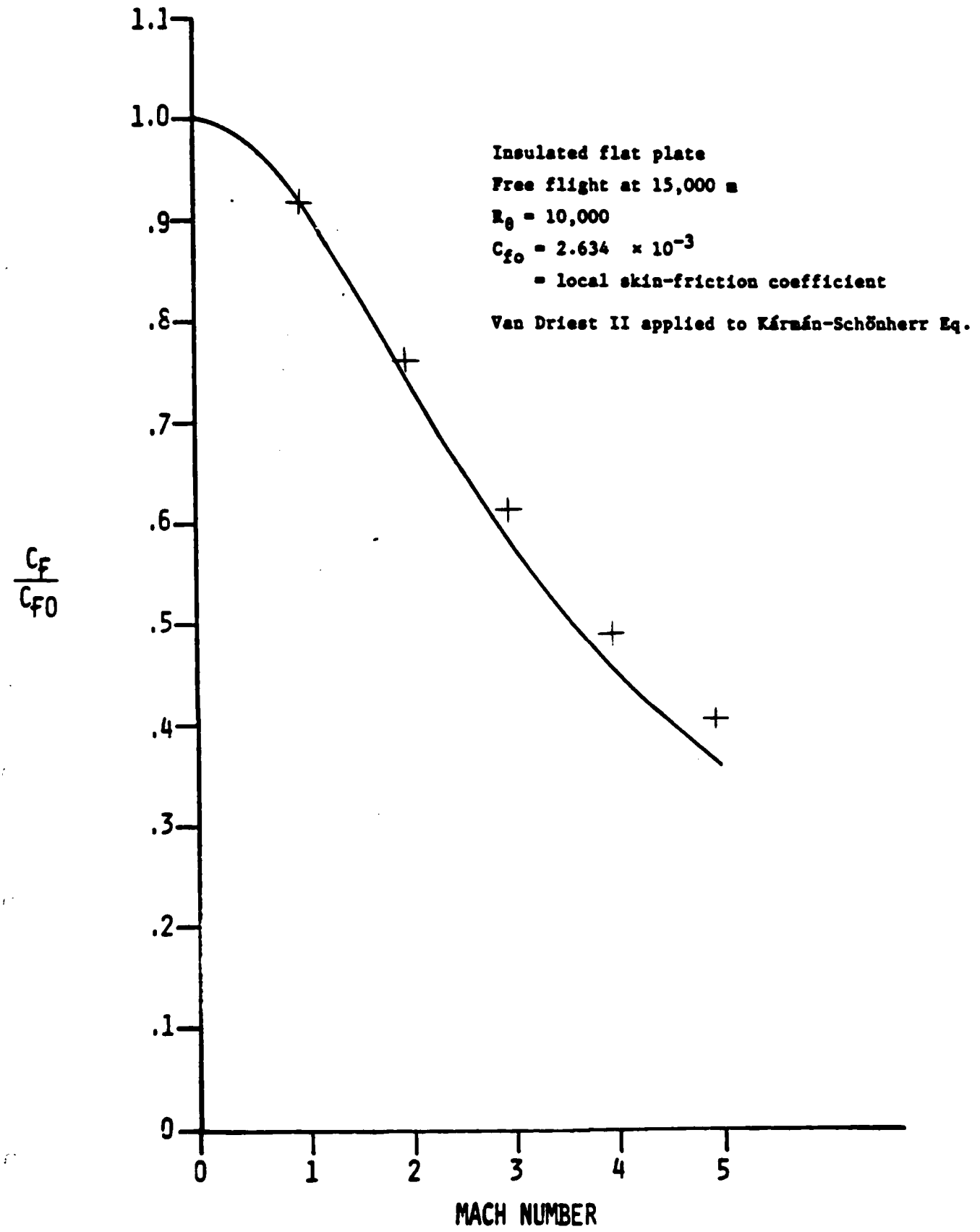

Figure 21. Case 8101 (Supersonic flat-plate boundary layer) Coefficient of friction as a function of Mach number.

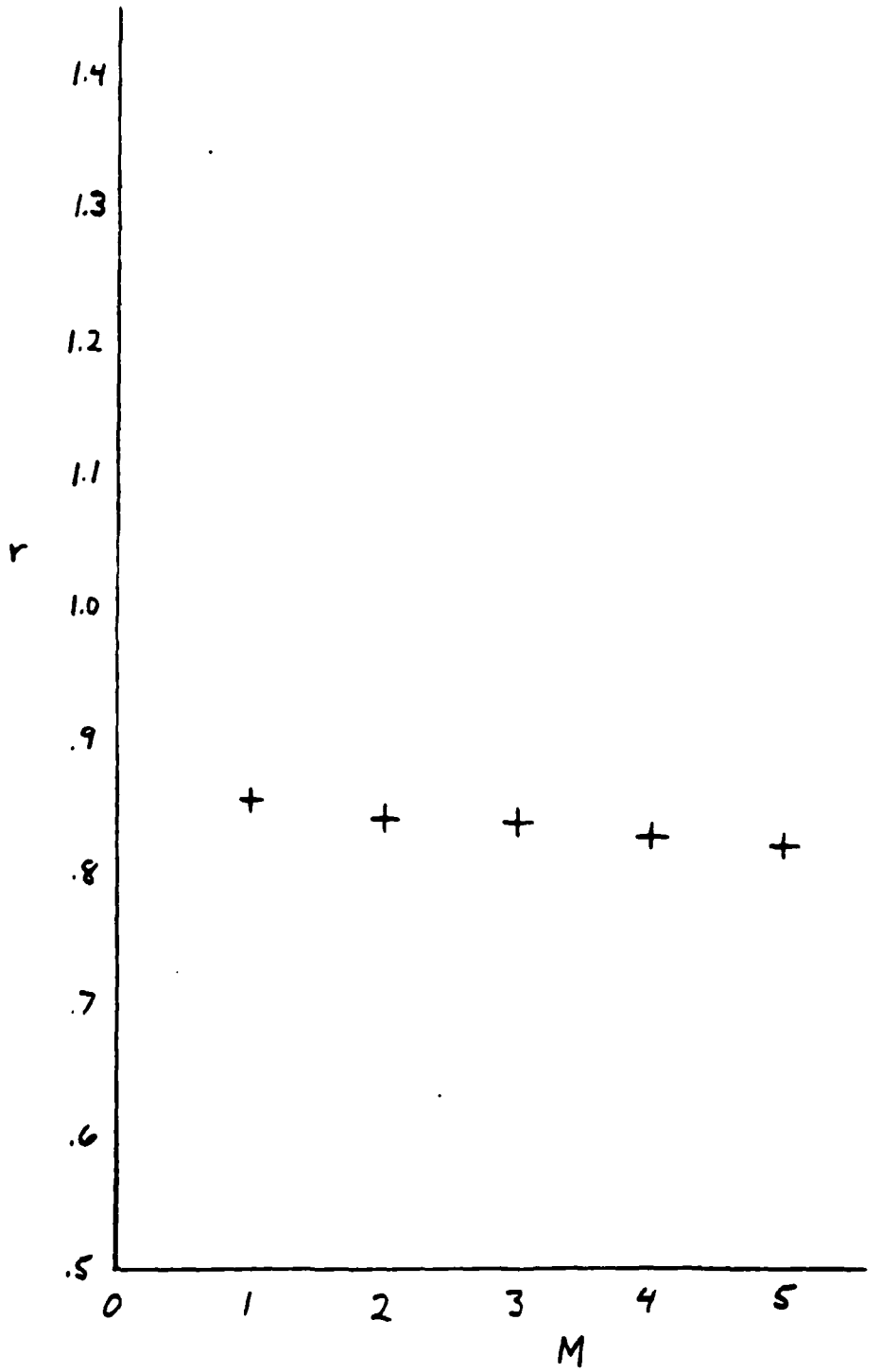

Figure 22. Case 8101 (Supersonic flat-plate boundary layer) Recovery factor as a function of Mach number.

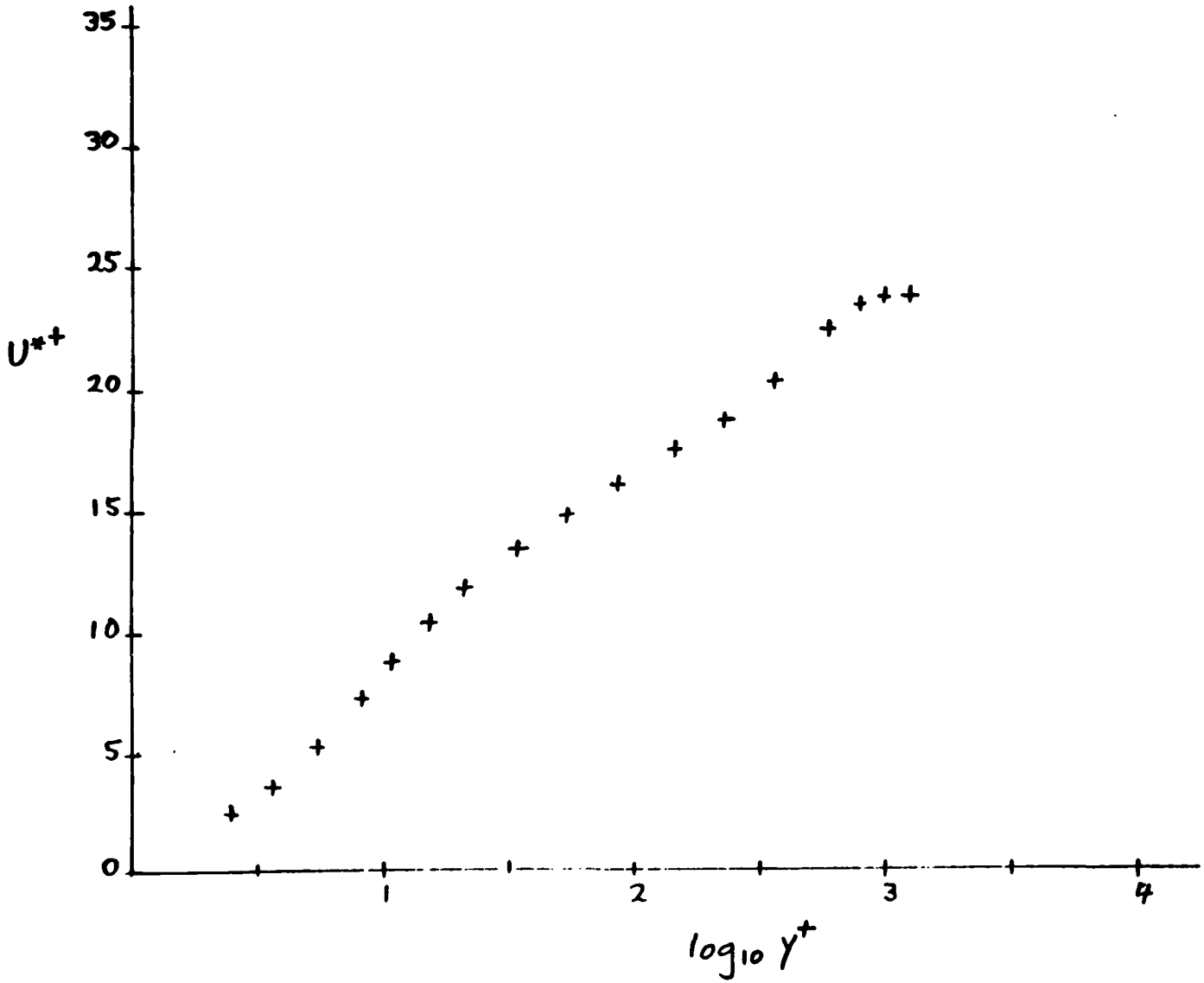

Figure 23. Case 8101 (Supersonic flat-plate boundary layer)
Mean velocity profile in law-of-the-wall coordinates, M = 5 .

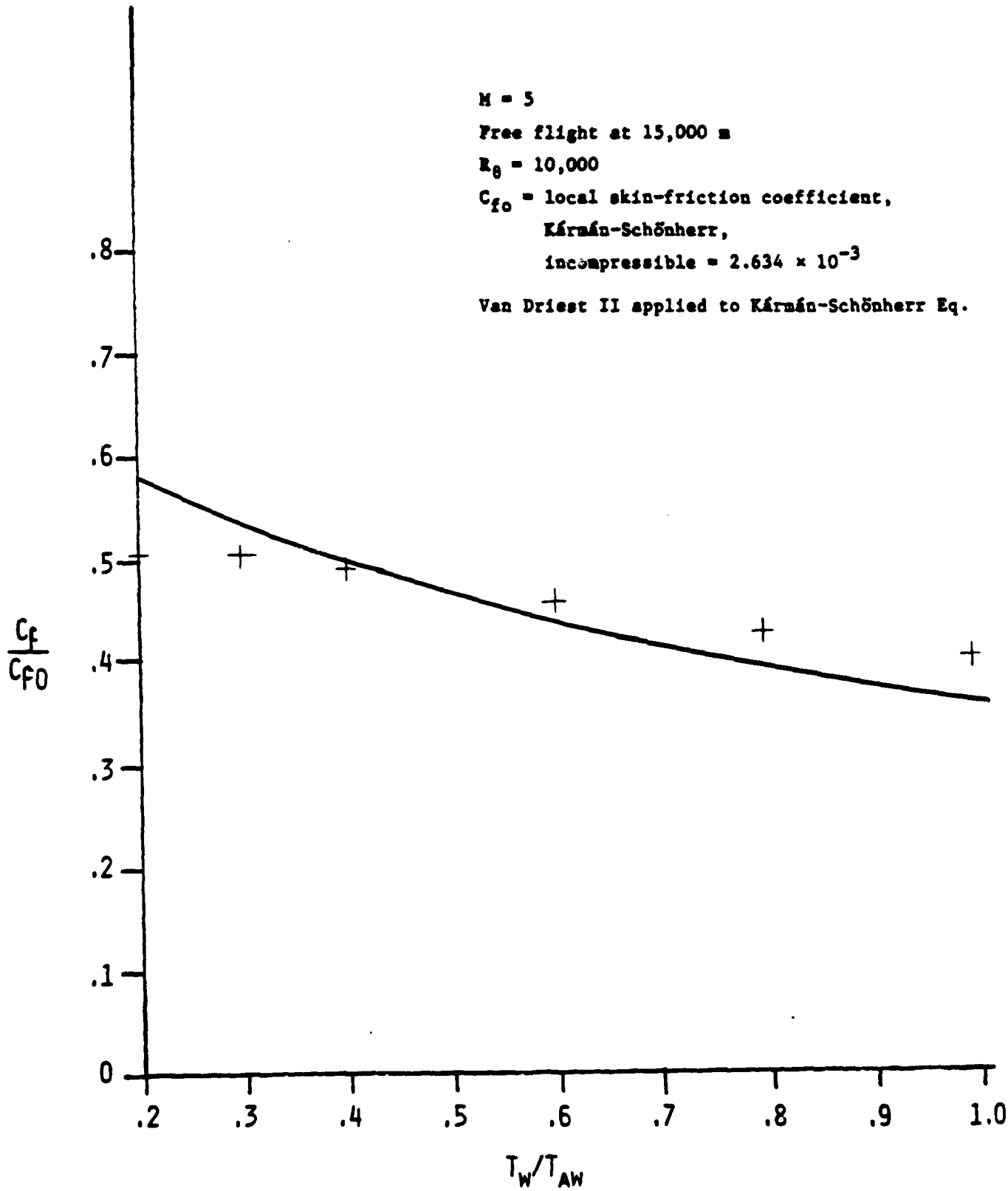

Figure 24. Case 8201 (Supersonic flat-plate boundary layer)
Coefficient of friction as a function of wall temperature.

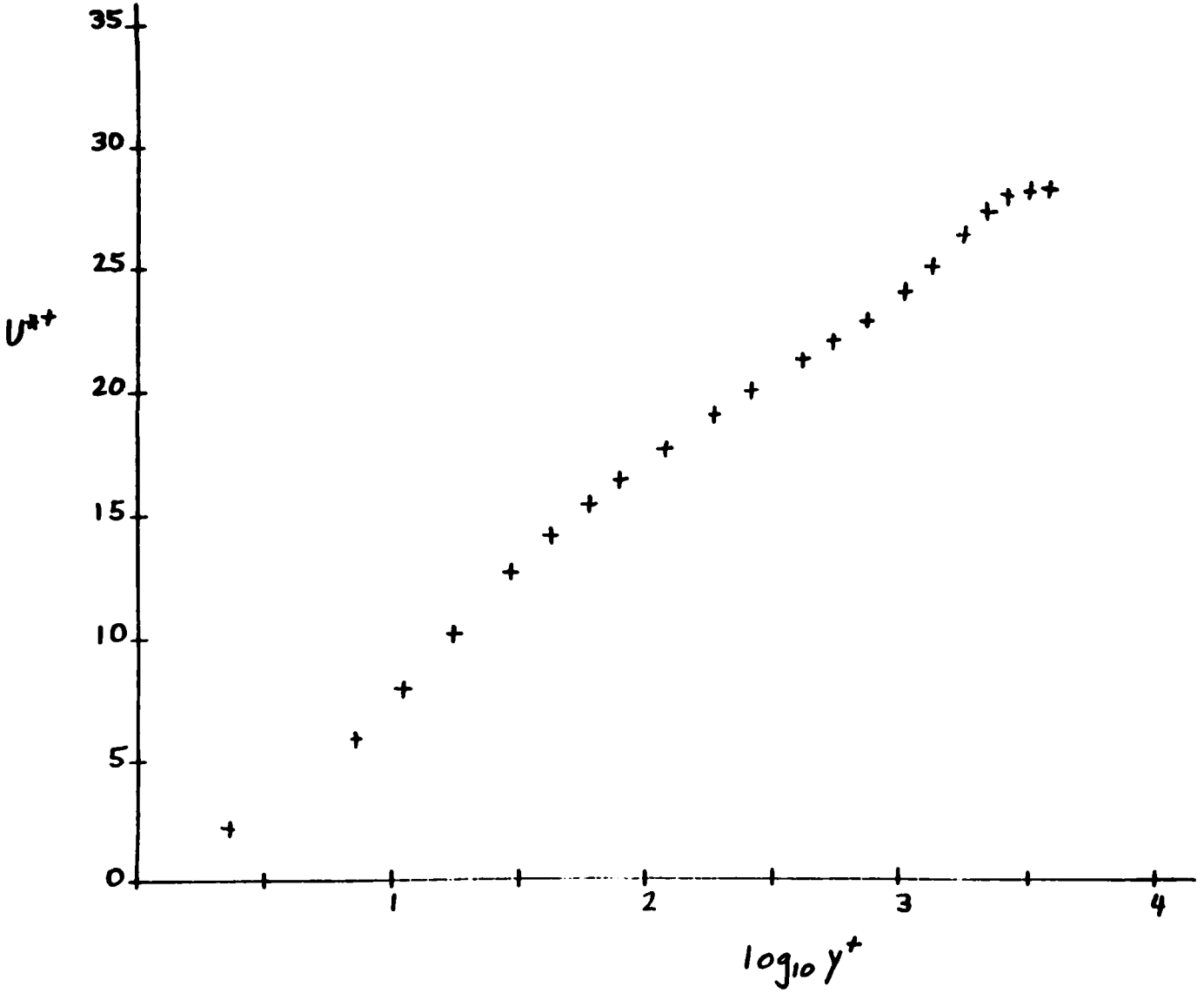

Figure 25. Case 8201 (Supersonic flat-plate boundary layer)
Mean velocity profile in law-of-the-wall coordinates, Tw/Taw = .3 .

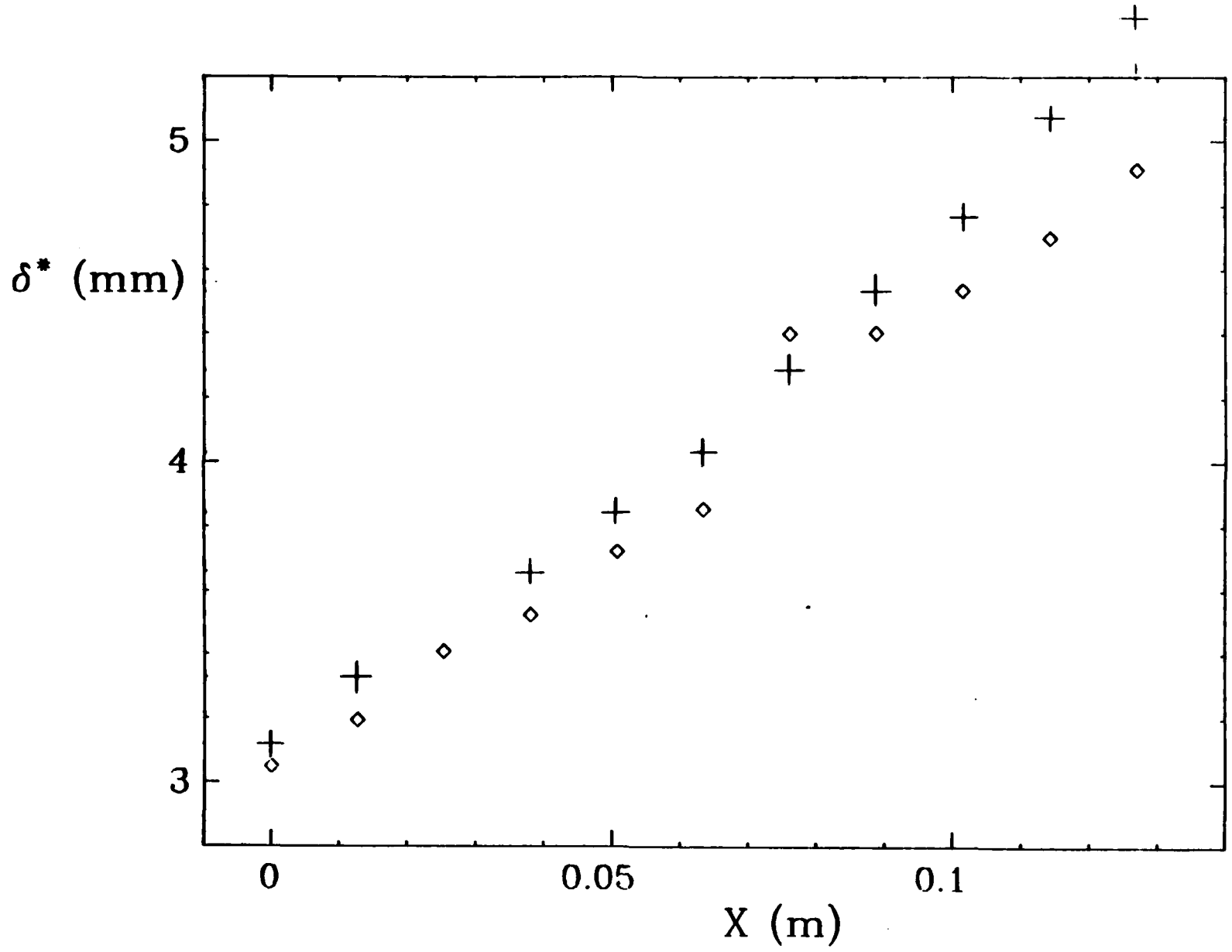

Figure 26. Case 8301 (Supersonic flat-plate boundary layer with favorable pressure gradient and blowing) Displacement thickness.

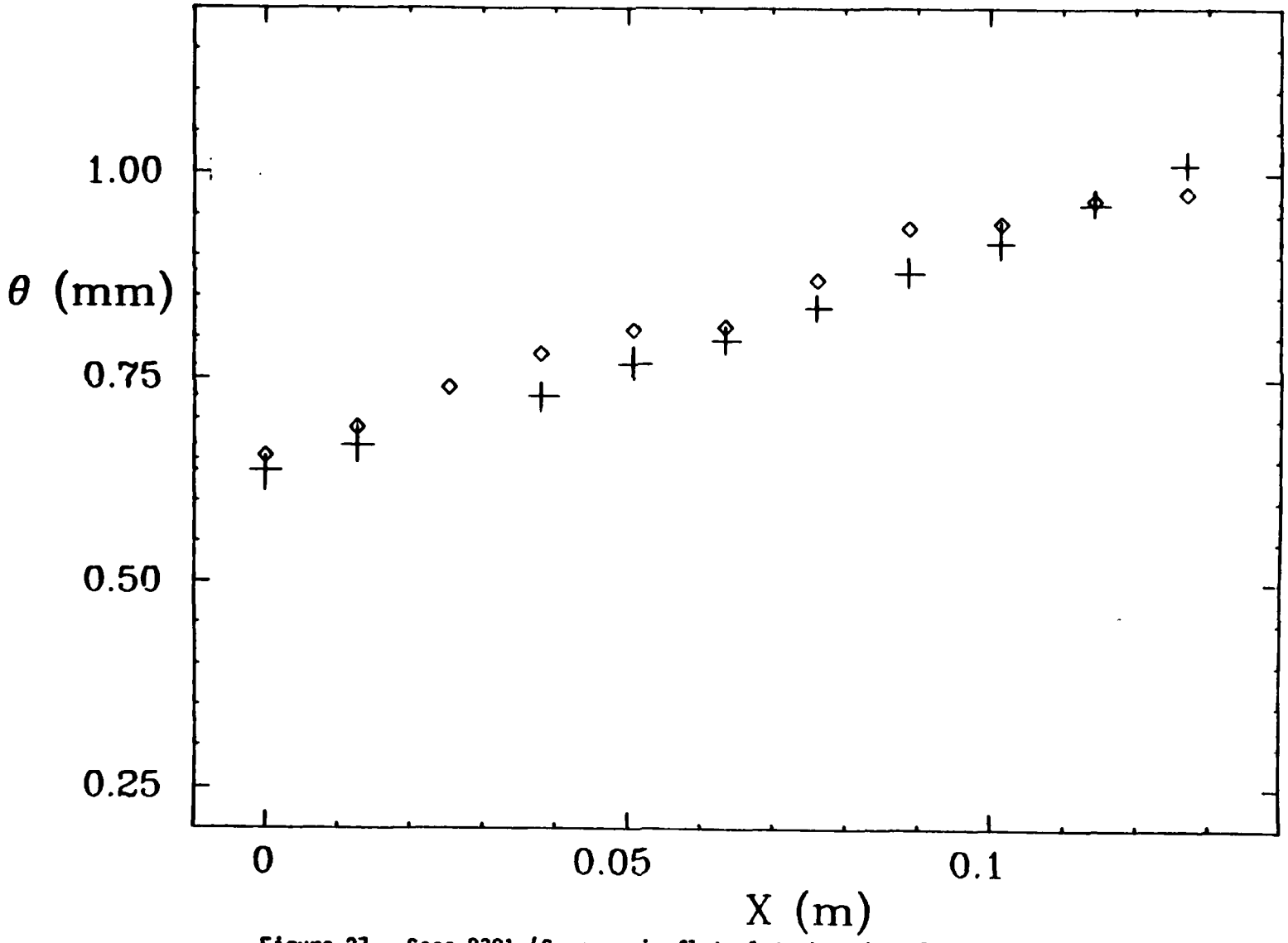

Figure 27. Case 8301 (Supersonic flat-plate boundary layer with favorable pressure gradient and blowing) Momentum thickness.

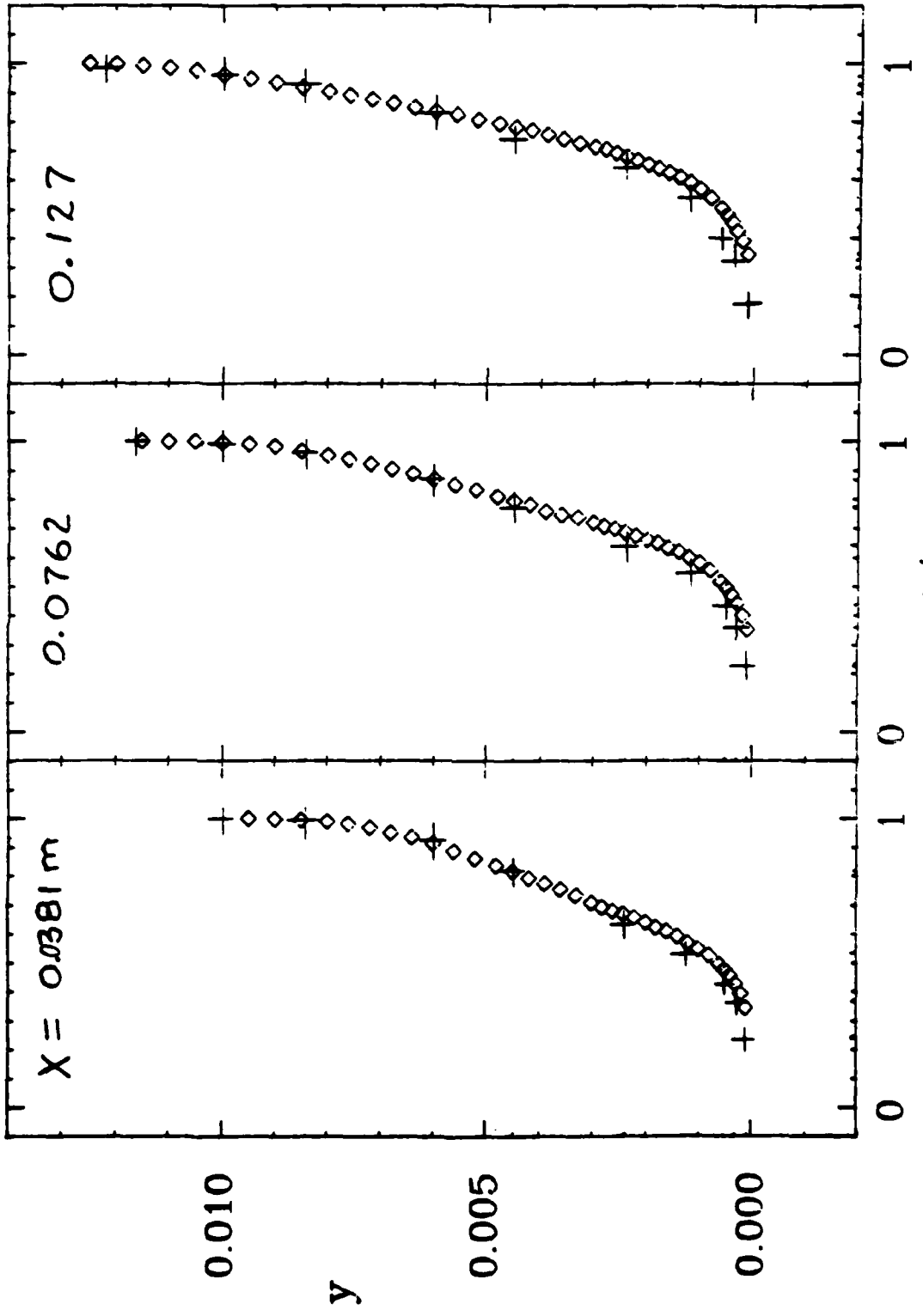

Figure 28. Case 8301 (Supersonic flat-plate boundary layer with favorable pressure gradient and blowing) Mean velocity profiles.

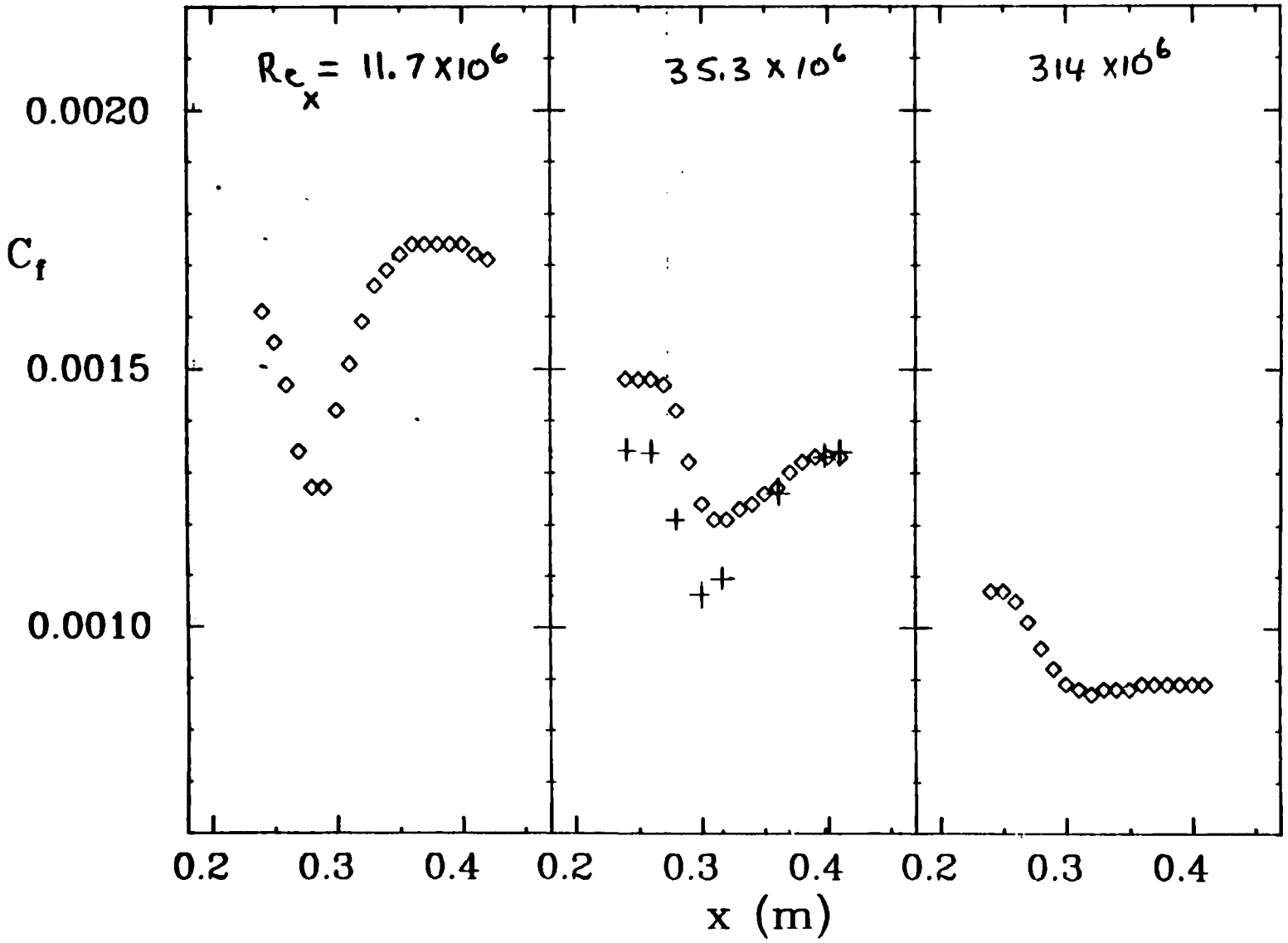

Figure 29. Case 8403 (Supersonic boundary layer inside a cylinder with adverse pressure gradient, centerbody II) Coefficient of friction.

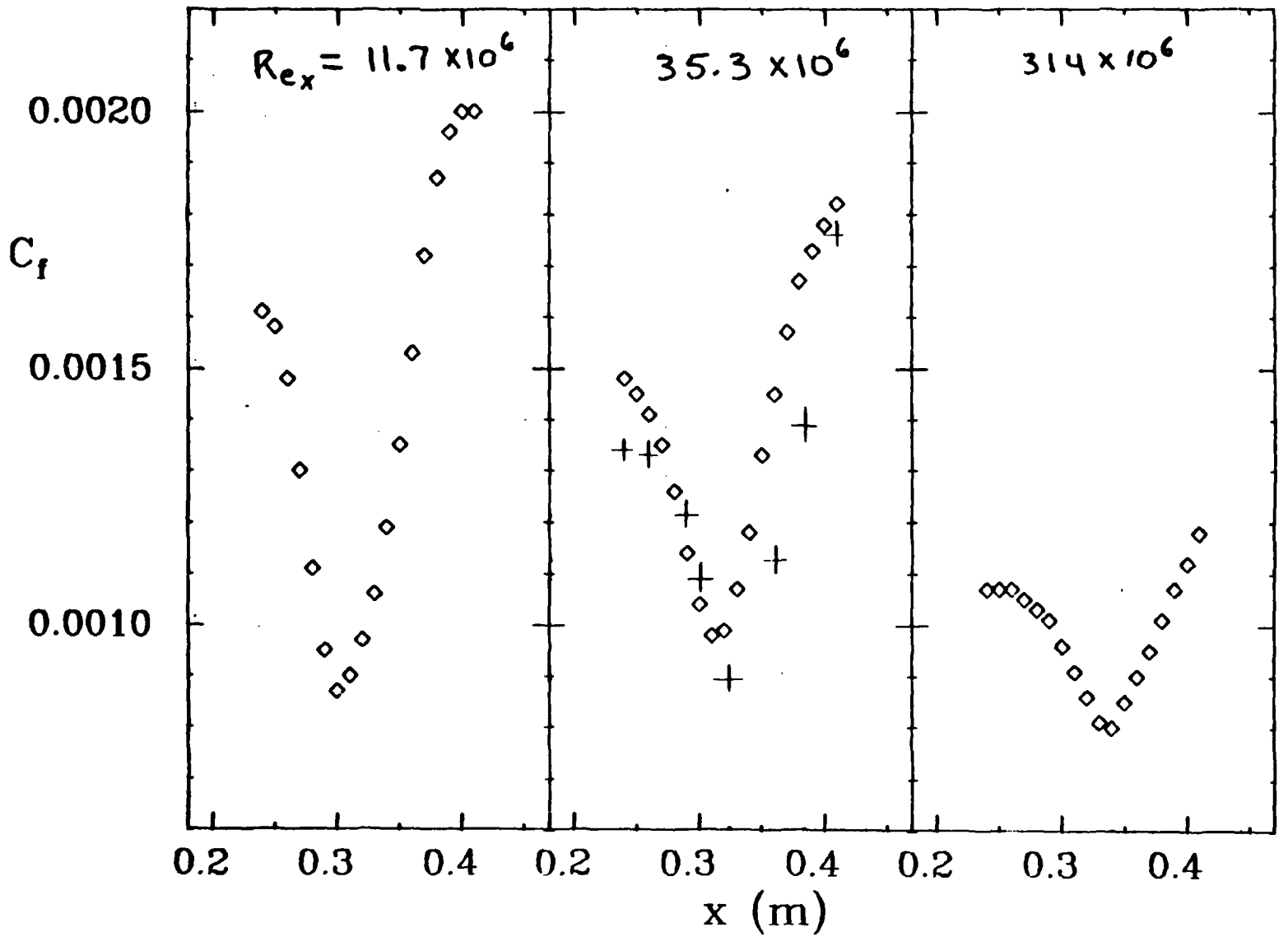

Figure 30. Case 8403 (Supersonic boundary layer inside a cylinder with adverse pressure gradient, centerbody IV) Coefficient of friction.

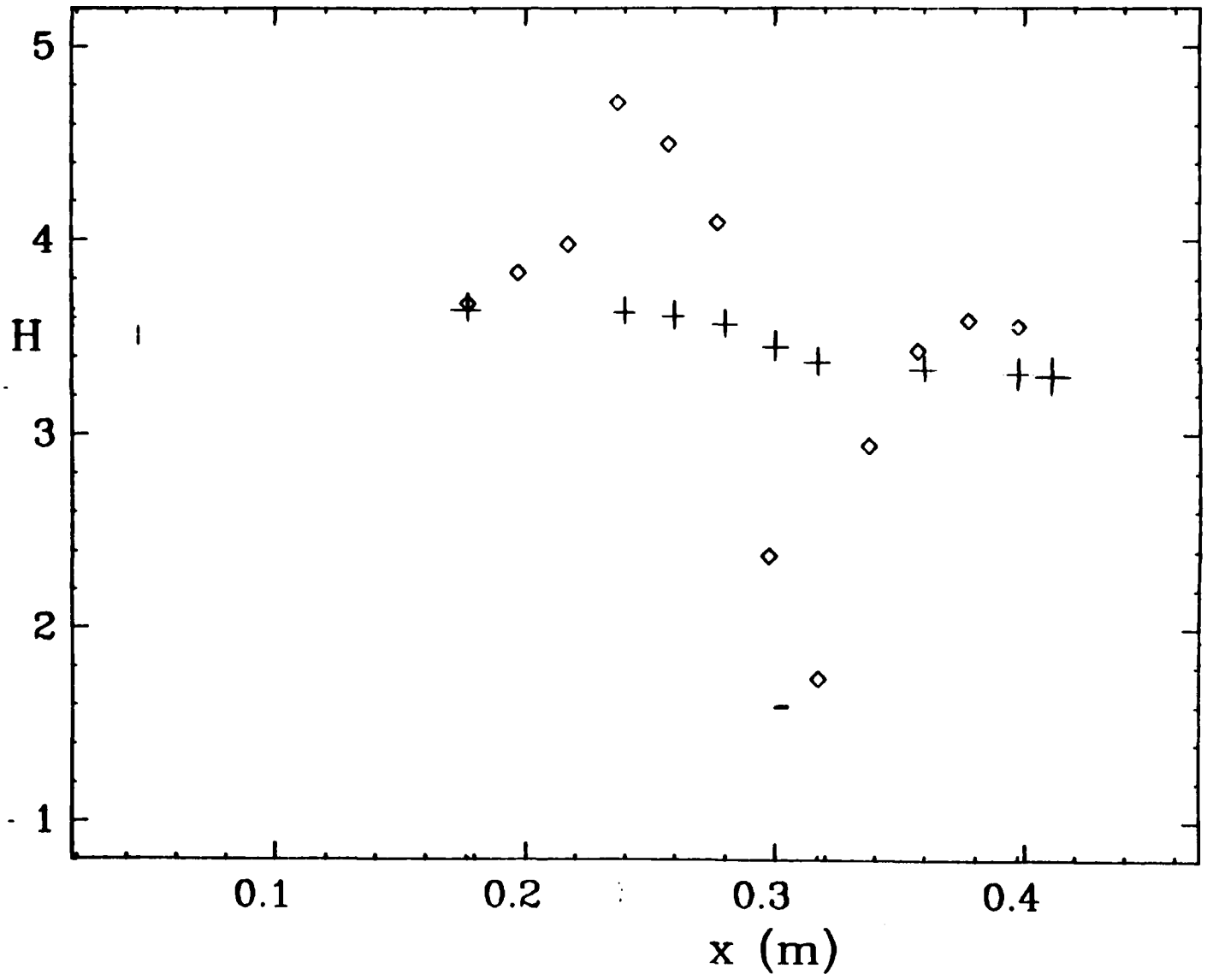

Figure 31. Case 8403 (Supersonic boundary layer inside a cylinder with adverse pressure gradient, centerbody II) Shape factor.

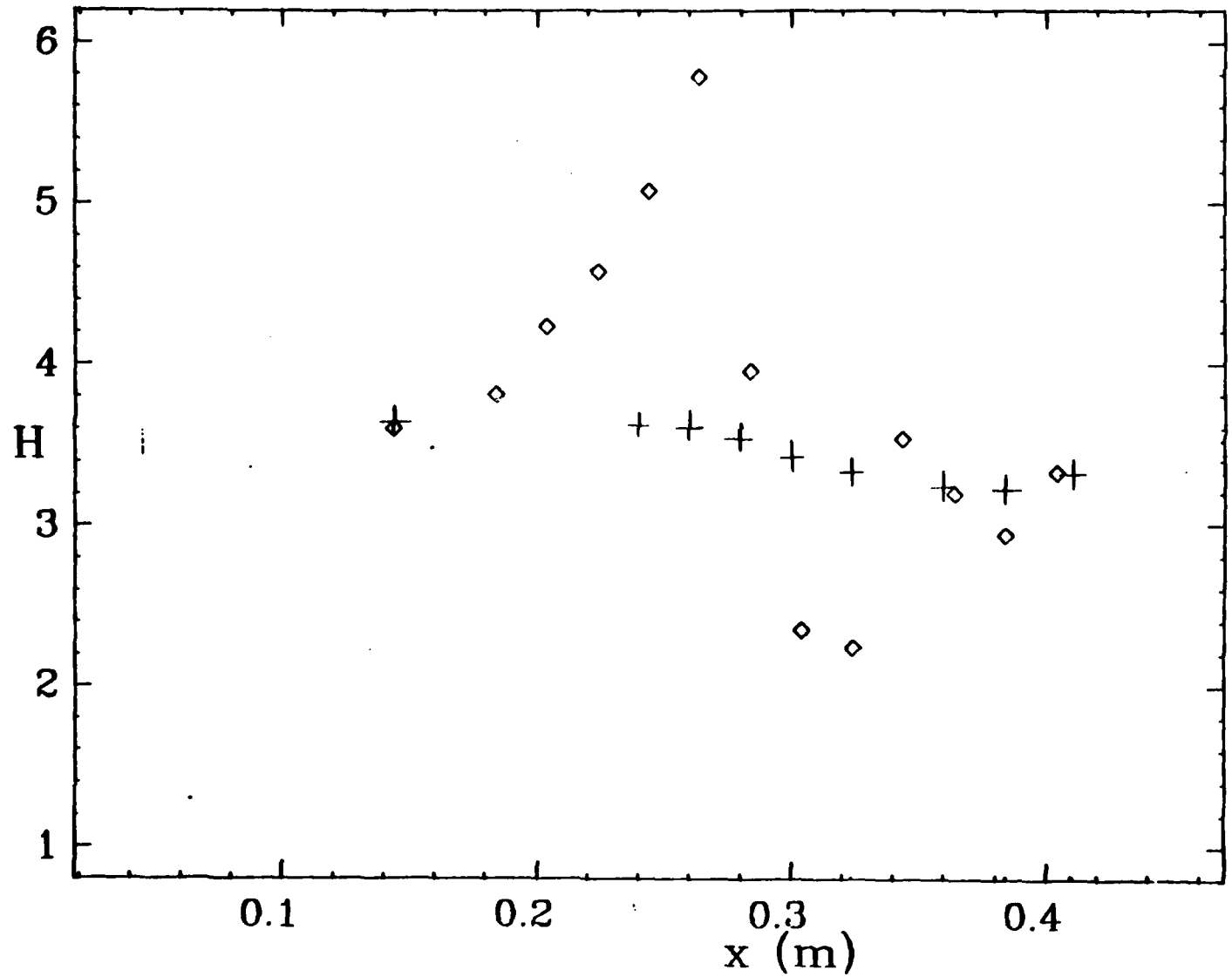

Figure 32. Case 8403 (Supersonic boundary layer inside a cylinder with adverse pressure gradient, centerbody IV) Shape factor.

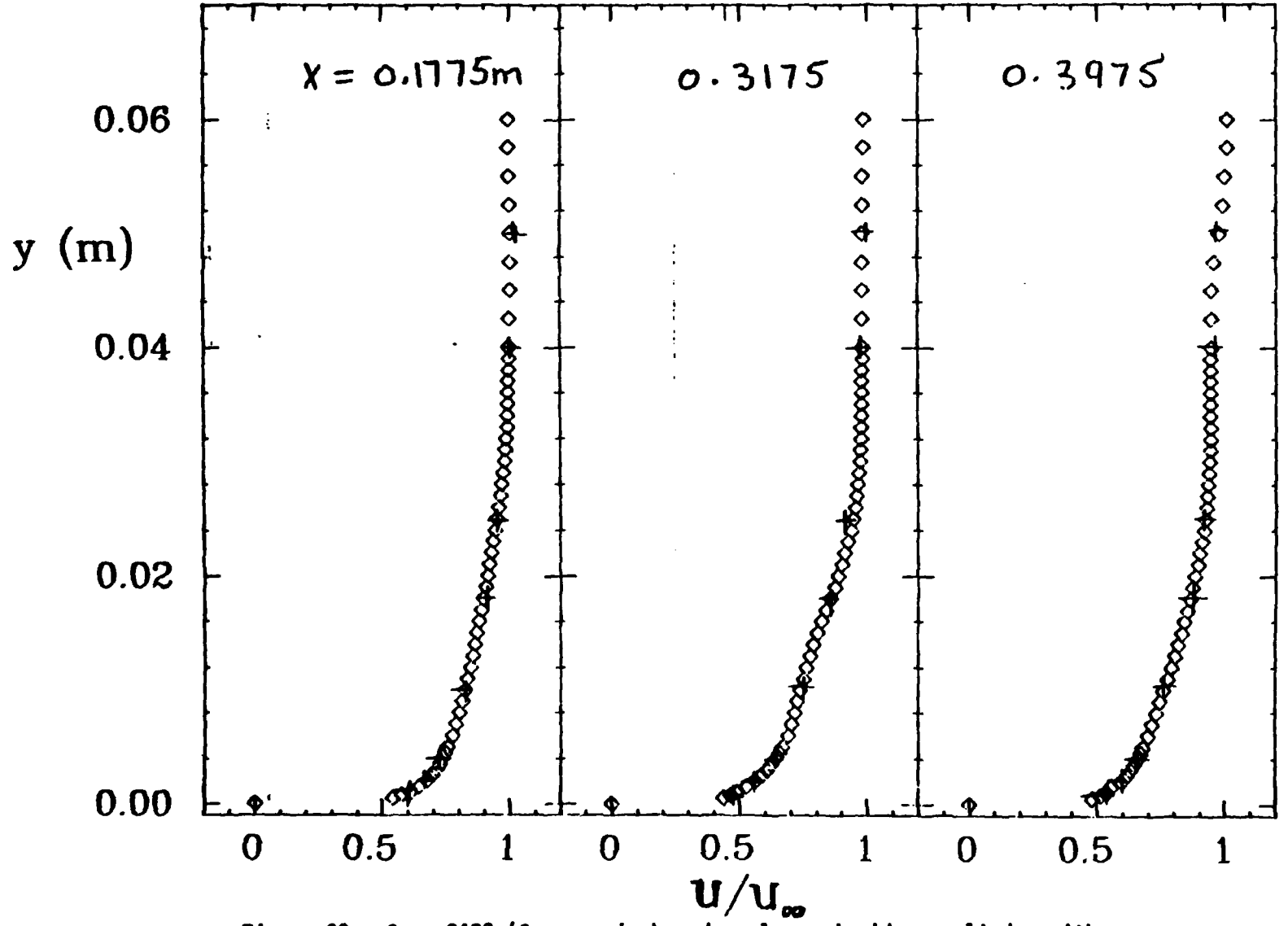

Figure 33. Case 8403 (Supersonic boundary layer inside a cylinder with adverse pressure gradient, centerbody II) Mean velocity profiles.

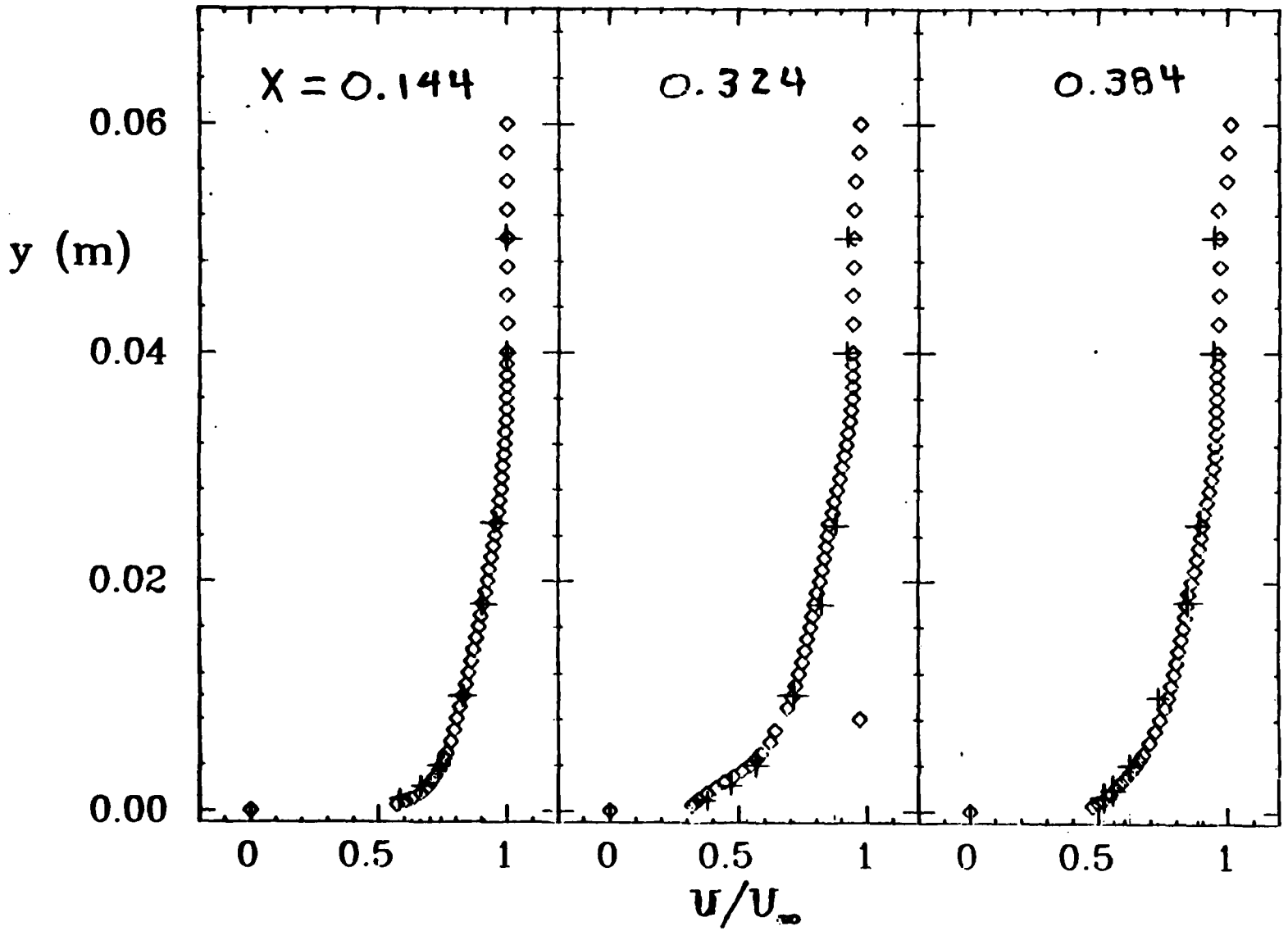

Figure 34. Case 8403 (Supersonic boundary layer inside a cylinder with adverse pressure gradient, centerbody IV) Mean velocity profiles.

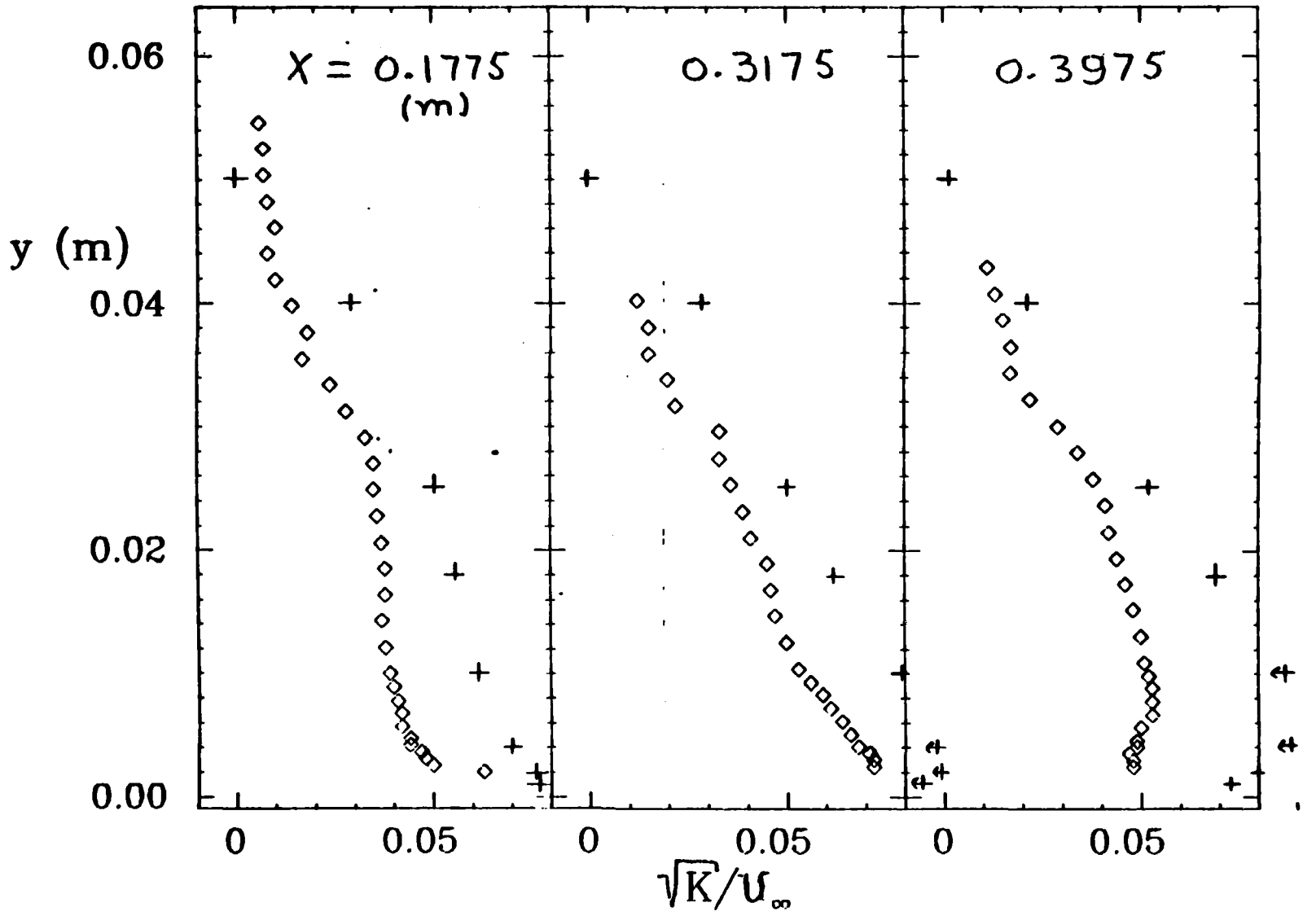

Figure 35. Case 8403 (Supersonic boundary layer inside a cylinder with adverse pressure gradient, centerbody II) Turbulence profiles.

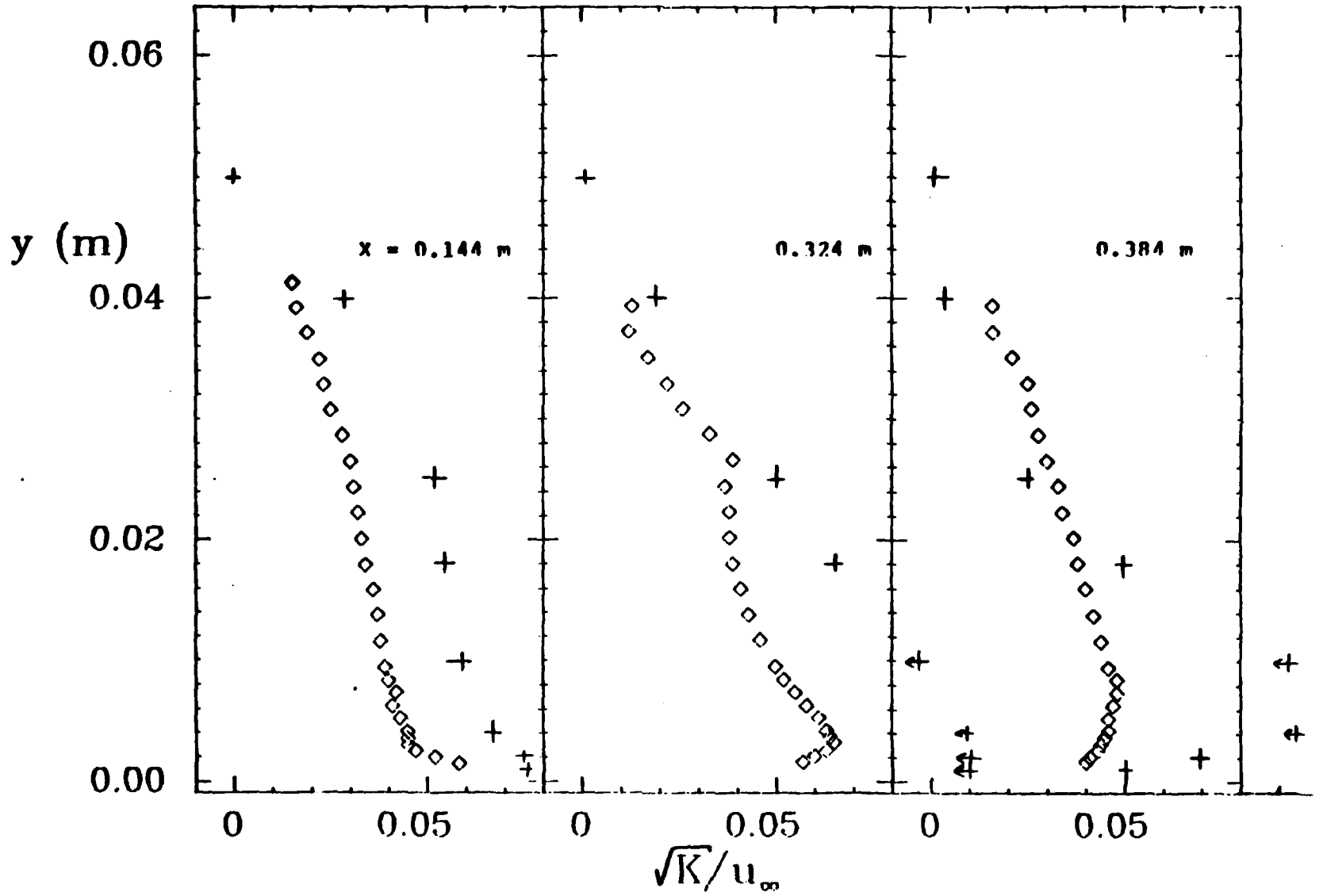

Figure 36. Case 8403 (Supersonic boundary layer inside a cylinder with adverse pressure gradient, centerbody IV) Turbulence profiles.

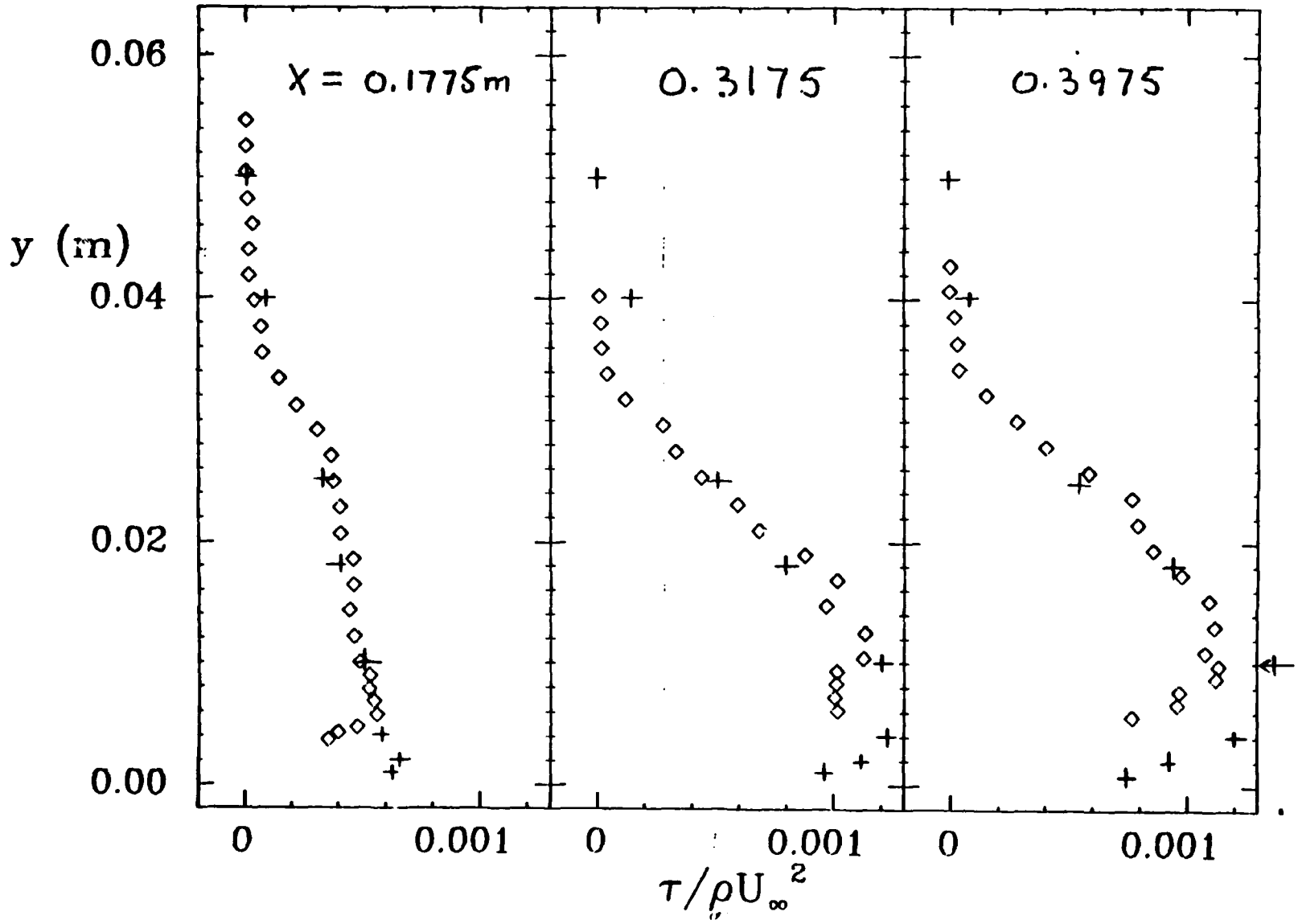

Figure 37. Case 8403 (Supersonic boundary layer inside a cylinder with adverse pressure gradient, centerbody II) Turbulent stress profiles.

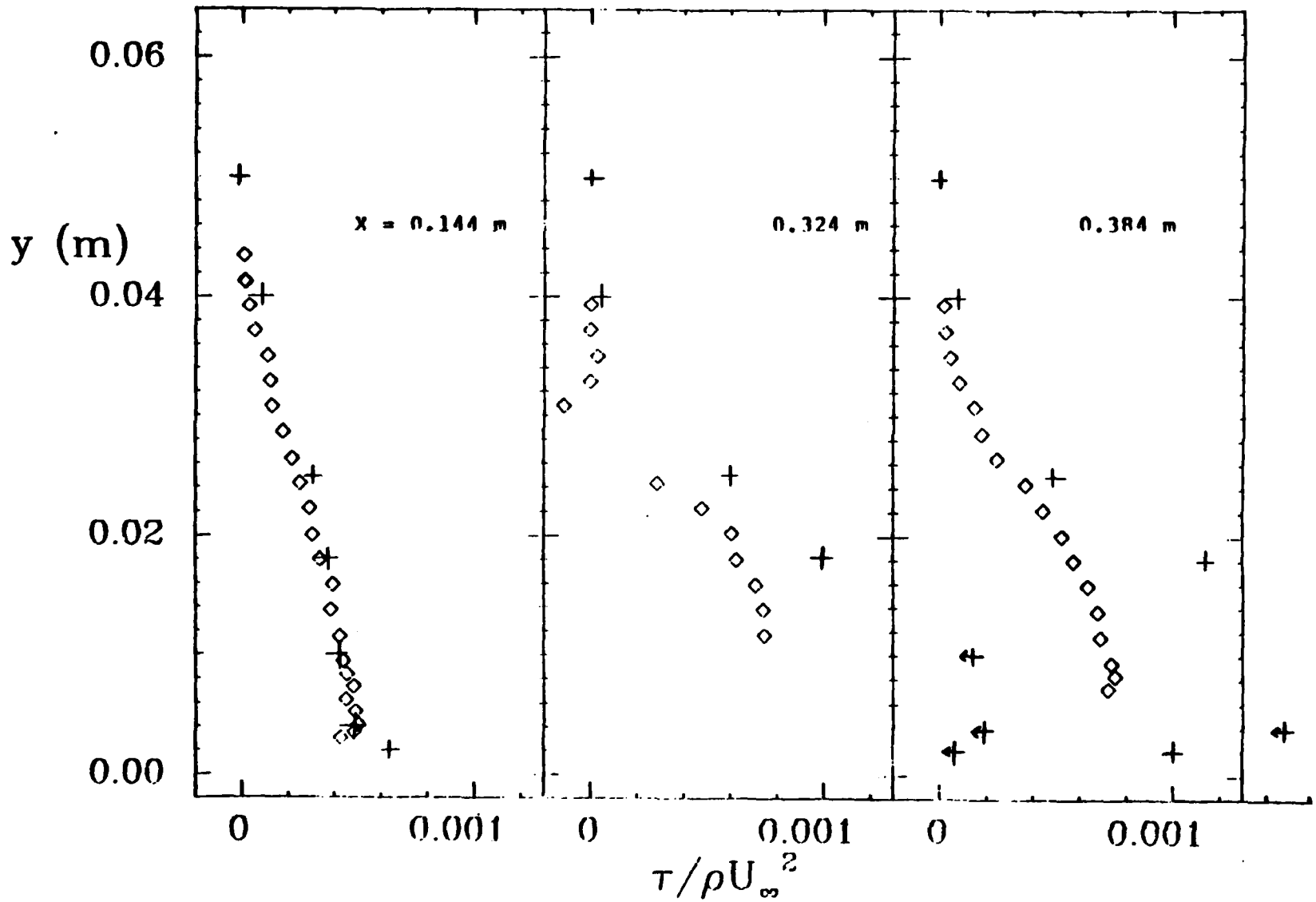

Figure 38. Case 8403 (Supersonic boundary layer inside a cylinder with adverse pressure gradient, centerbody IV) Turbulent stress profiles.

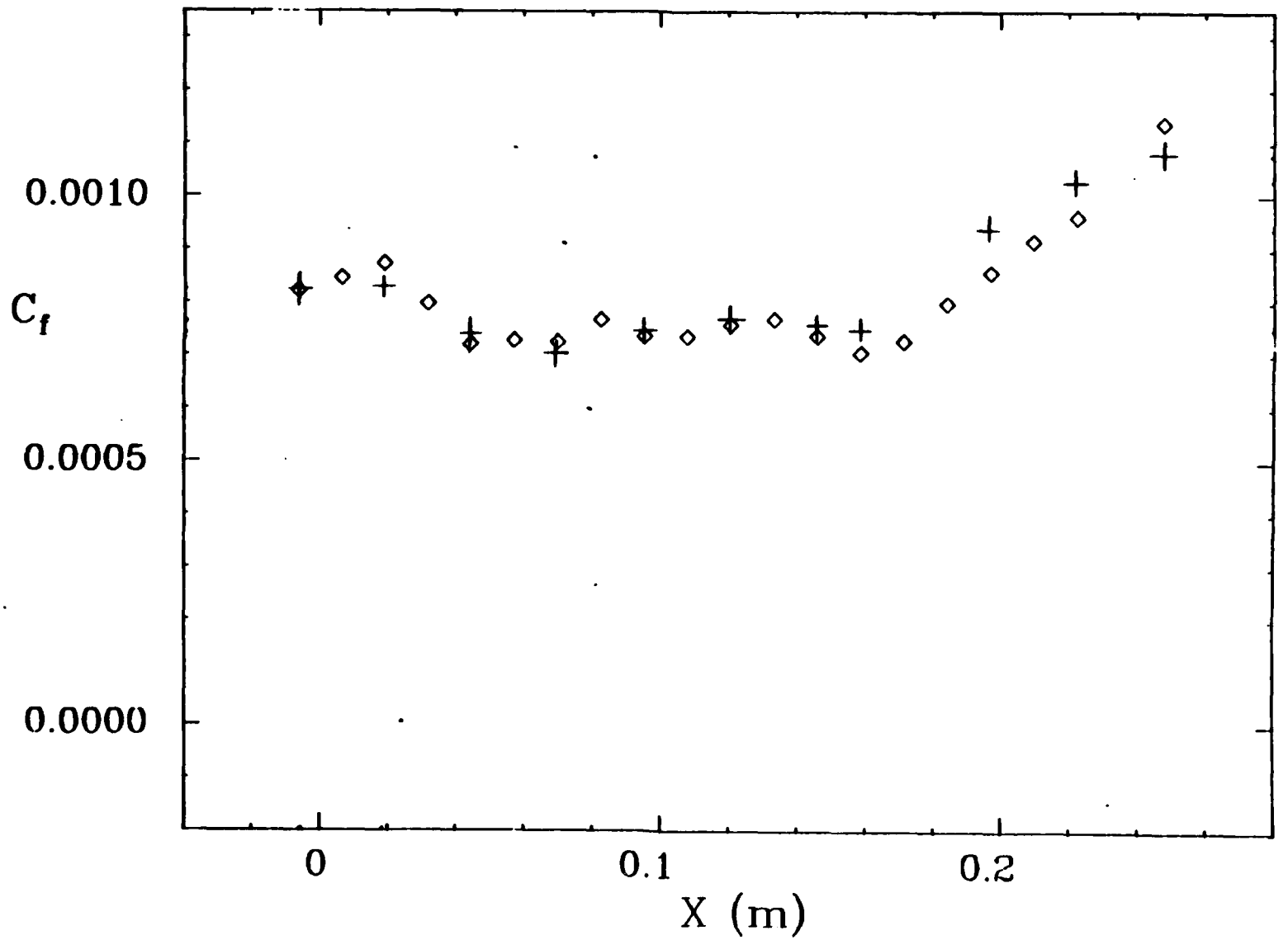

Figure 39. Case 8411 (Supersonic flat-plate boundary layer with adverse pressure gradient) Coefficient of friction.

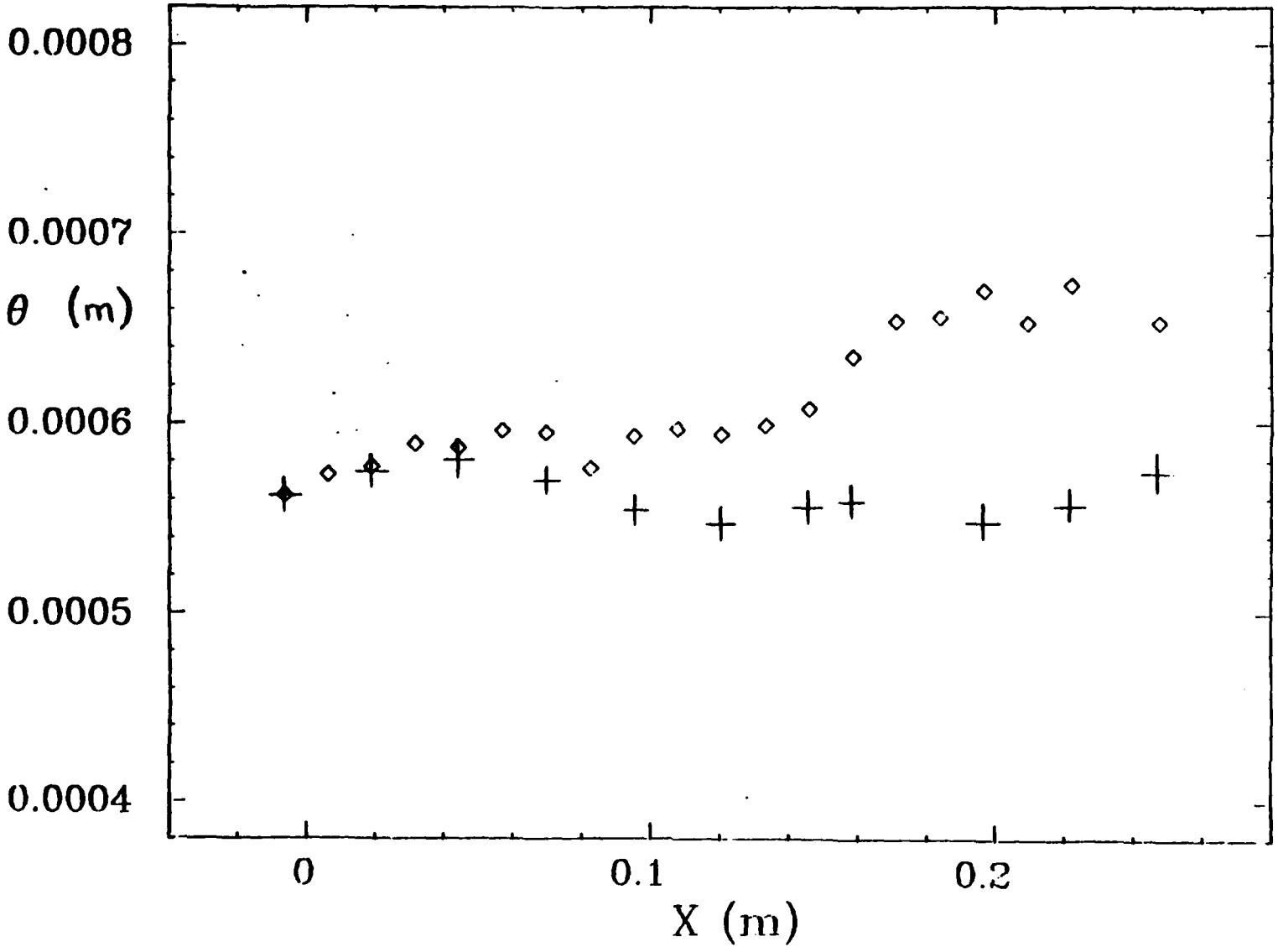

Figure 40. Case 8411 (Supersonic flat-plate boundary layer with adverse pressure gradient) Momentum thickness.

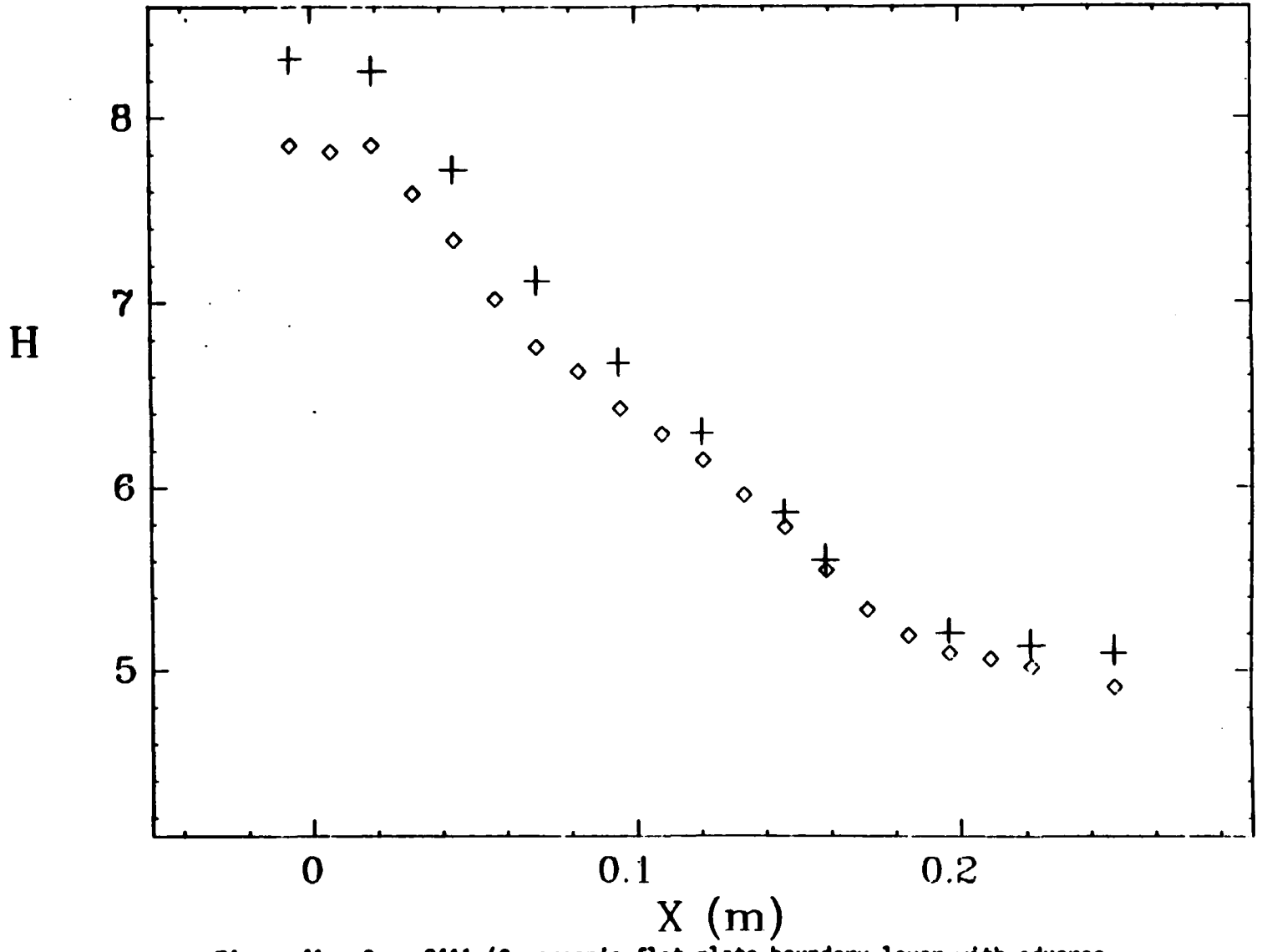

Figure 41. Case 8411 (Supersonic flat-plate boundary layer with adverse pressure gradient) Shape factor.

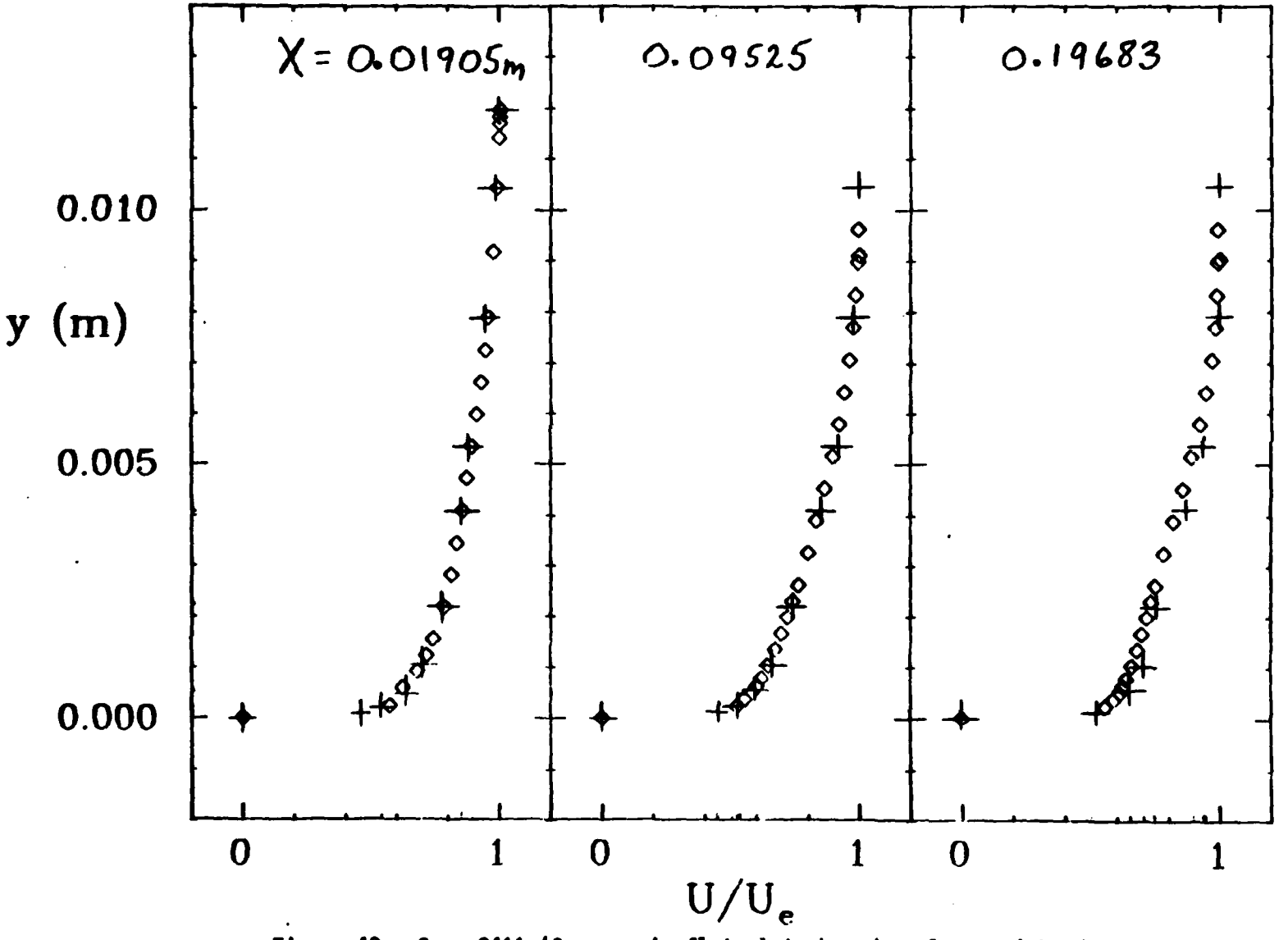

Figure 42. Case 8411 (Supersonic flat-plate boundary layer with adverse pressure gradient) Mean velocity profiles..

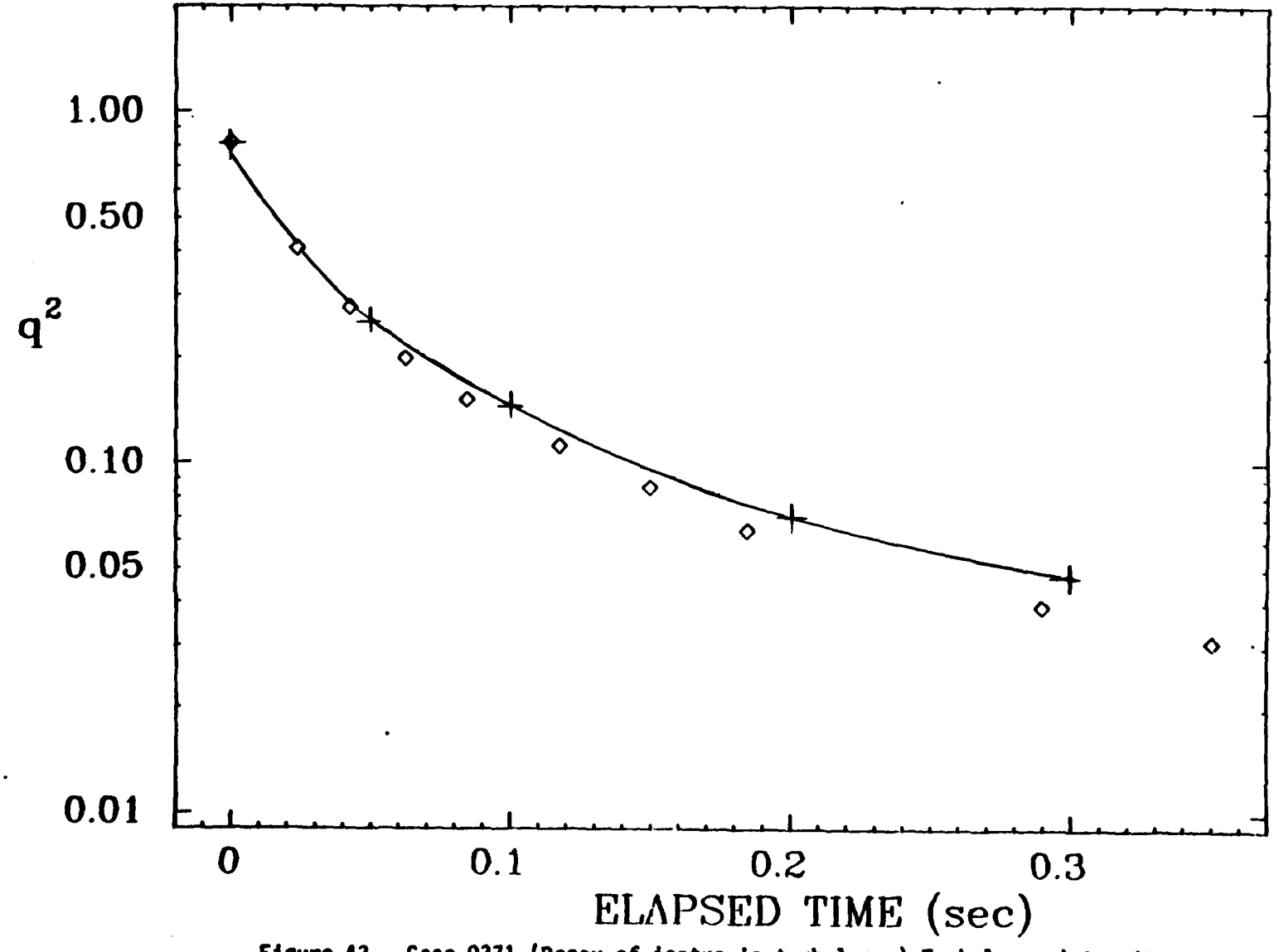

Figure 43. Case 0371 (Decay of isotropic turbulence) Turbulence intensity.

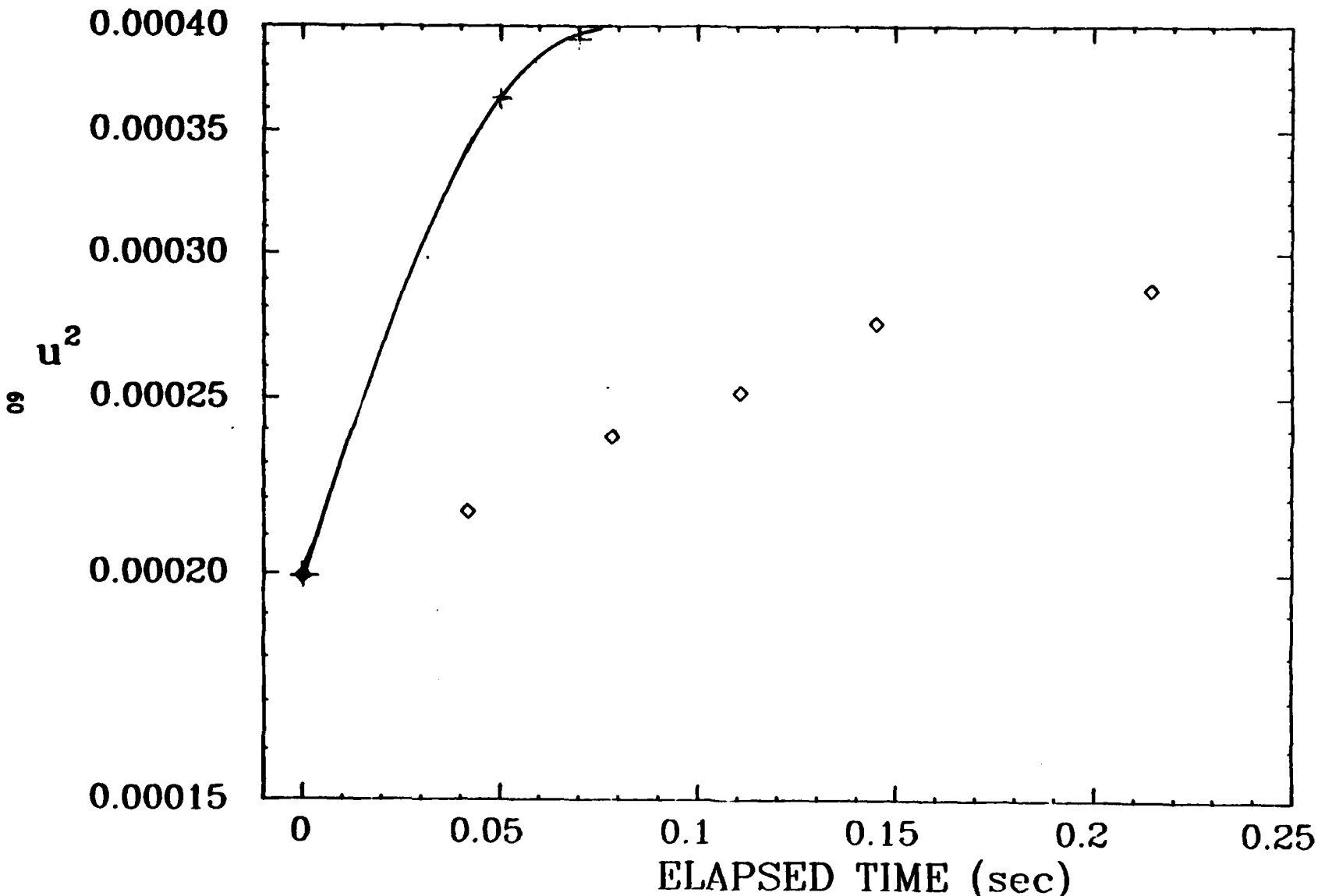

Figure 44. Case 0373A (Axisymmetric return to isotropy) Longitudinal correlation.

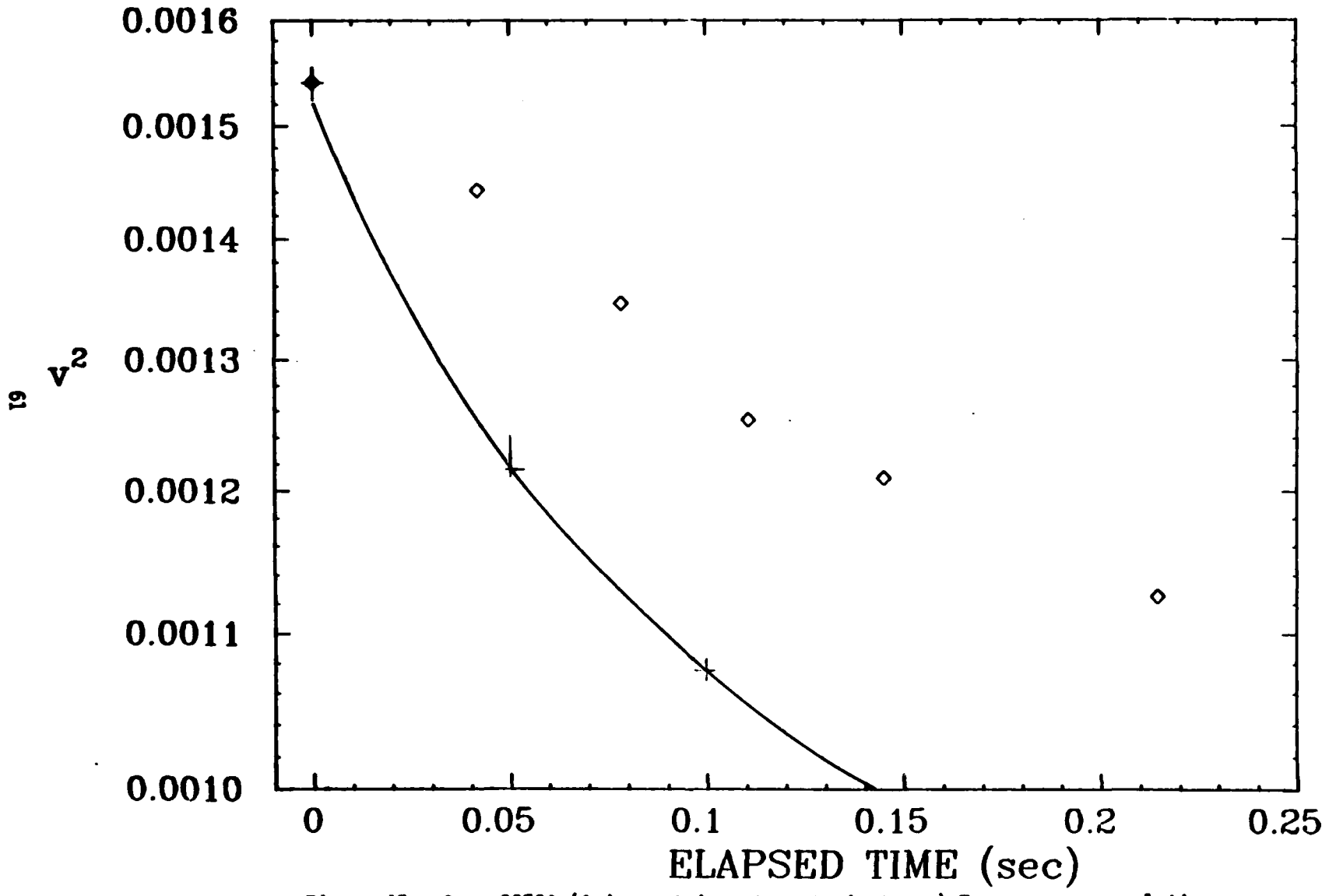

Figure 45. Case 0373A (Axisymmetric return to isotropy) Transverse correlation.

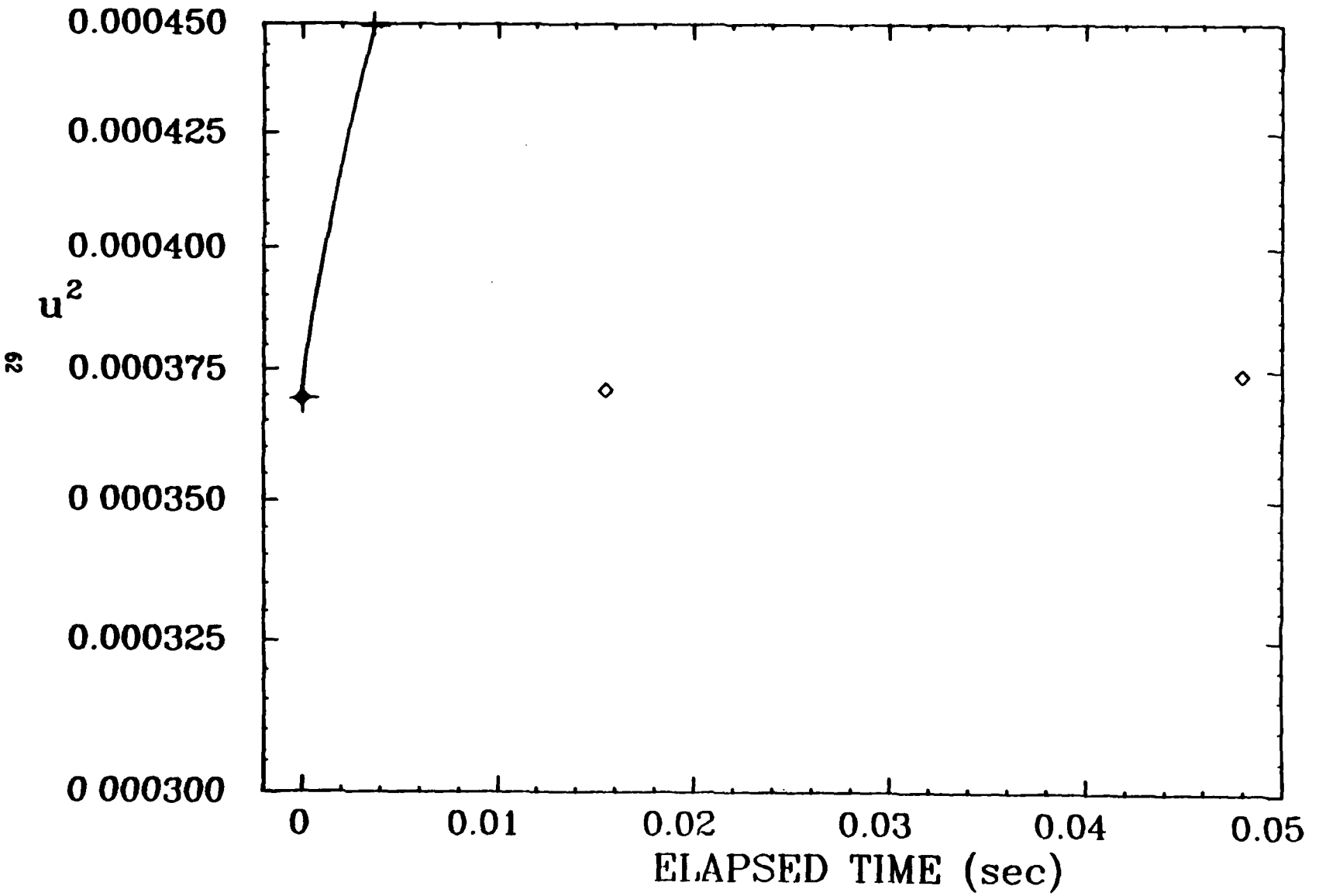

Figure 46. Case 0373B (Axisymmetric return to isotropy) Longitudinal correlation.

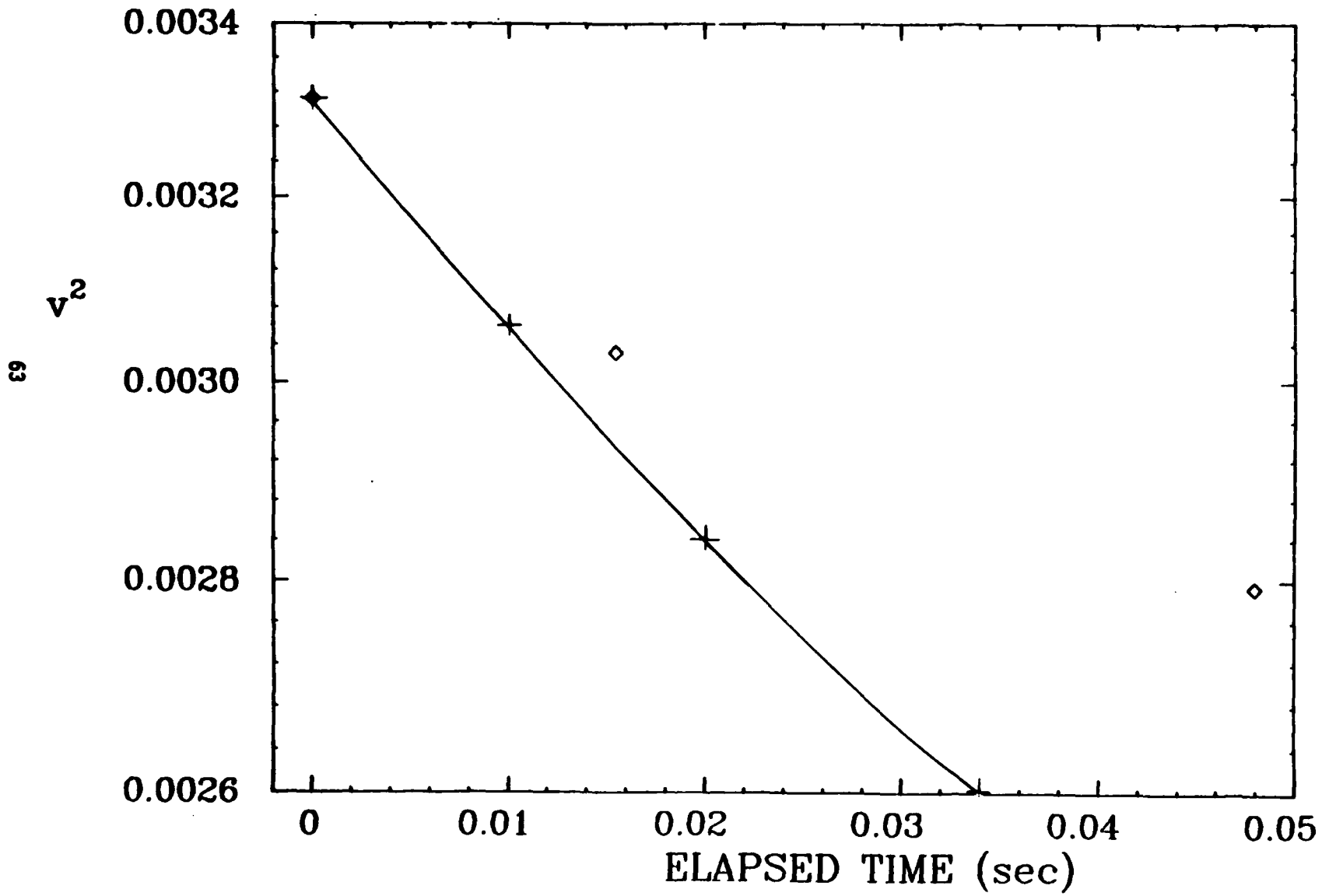

Figure 47. Case 0373B (Axisymmetric return to isotropy) Transverse correlation.

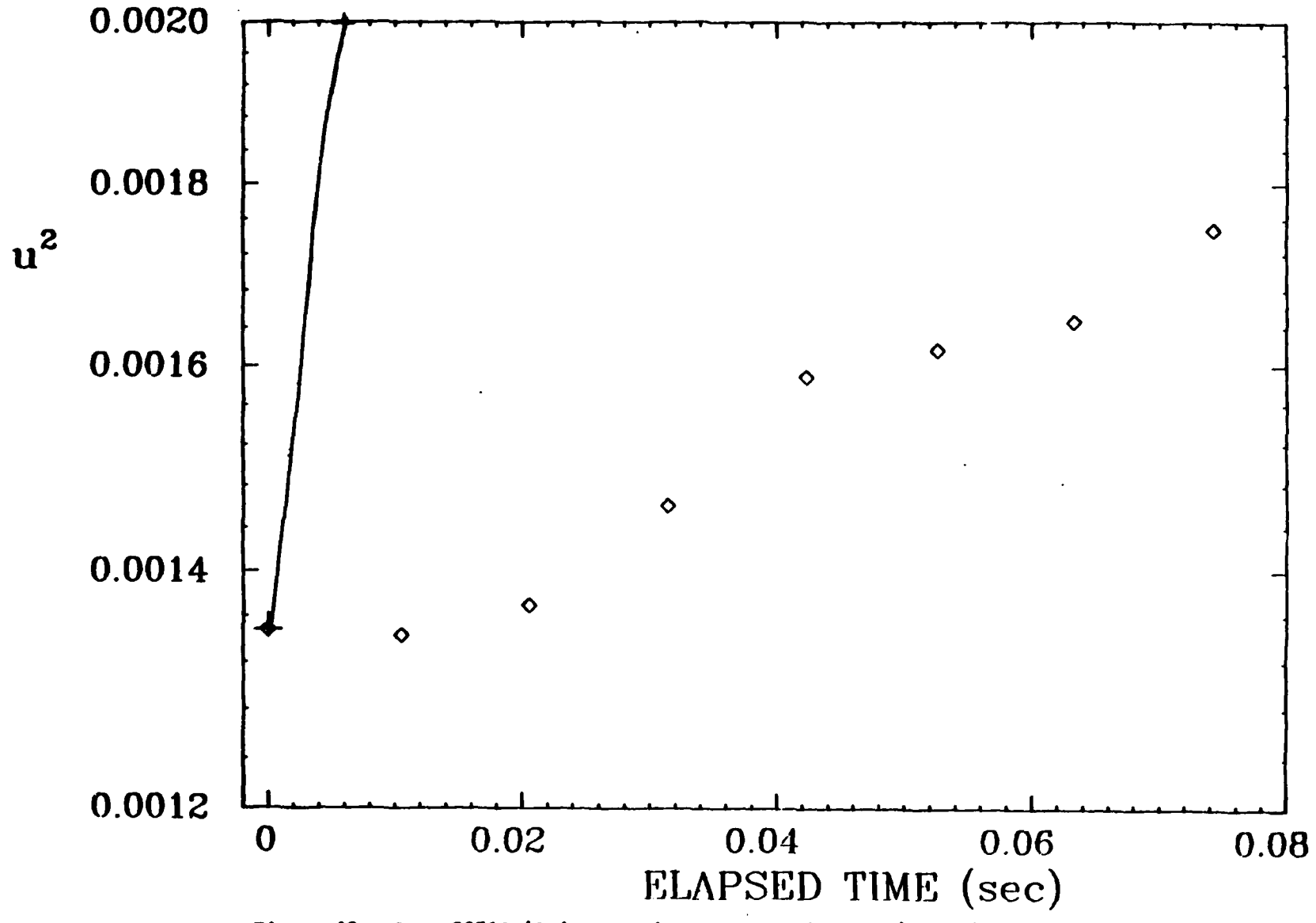

Figure 48. Case 0373C (Axisymmetric return to isotropy) Longitudinal correlation.

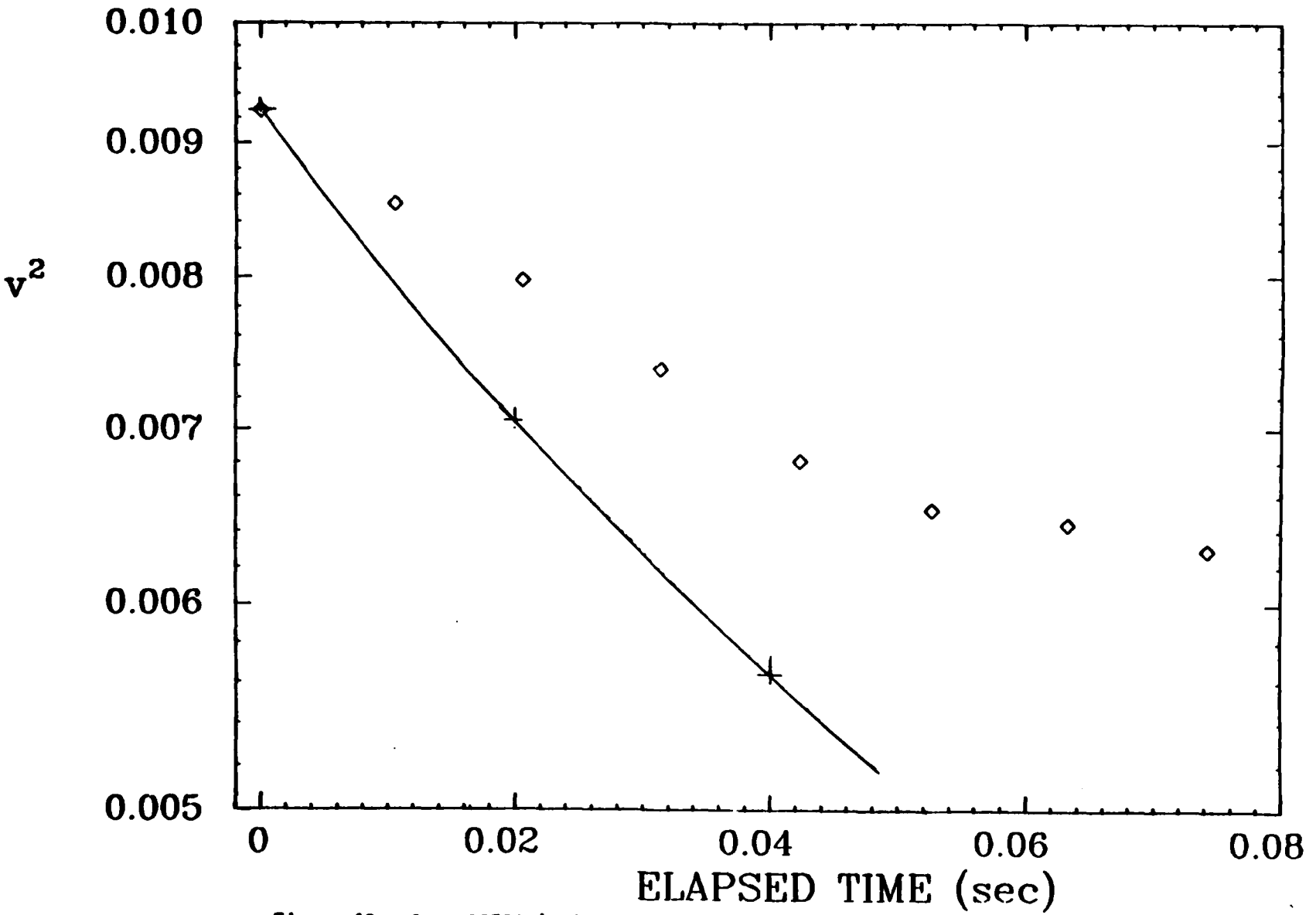

Figure 49. Case 0373C (Axisymmetric return to isotropy) Transverse correlation.

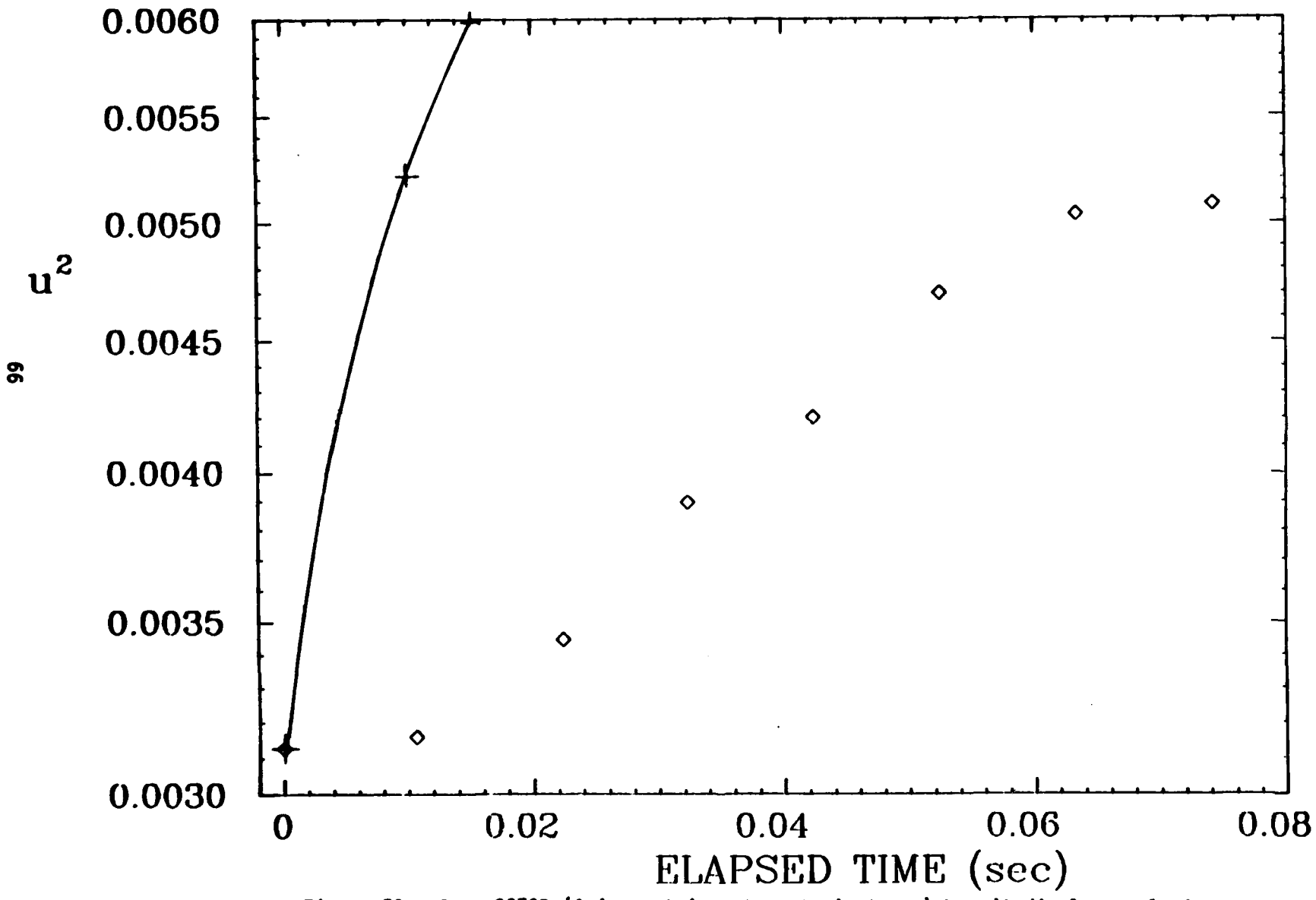

Figure 50. Case 0373D (Axisymmetric return to isotropy) Longitudinal correlation.

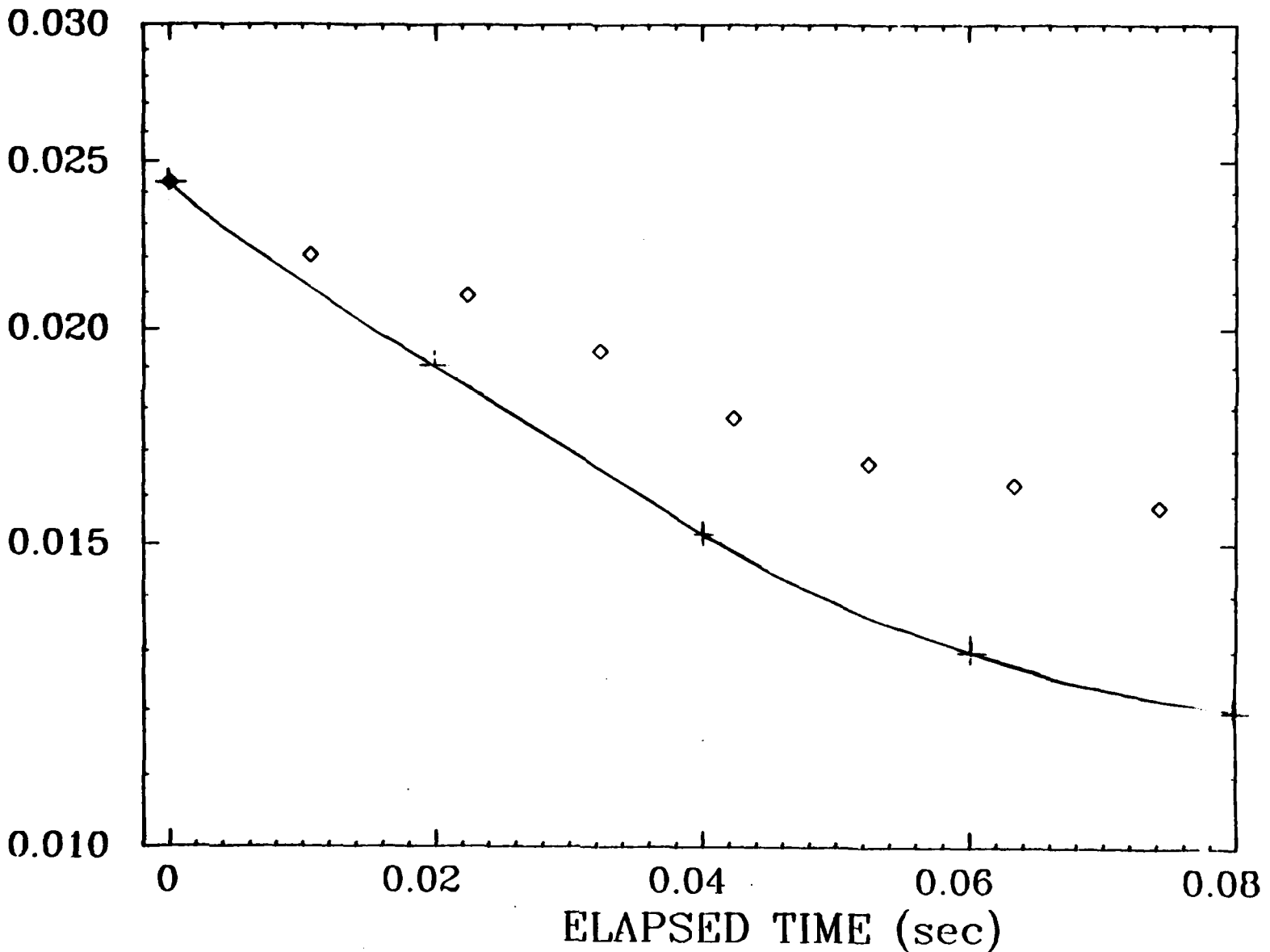

Figure 51. Case 0373D (Axisymmetric return to isotropy) Transverse correlation.

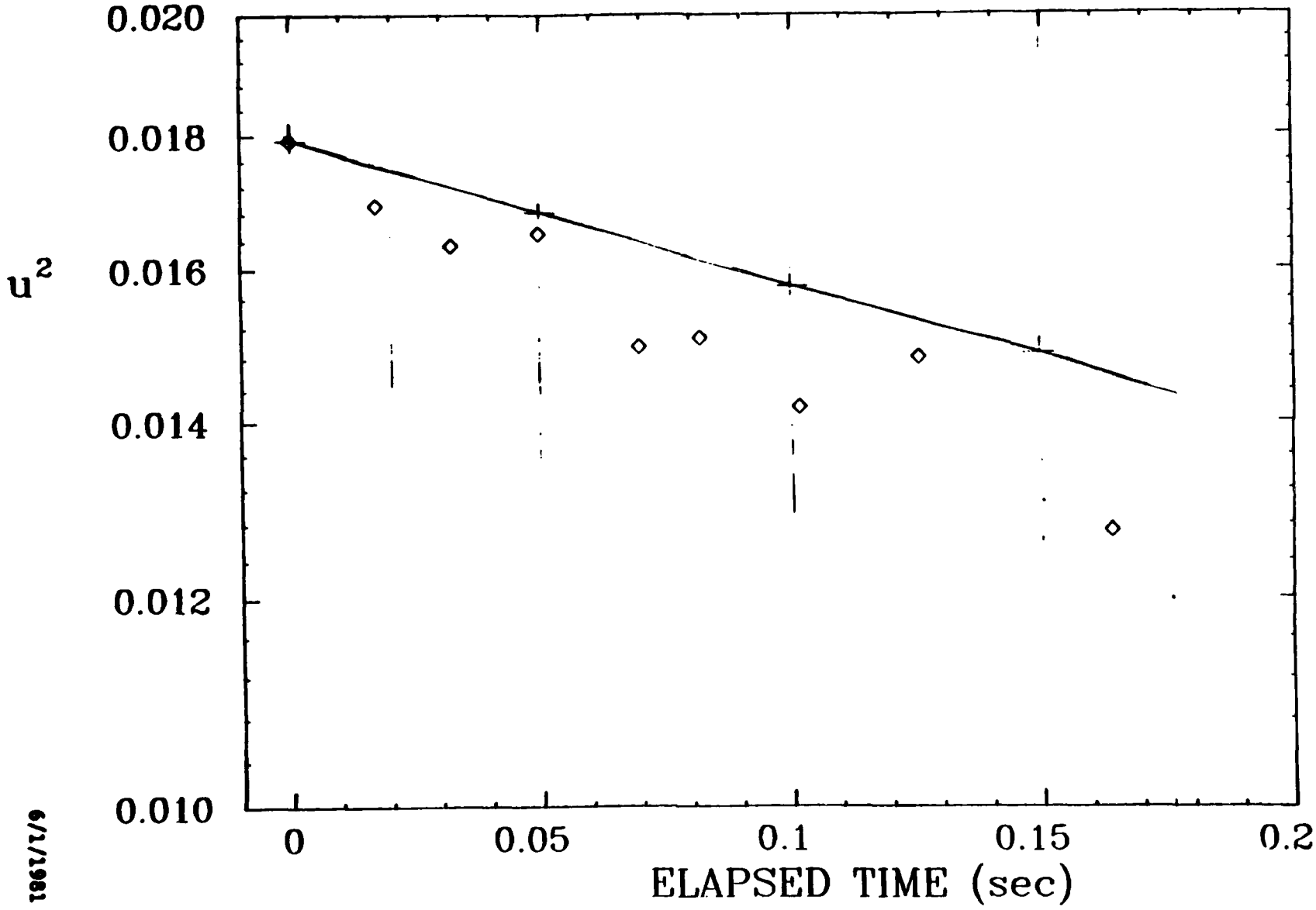

Figure 52. Case 0373E (Plane return to isotropy) Longitudinal correlation.

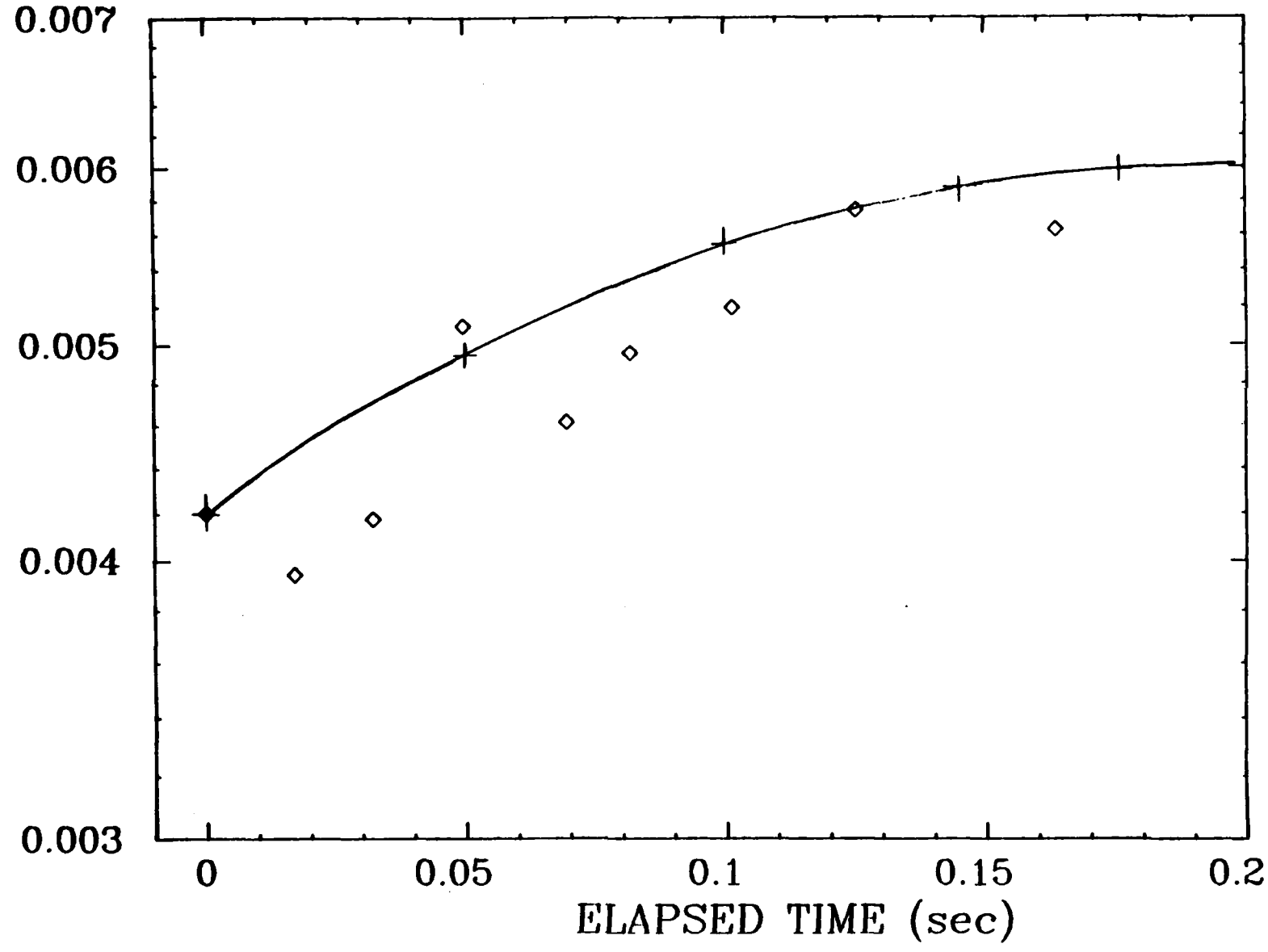

Figure 53. Case 0373E (Plane return to isotropy) Transverse correlation.

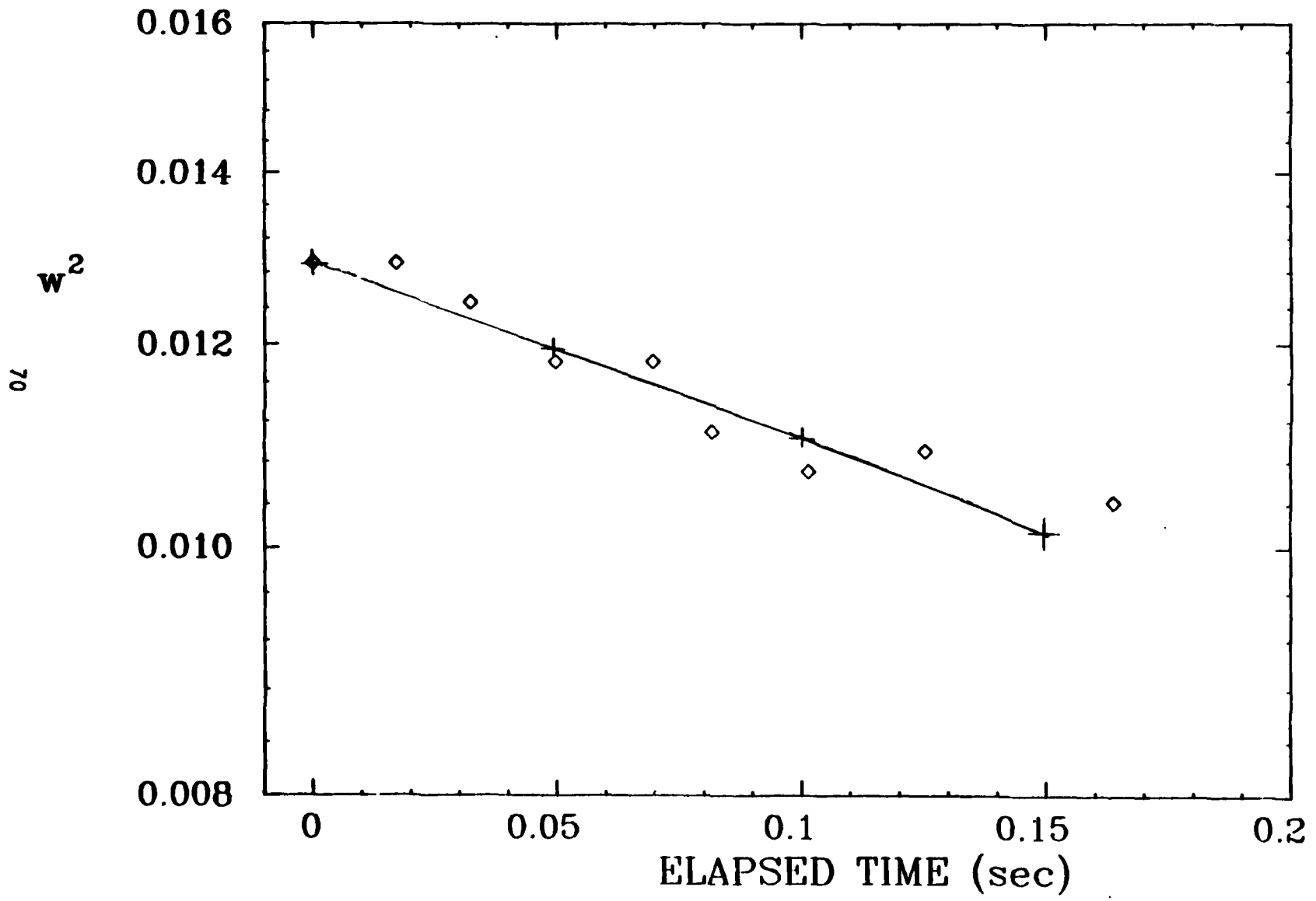

Figure 54. Case 0373E (Plane return to isotropy) Transverse correlation.

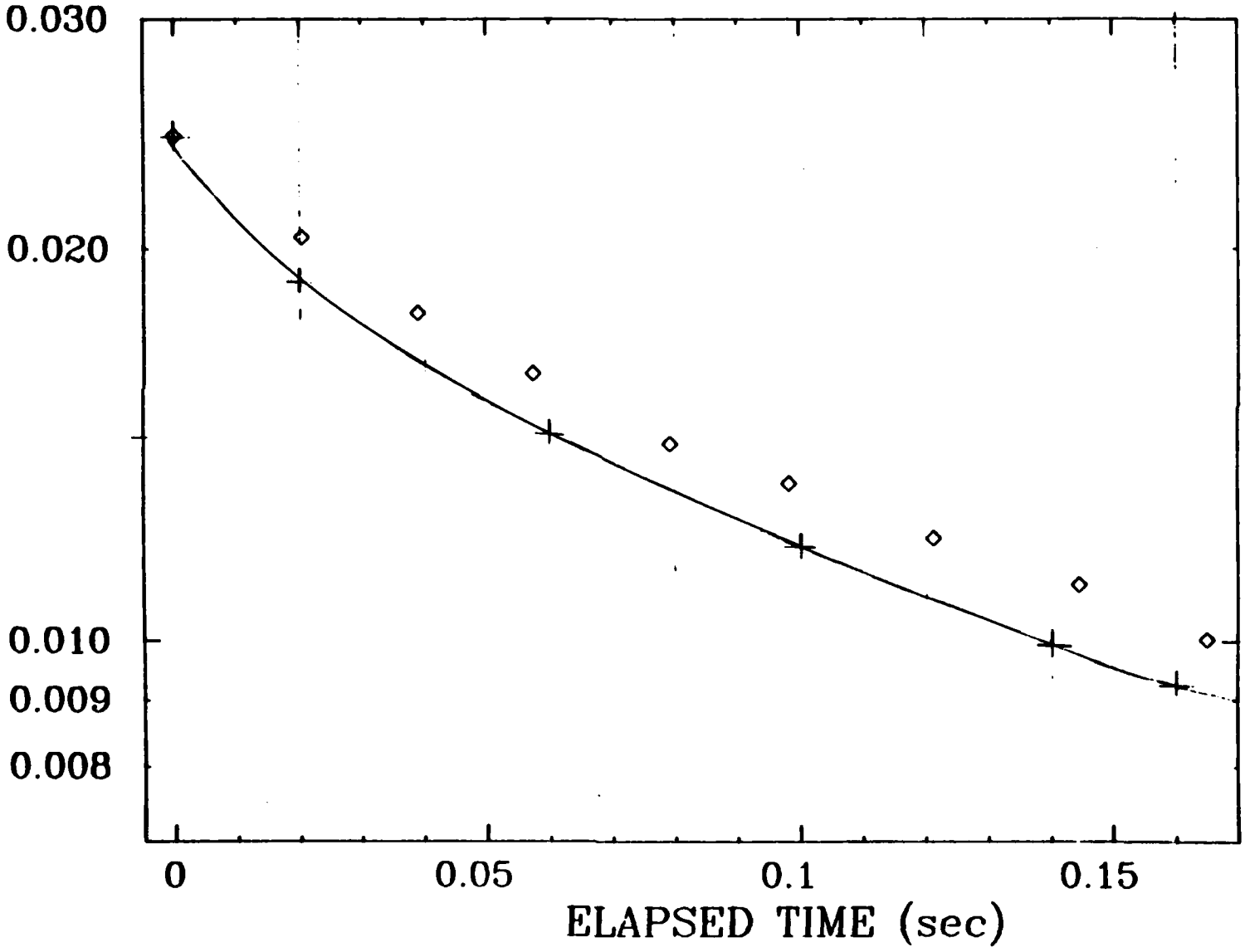

Figure 55. Case 0374A (Plane strain) Longitudinal correlation.

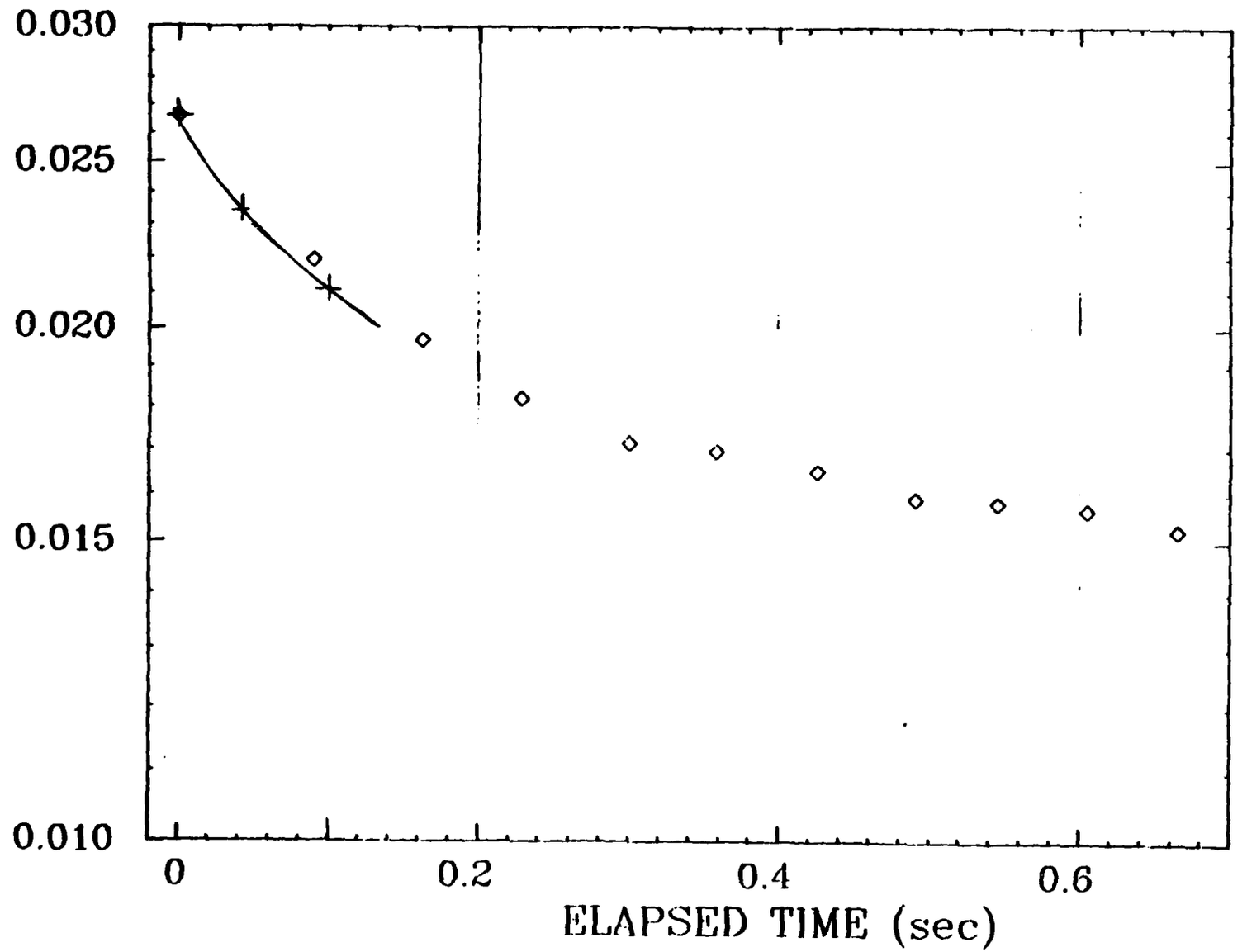

Figure 56. Case 0374A (Plane strain) Transverse correlation.

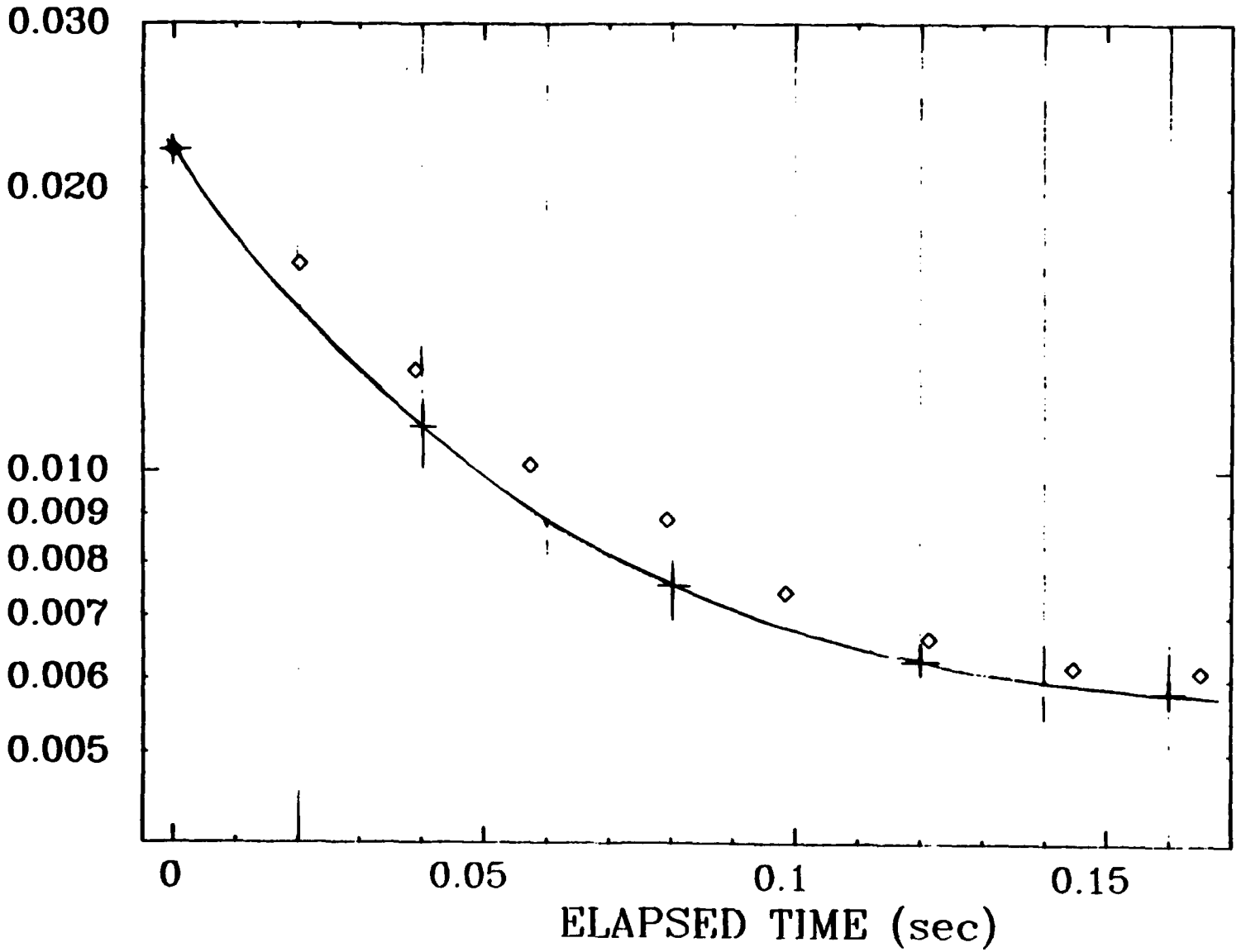

Figure 57. Case 0374A (Plane strain) Transverse correlation.

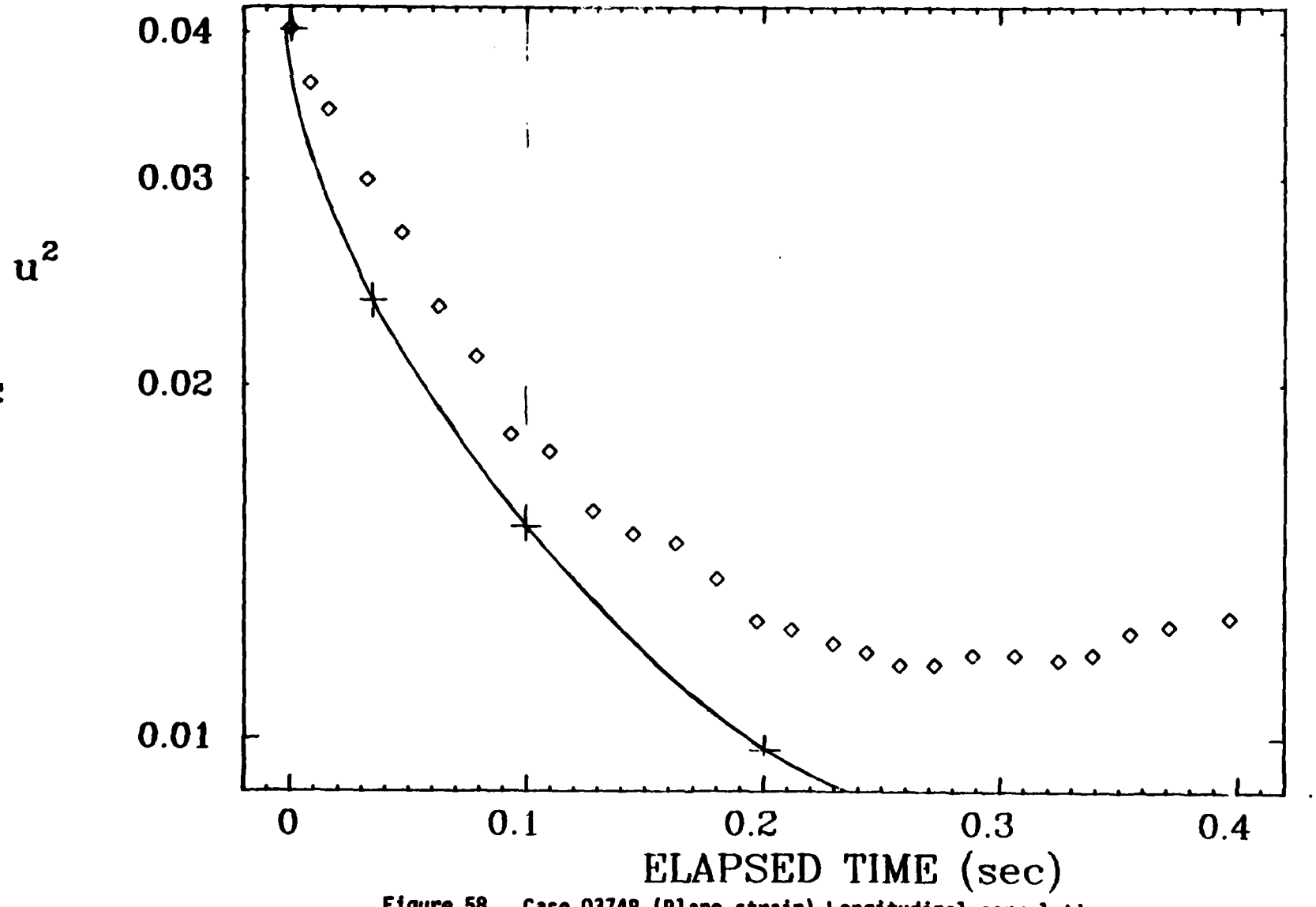

Figure 58. Case 0374B (Plane strain) Longitudinal correlation.

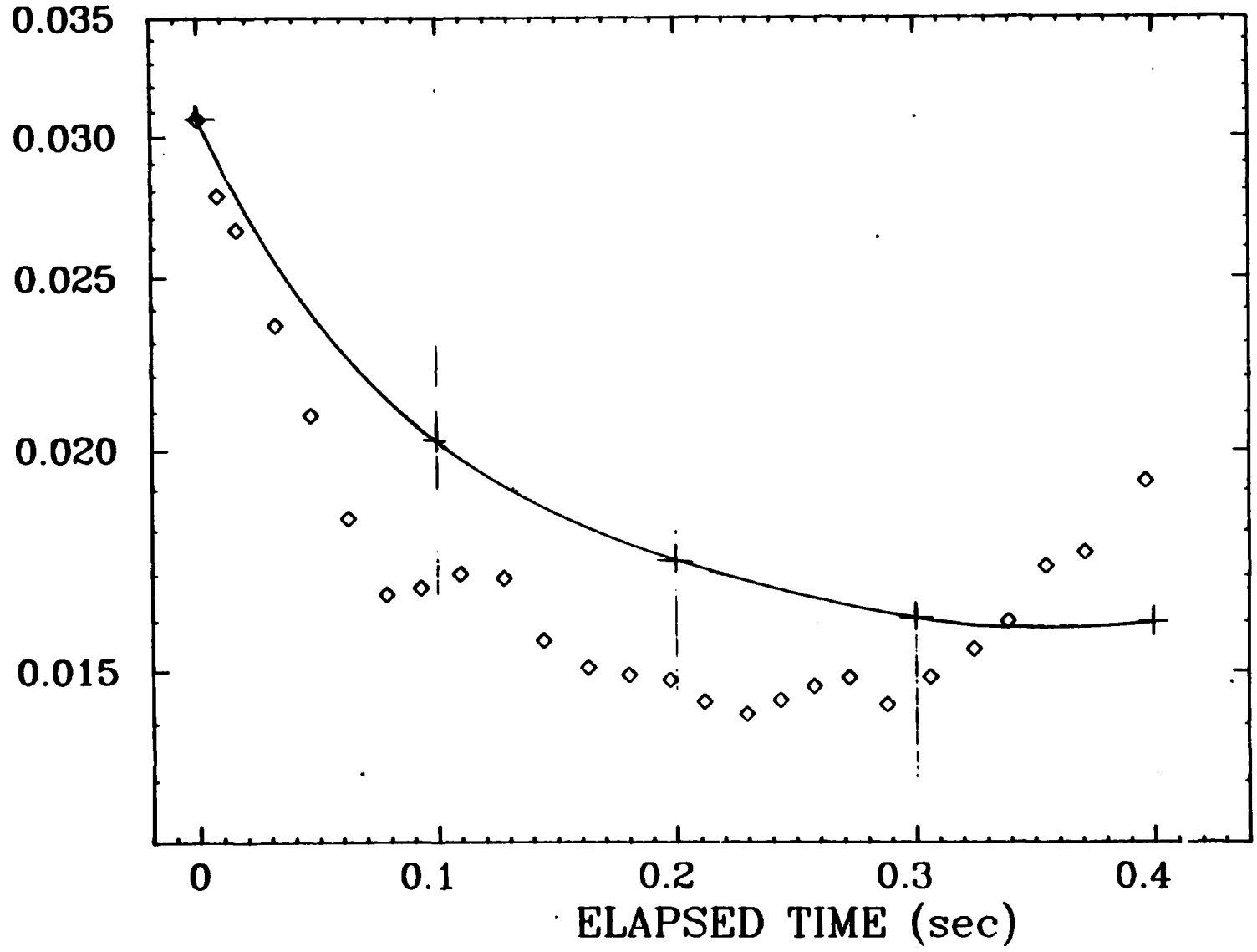

Figure 59. Case 0374B (Plane strain) Transverse correlation.

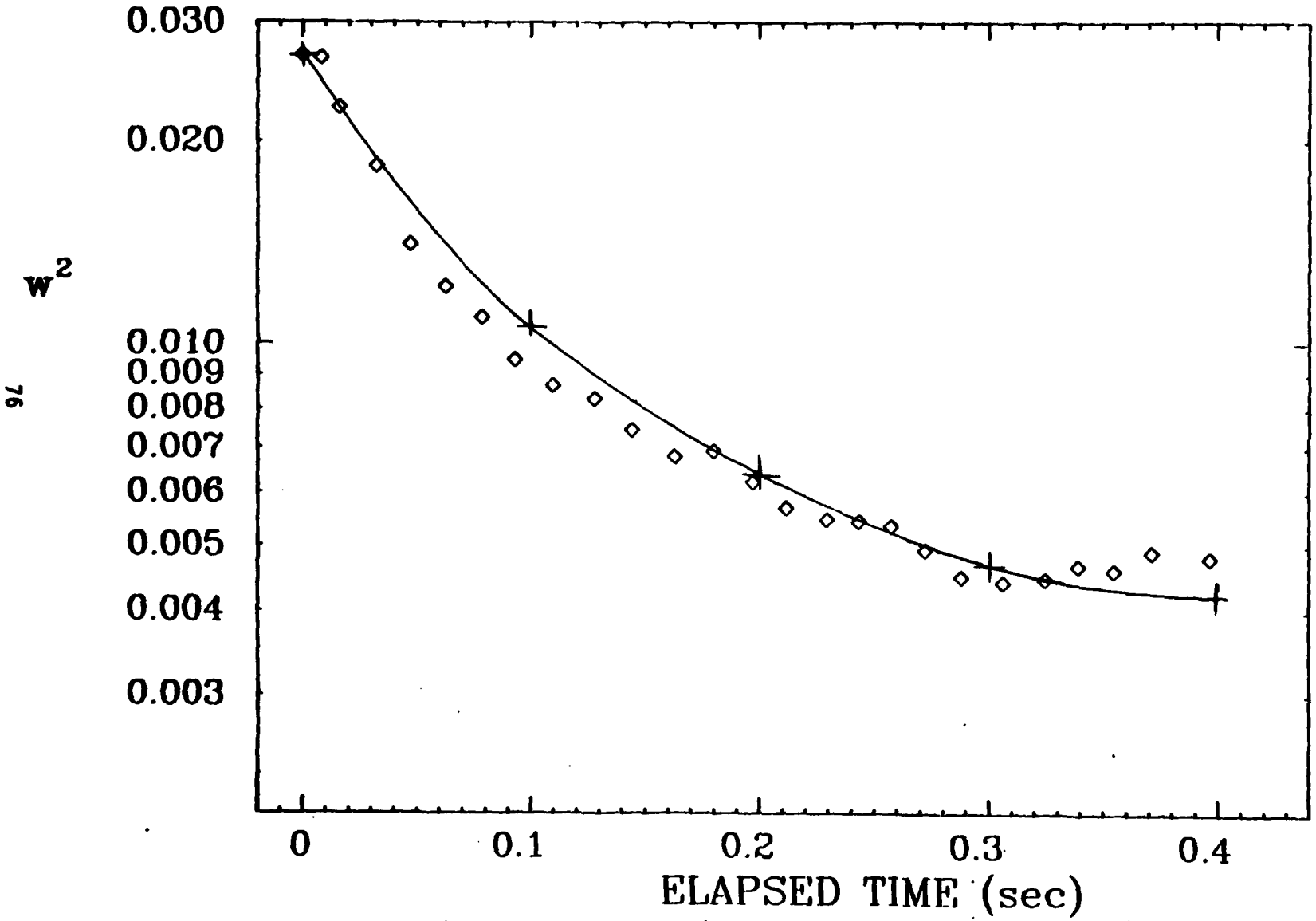

Figure 60. Case 0374B (Plane strain) Transverse correlation.

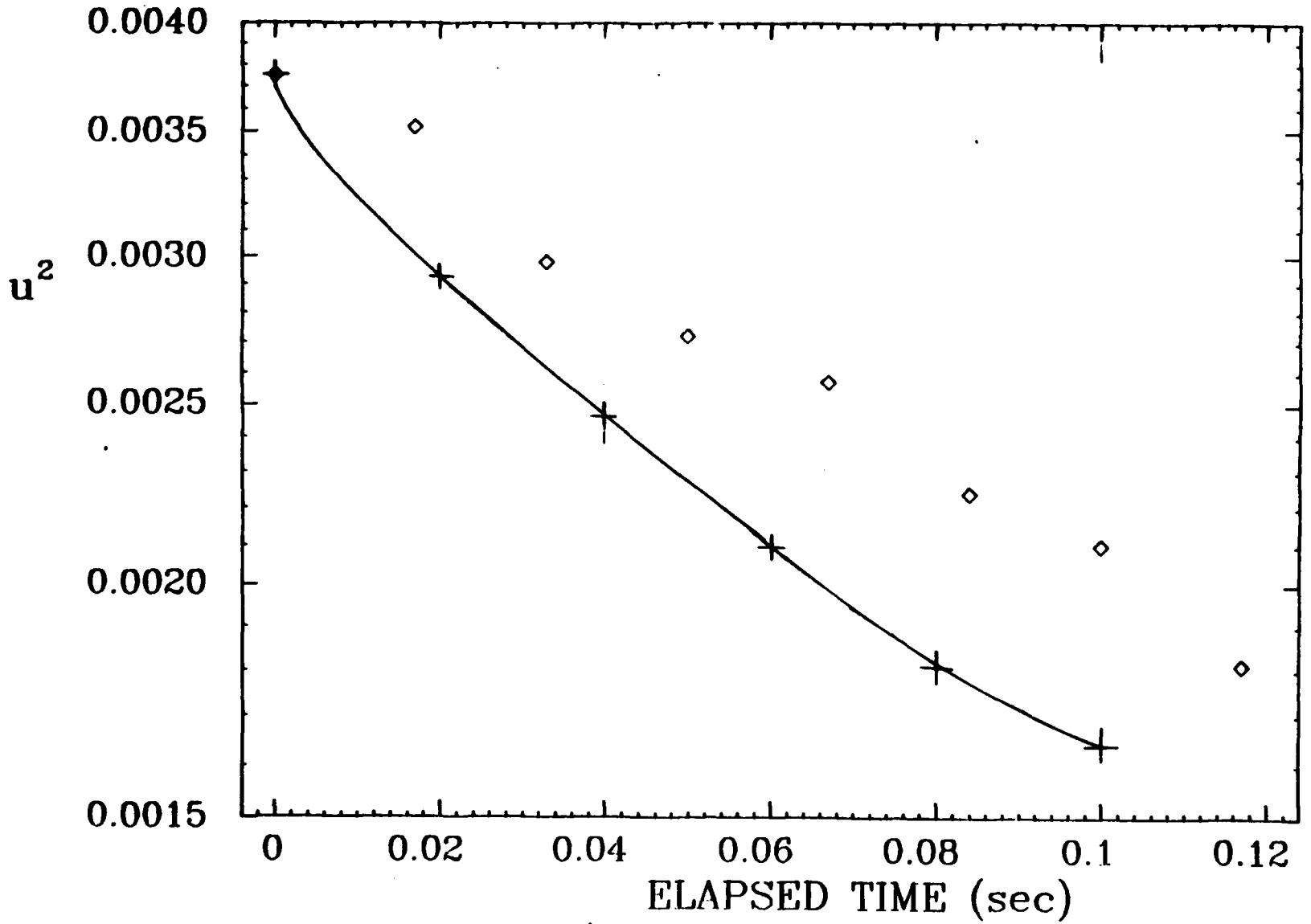

Figure 61. Case 0375A (Axisymmetric strain) Longitudinal correlation.

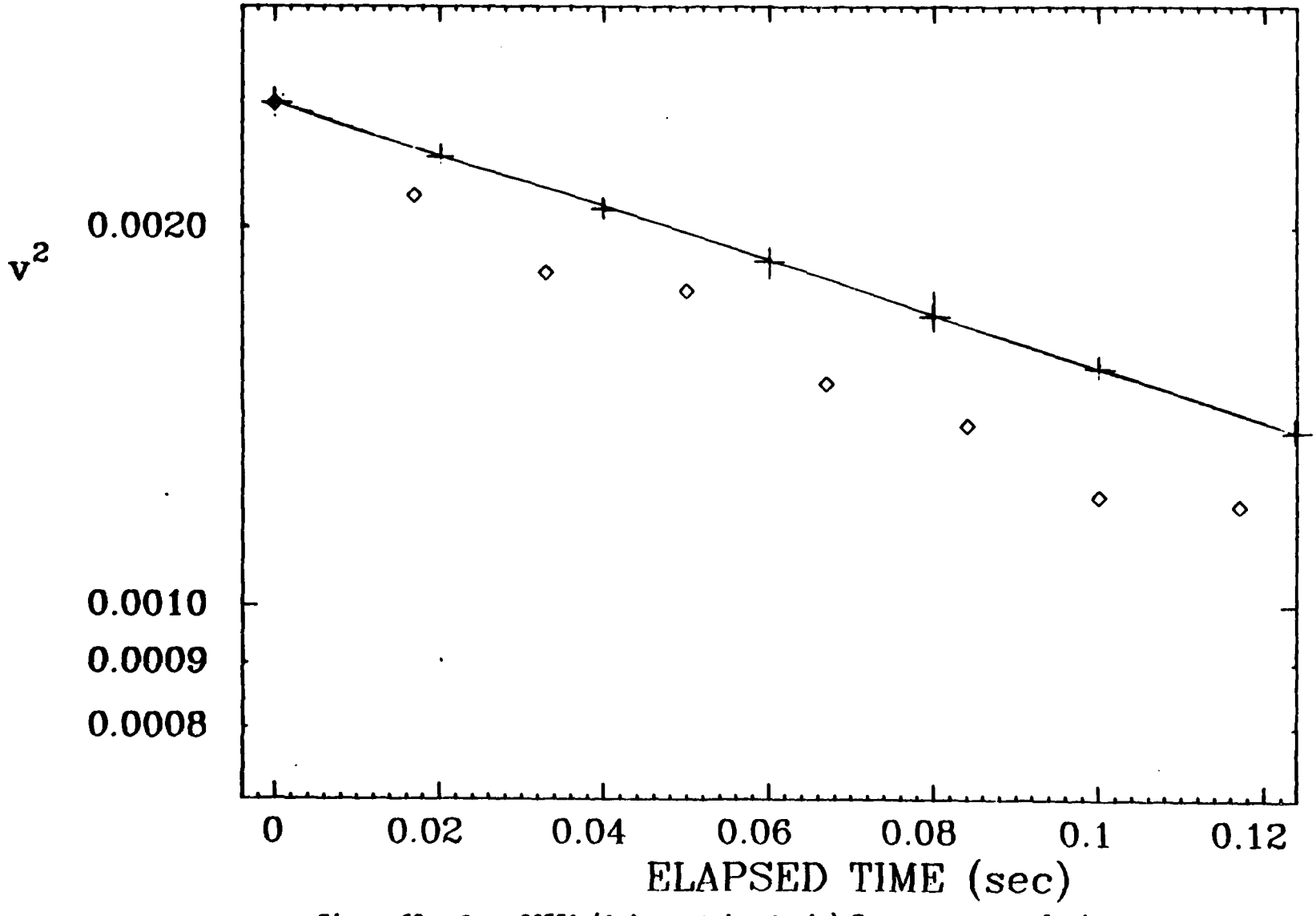

Figure 62. Case 0375A (Axisymmetric strain) Transverse correlation.

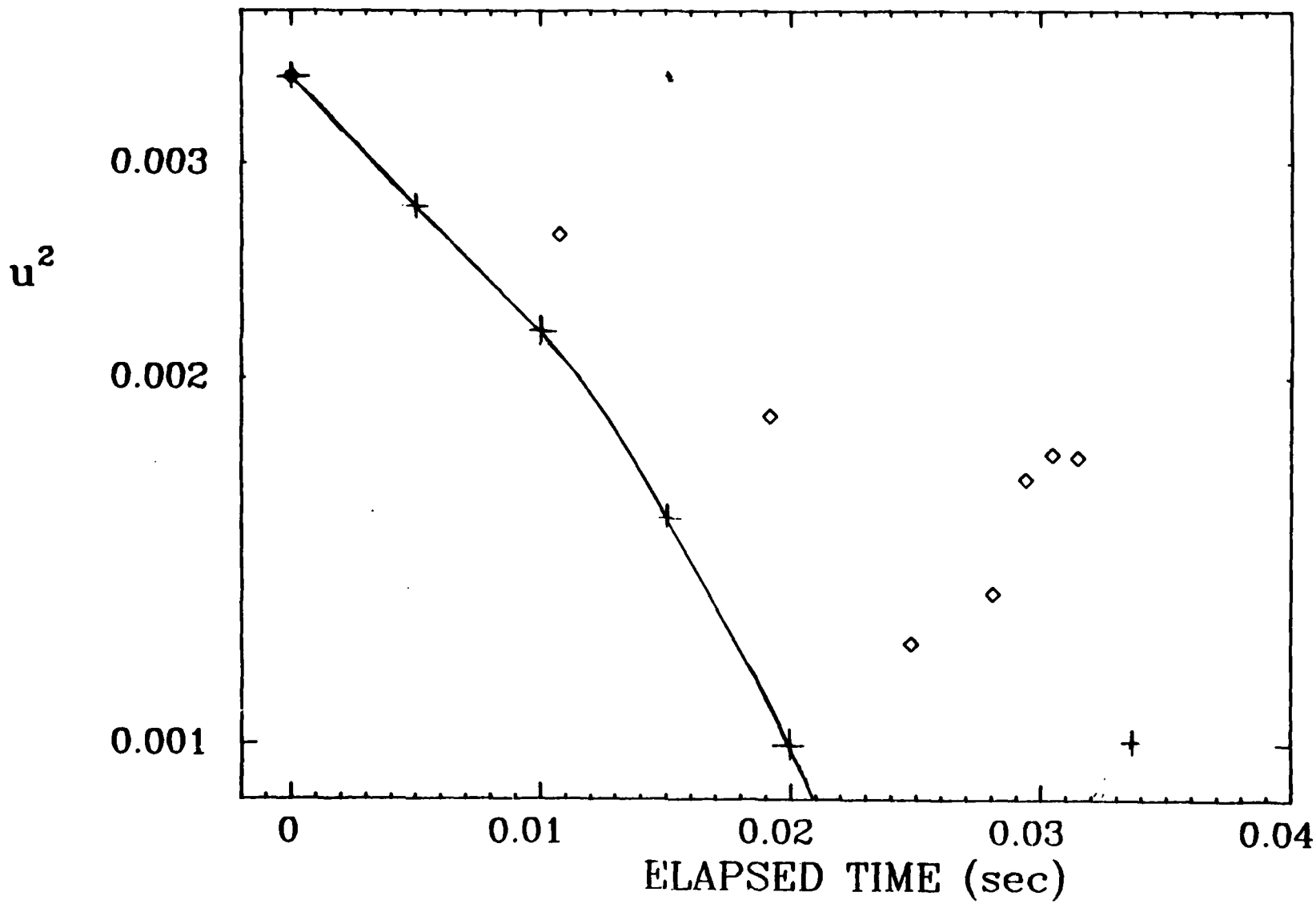

Figure 63. Case 0375B (Axisymmetric strain) Longitudinal correlation.

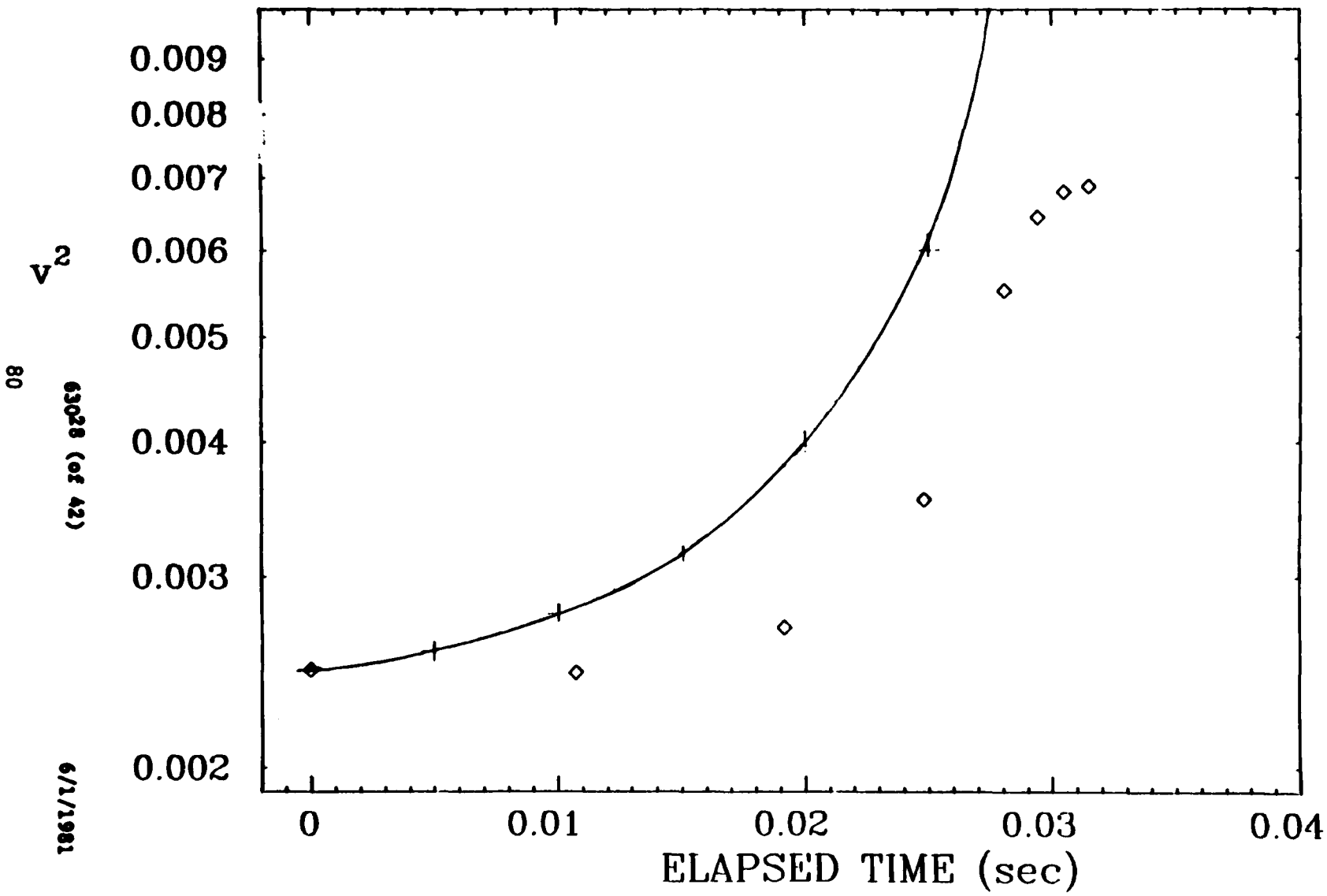

Figure 64. Case 0375B (Axisymmetric strain) Transverse correlation.

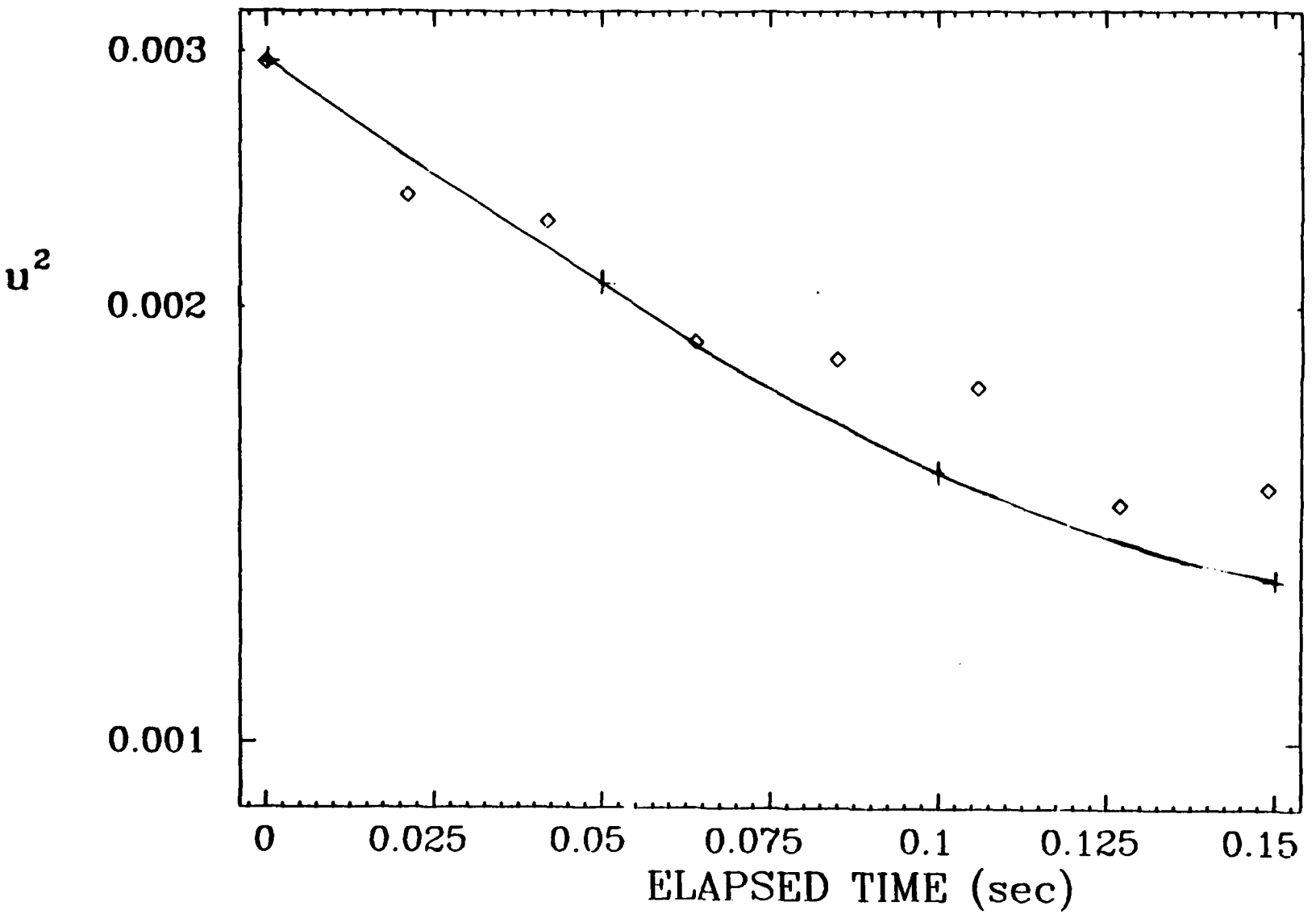

Figure 65. Case 0375C (Axisymmetric strain) Longitudinal correlation.

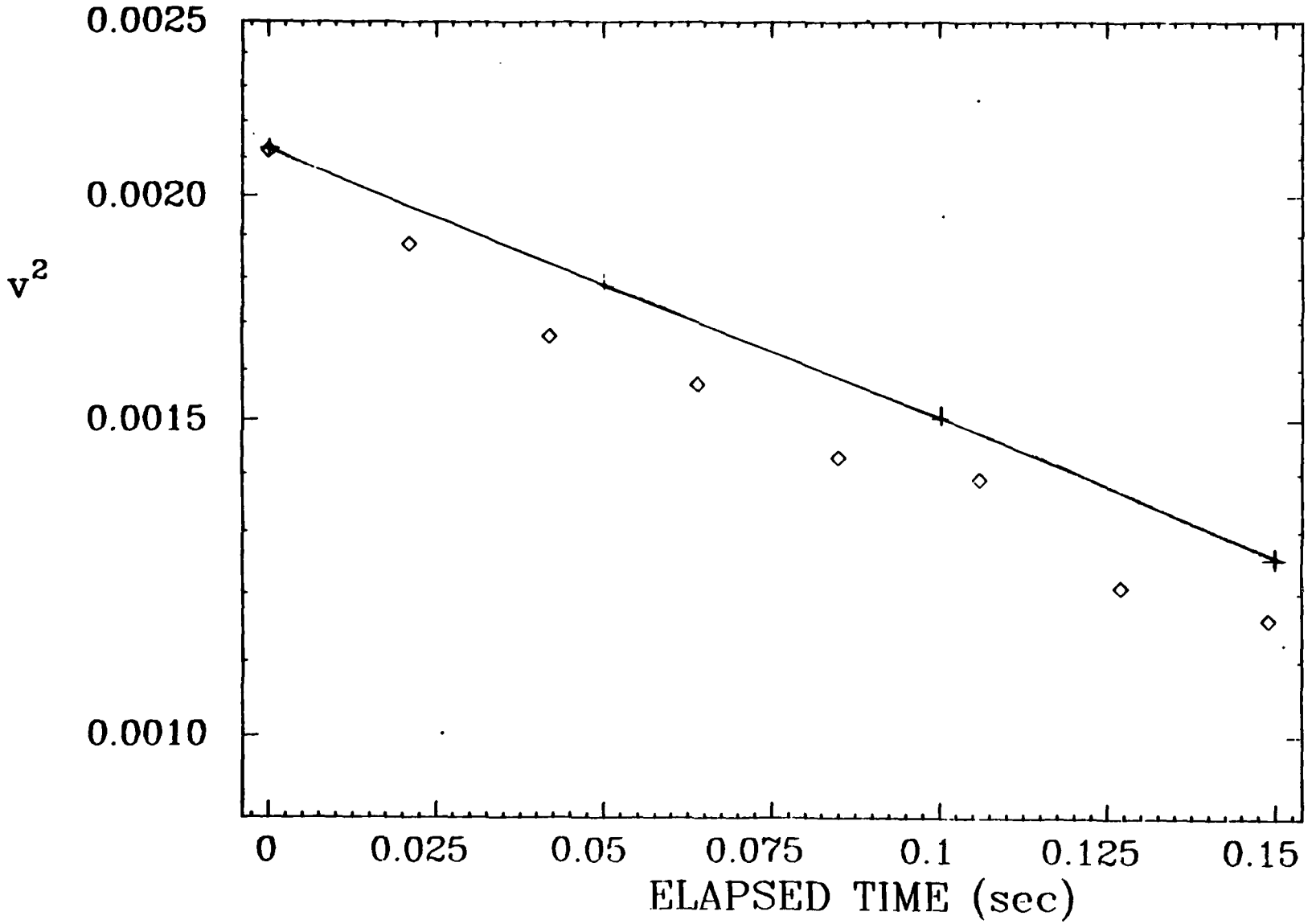

Figure 66. Case 0375C (Axisymmetric strain) Transverse correlation.

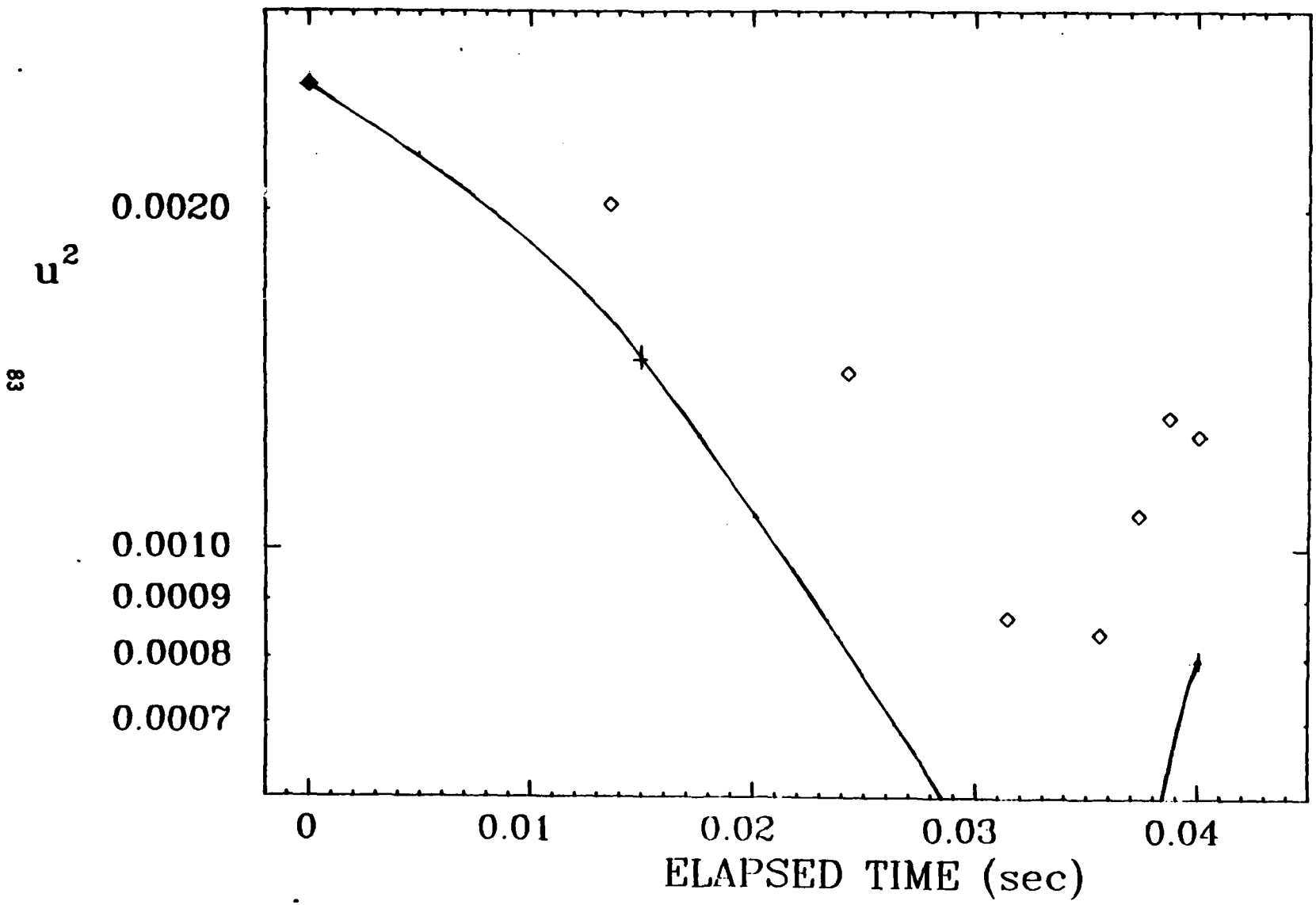

Figure 67. Case 0375D (Axisymmetric strain) Longitudinal correlation.

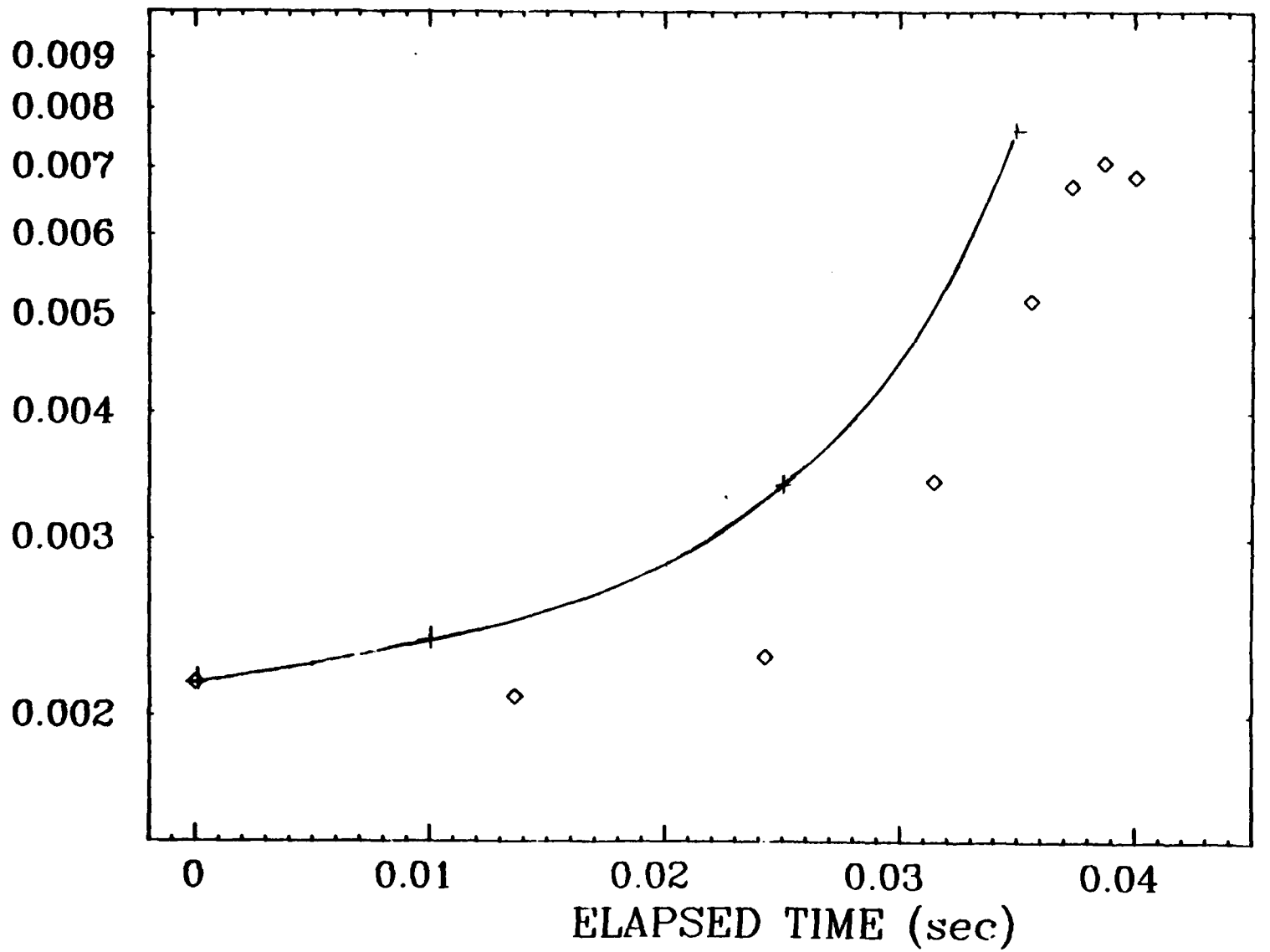

Figure 68. Case 0375D (Axisymmetric strain) Transverse correlation.

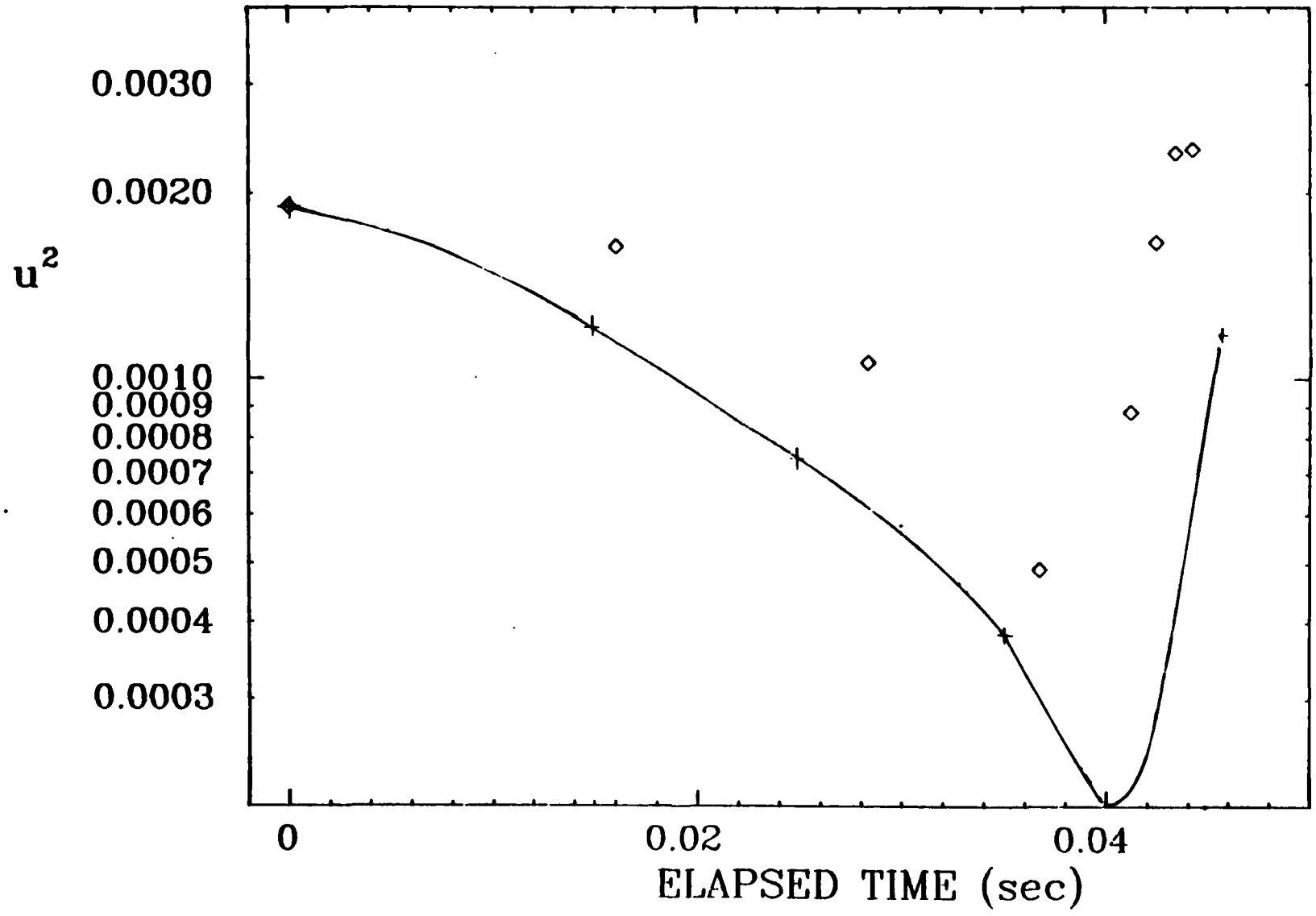

Figure 69. Case 0375E (Axisymmetric strain) Longitudinal correlation.

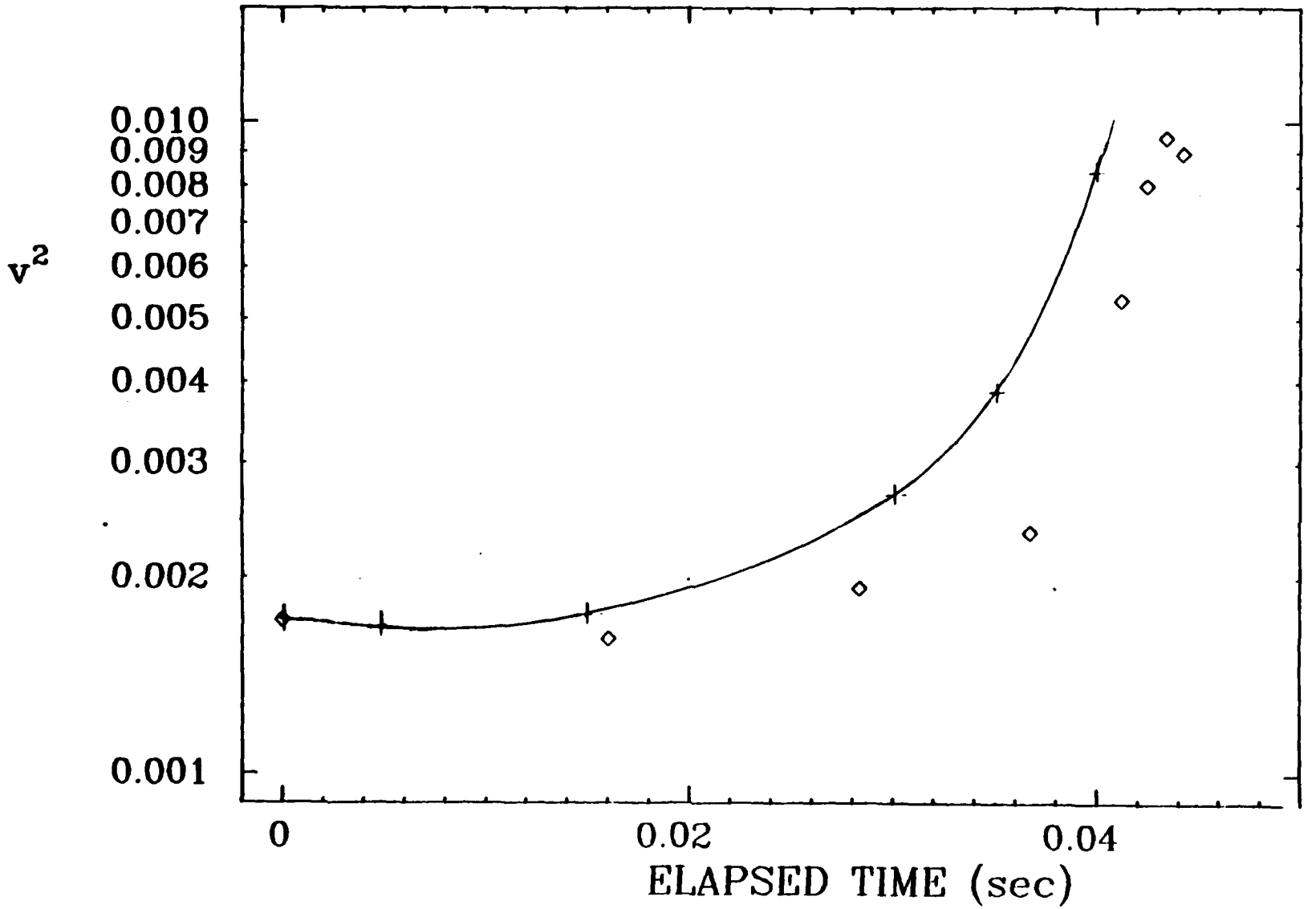

Figure 70. Case 0375E (Axisymmetric strain) Transverse correlation.

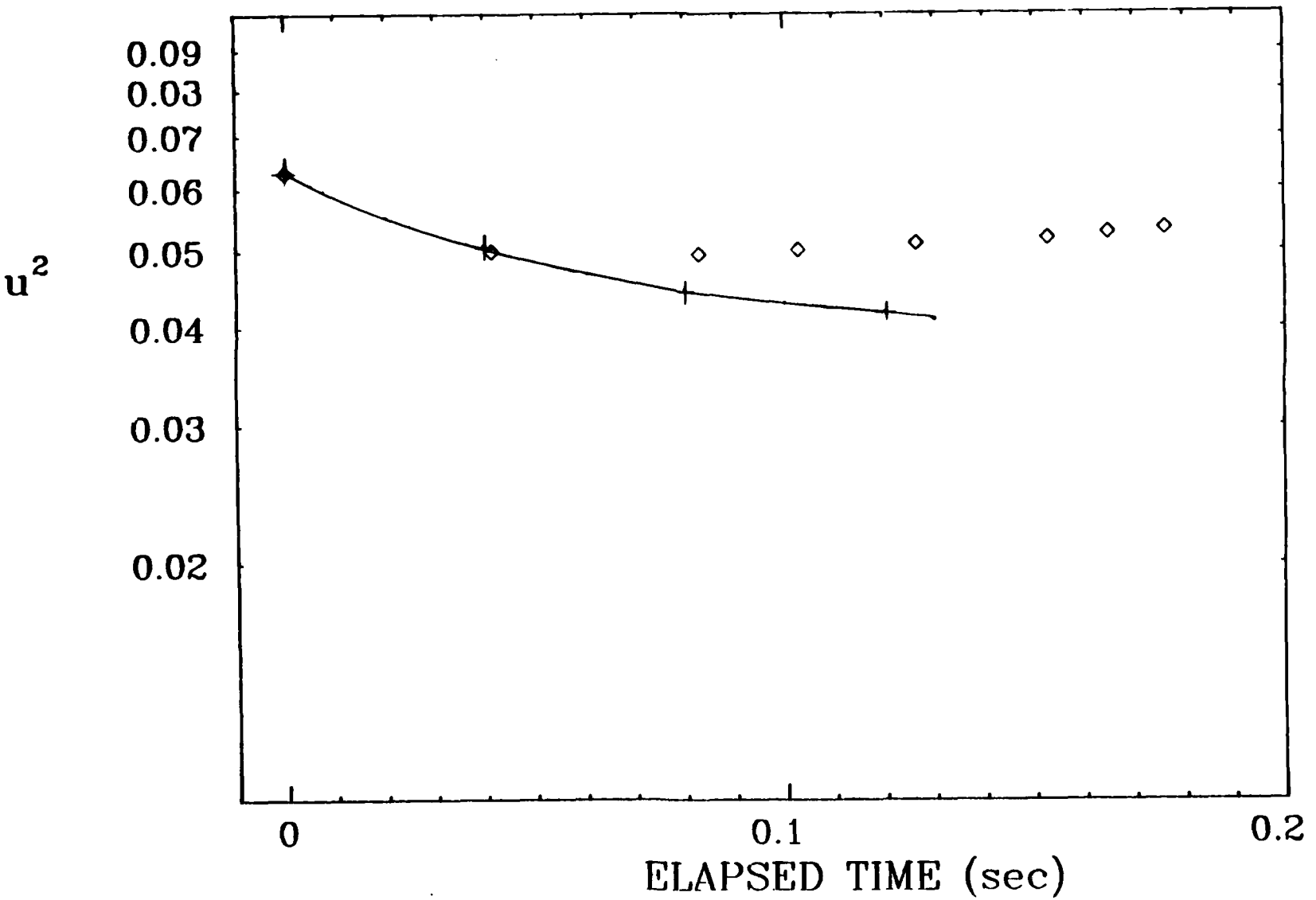

Figure 71. Case 0376A (Low-strain shear) Longitudinal correlation.

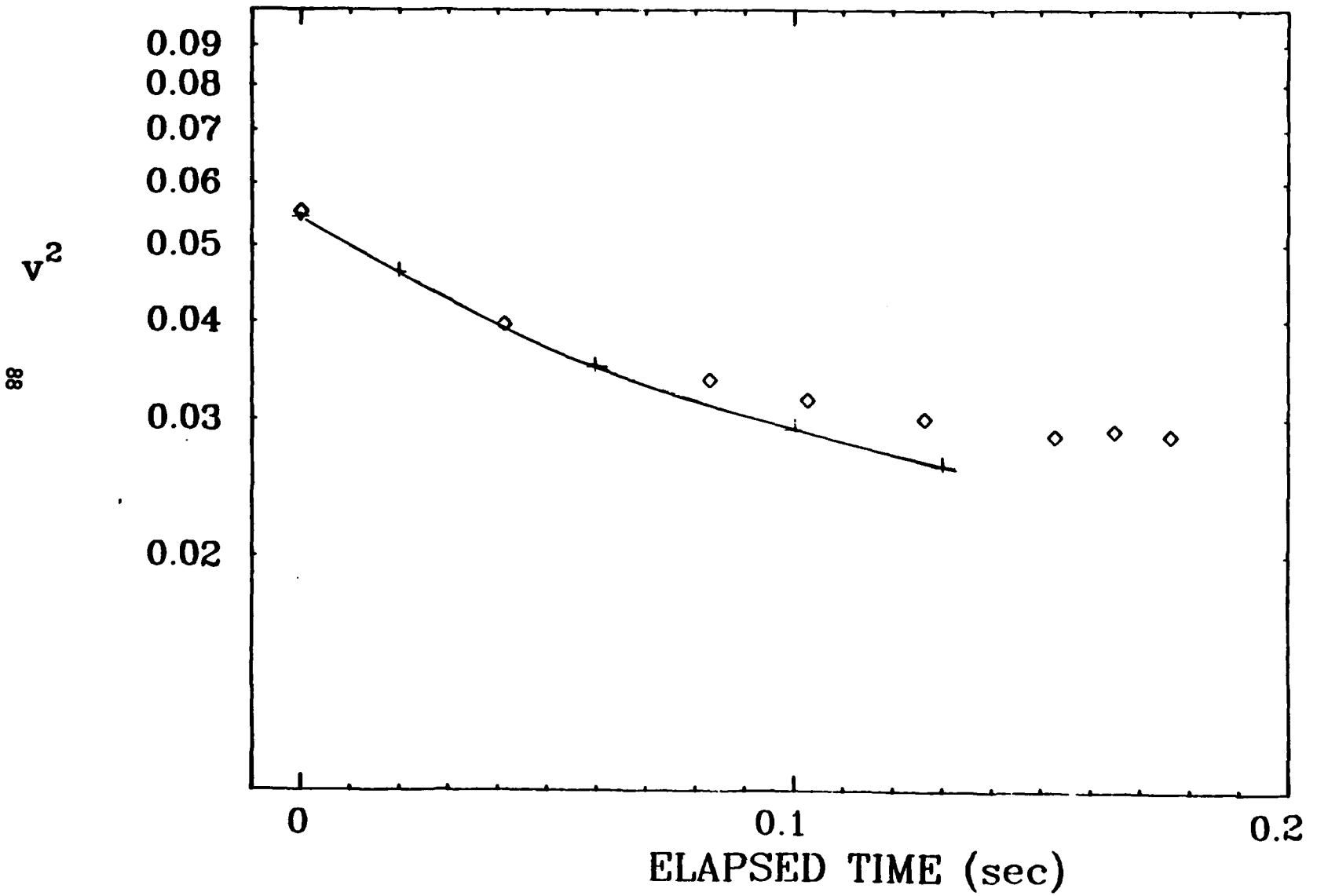

Figure 72. Case 0376A (Low-strain shear) Transverse correlation.

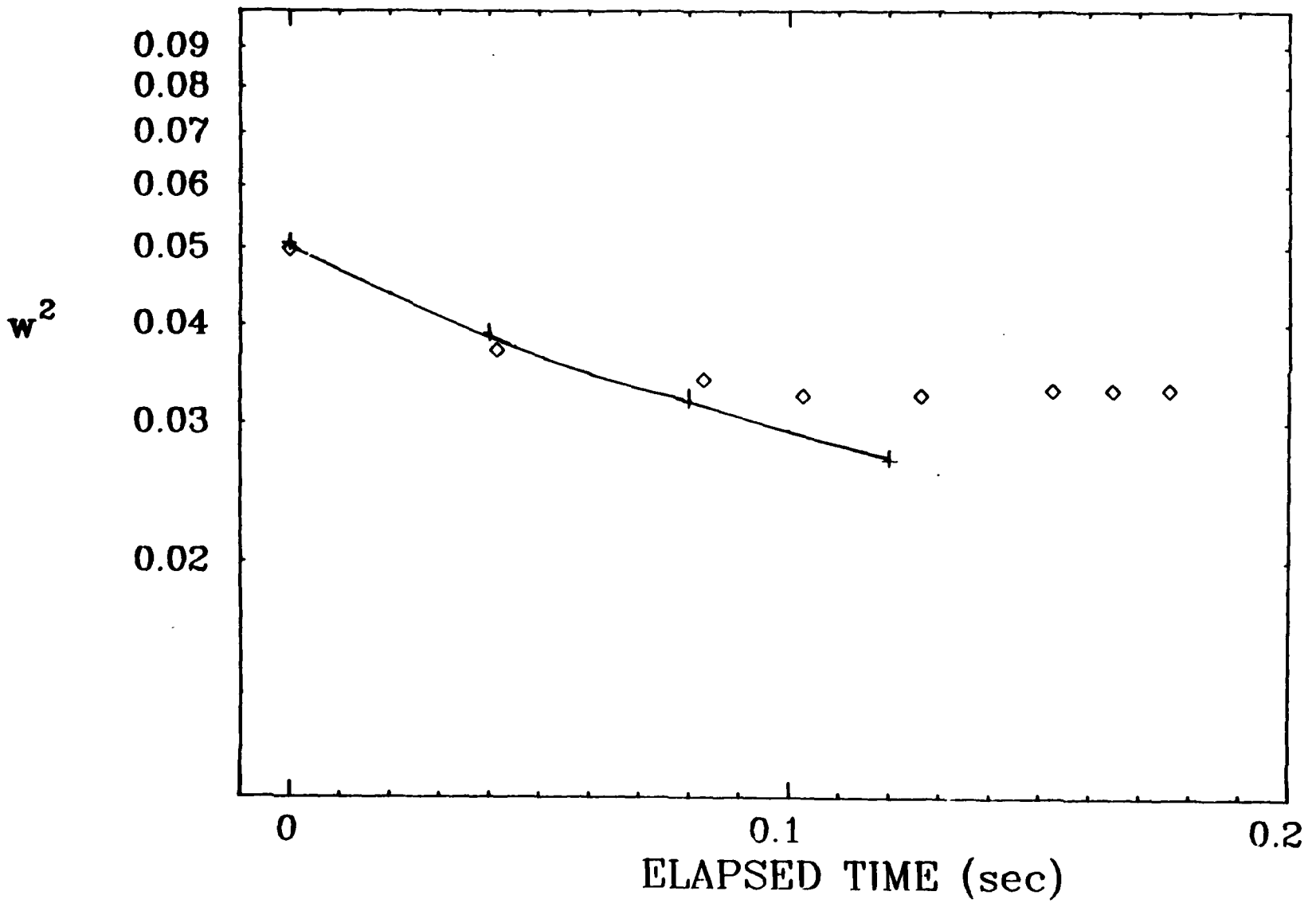

Figure 73. Case 0376A (Low-strain shear) Transverse correlation.

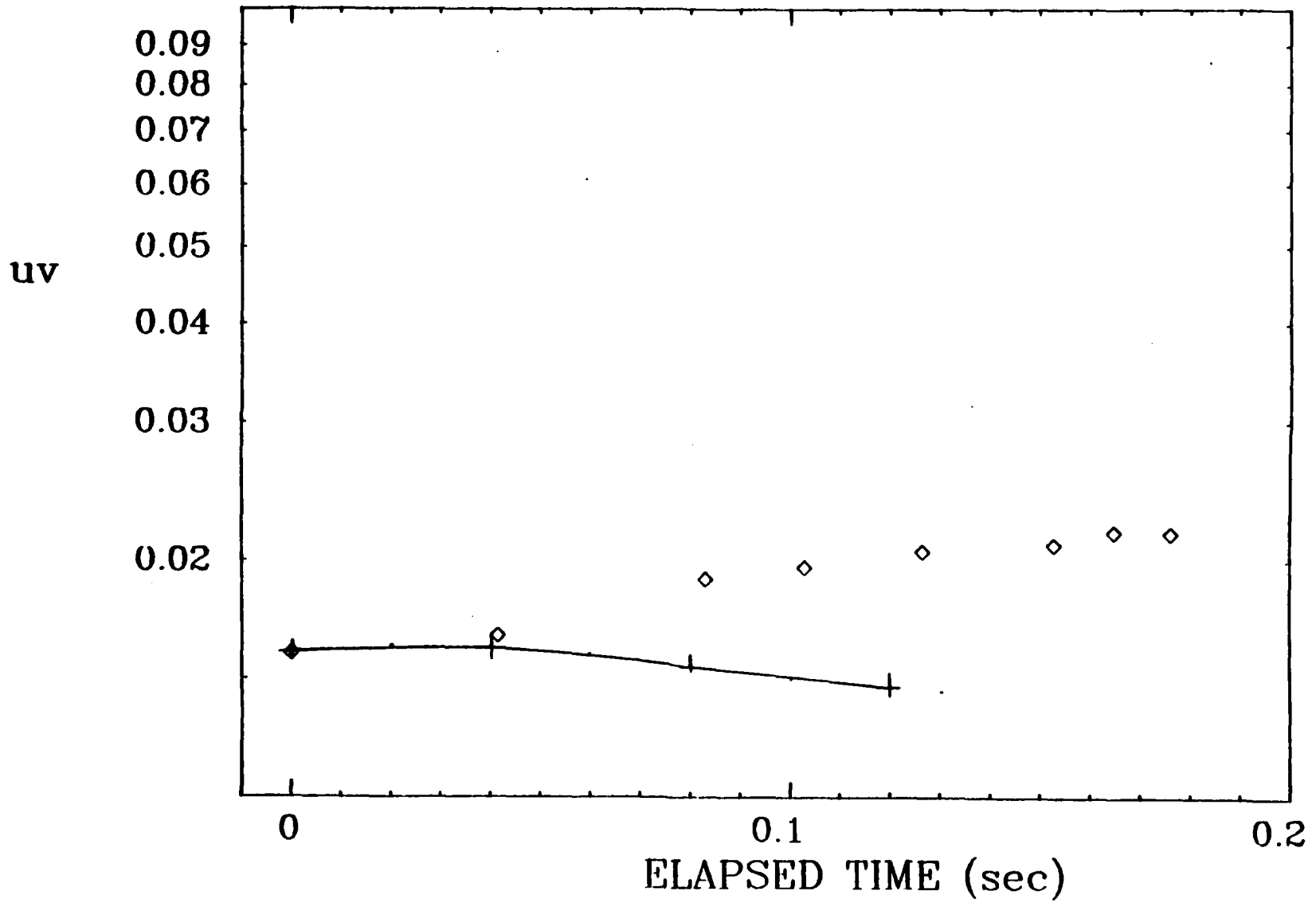

Figure 74. Case 0376A (Low-strain shear) Cross correlation.

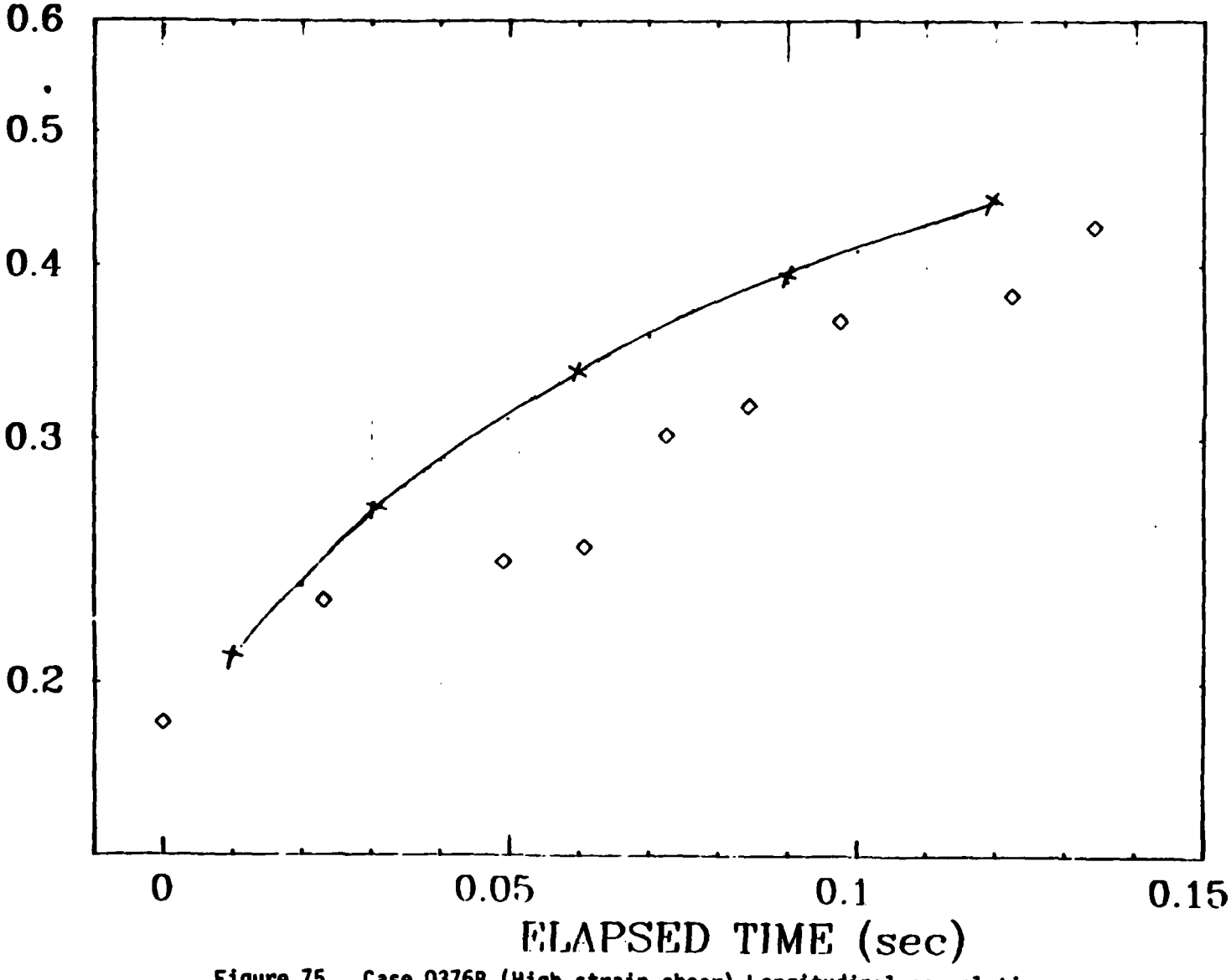

Figure 75. Case 0376B (High-strain shear) Longitudinal correlation.

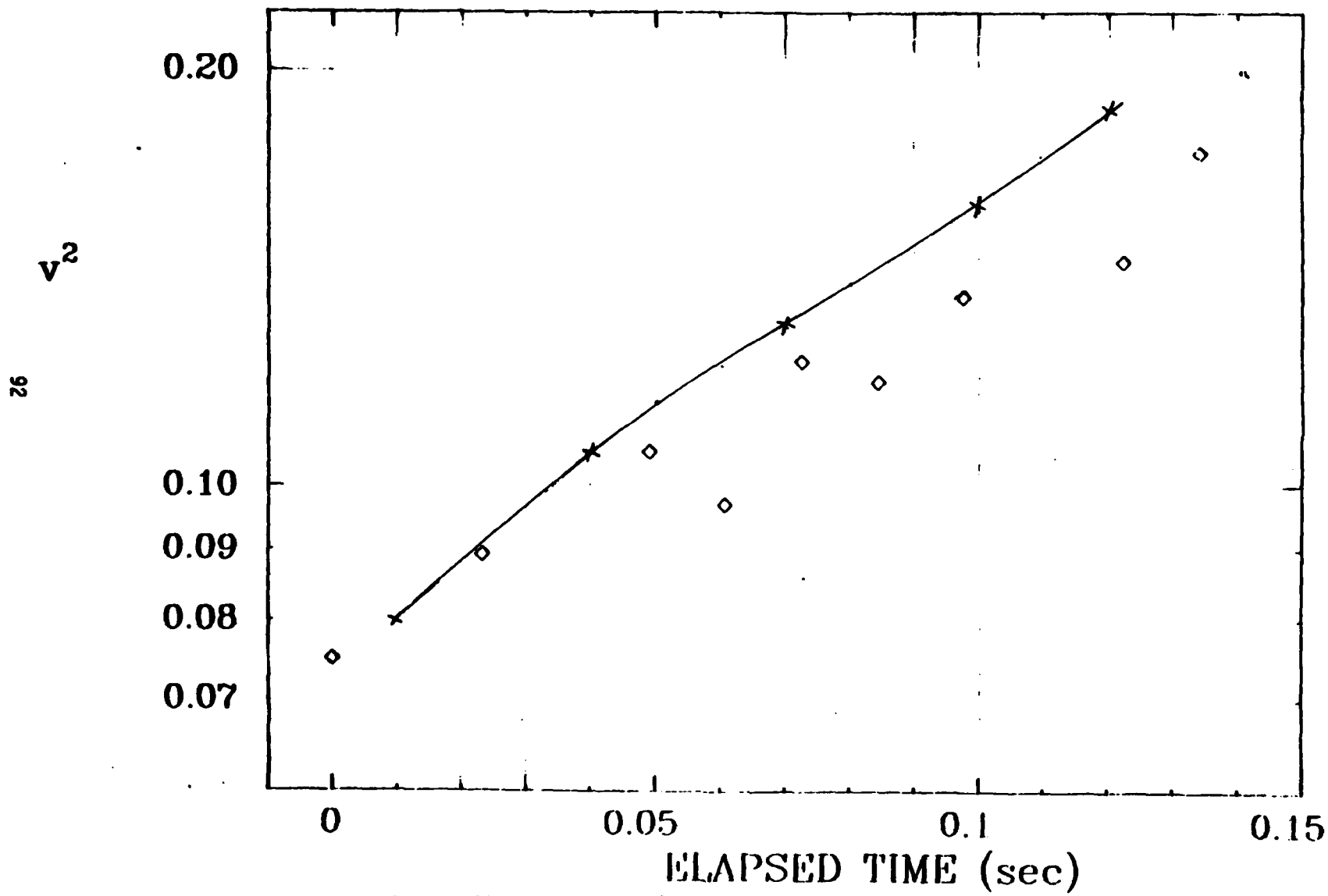

Figure 76. Case 0376B (High-strain shear) Transverse correlation.

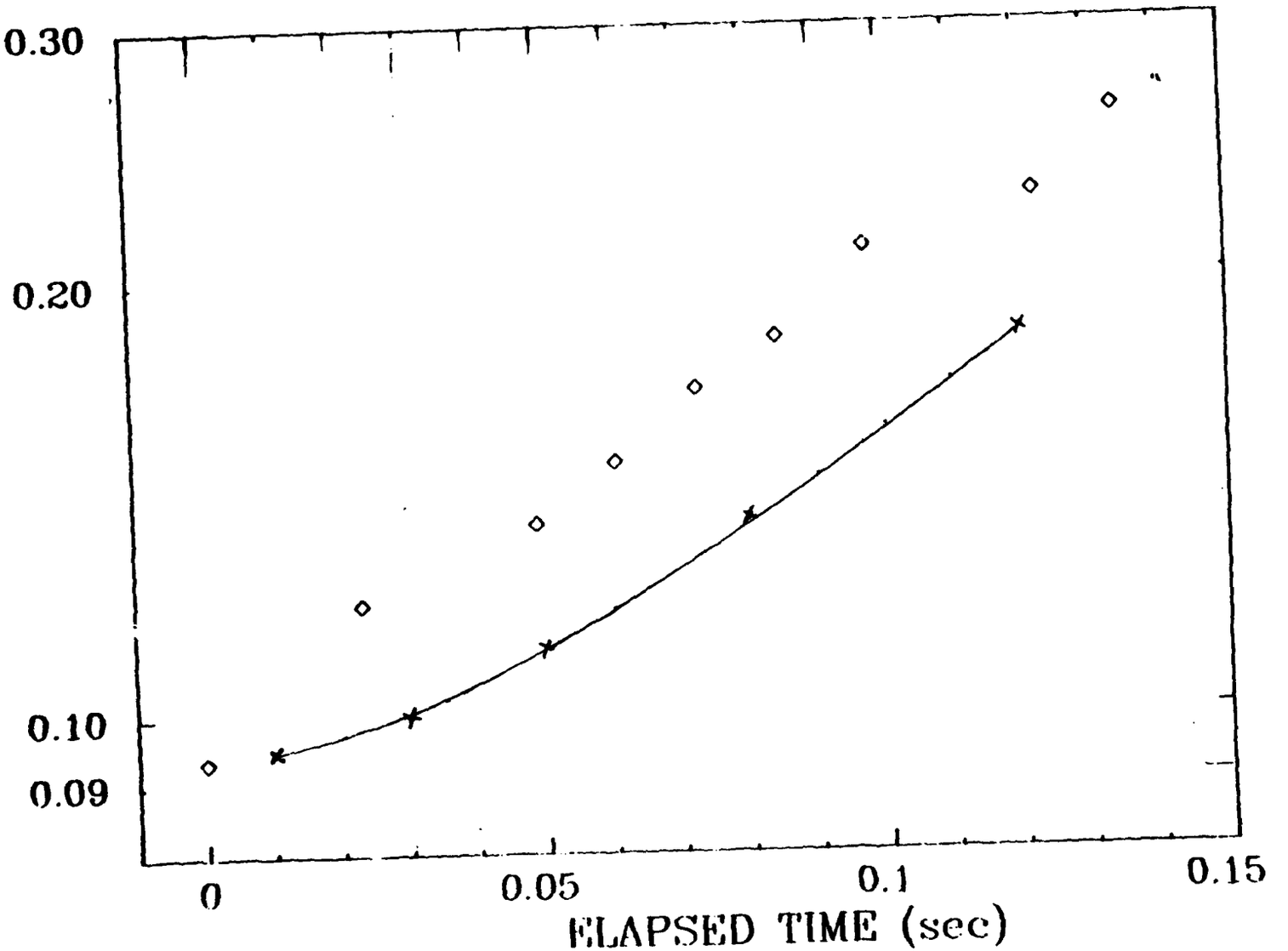

Figure 77. Case 0376B (High-strain shear) Transverse correlation.

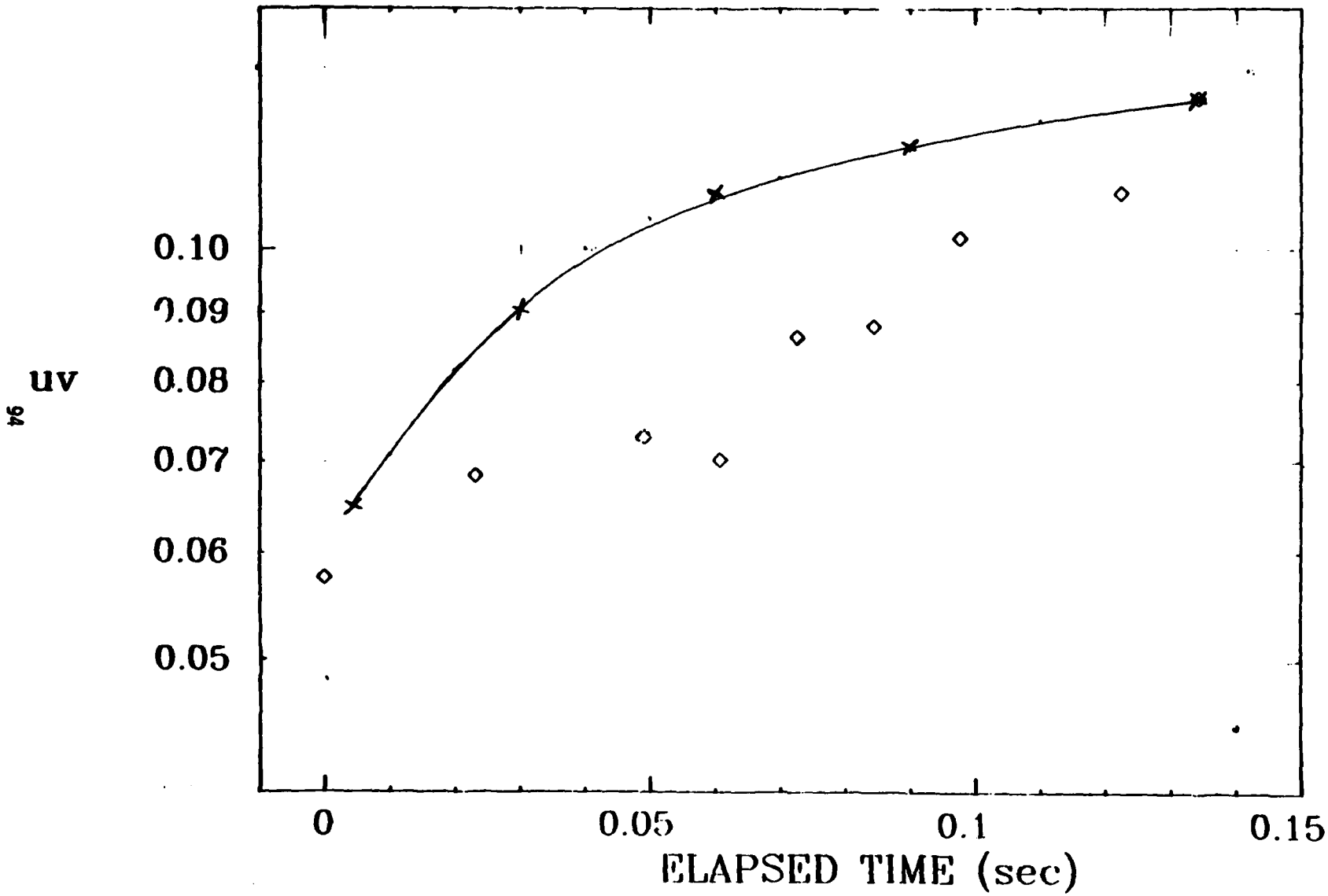

Figure 78. Case 0376B (High-strain shear) Cross correlation.

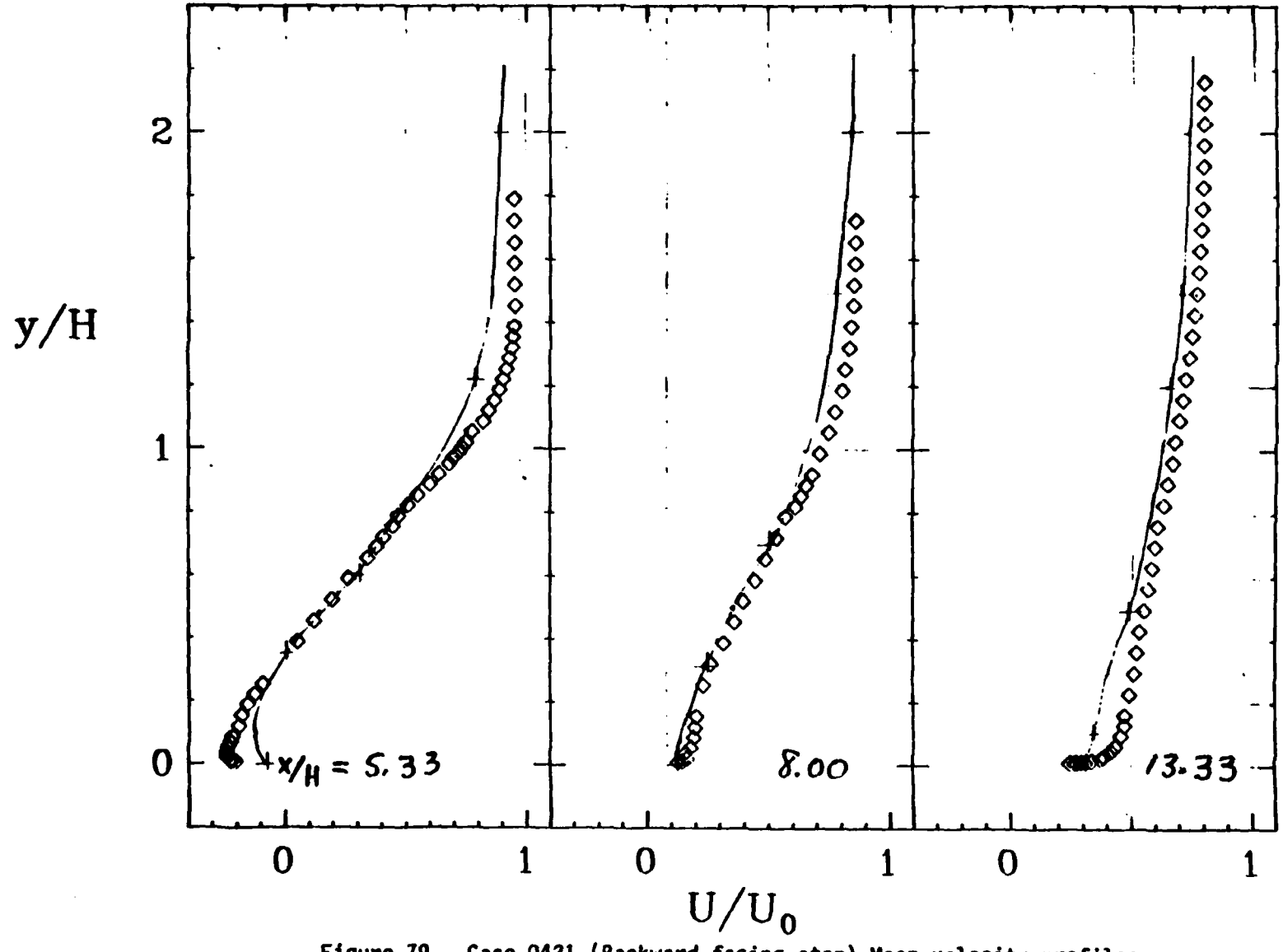

Figure 79. Case 0421 (Backward-facing step) Mean velocity profiles.

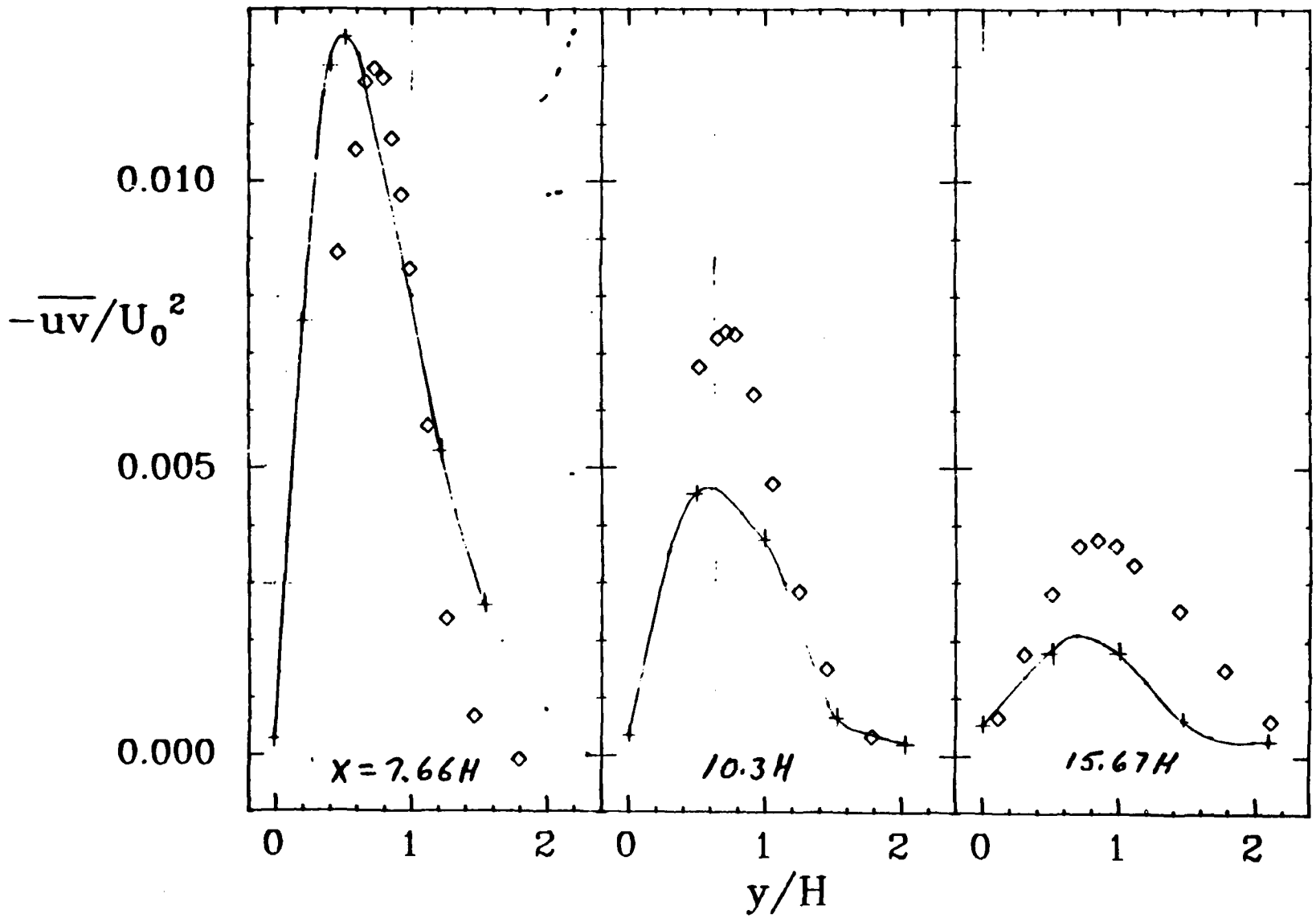

Figure 80. Case 0421 (Backward-facing step) Turbulent stress profiles.

AD-A121 322 ARAP'S SECOND-ORDER CLOSURE MODEL: COMPARISON WITH A NUMBER OF COMPLEX TU..(U) AERONAUTICAL RESEARCH ASSOCIATES OF PRINCETON INC NJ W S KEWELLEN ET AL.

UNCLASSIFIED APR 82 ARAP-469 AFOSR-TR-82-0970 F/G 20/4 NL

END

DATE FILMED

DTIC

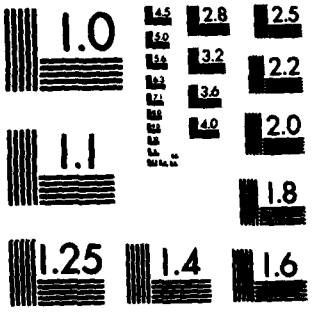

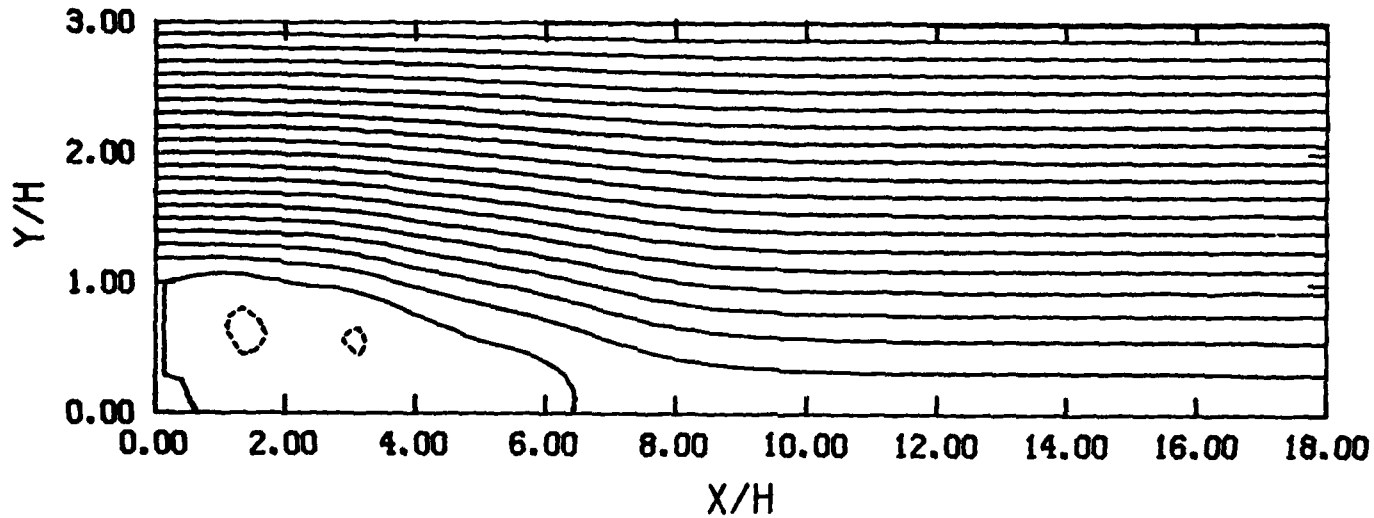

Figure 81. Time-averaged streamlines for Case 0421, behind the backward facing step. H is the height of the step. Contours shown at equally spaced intervals.

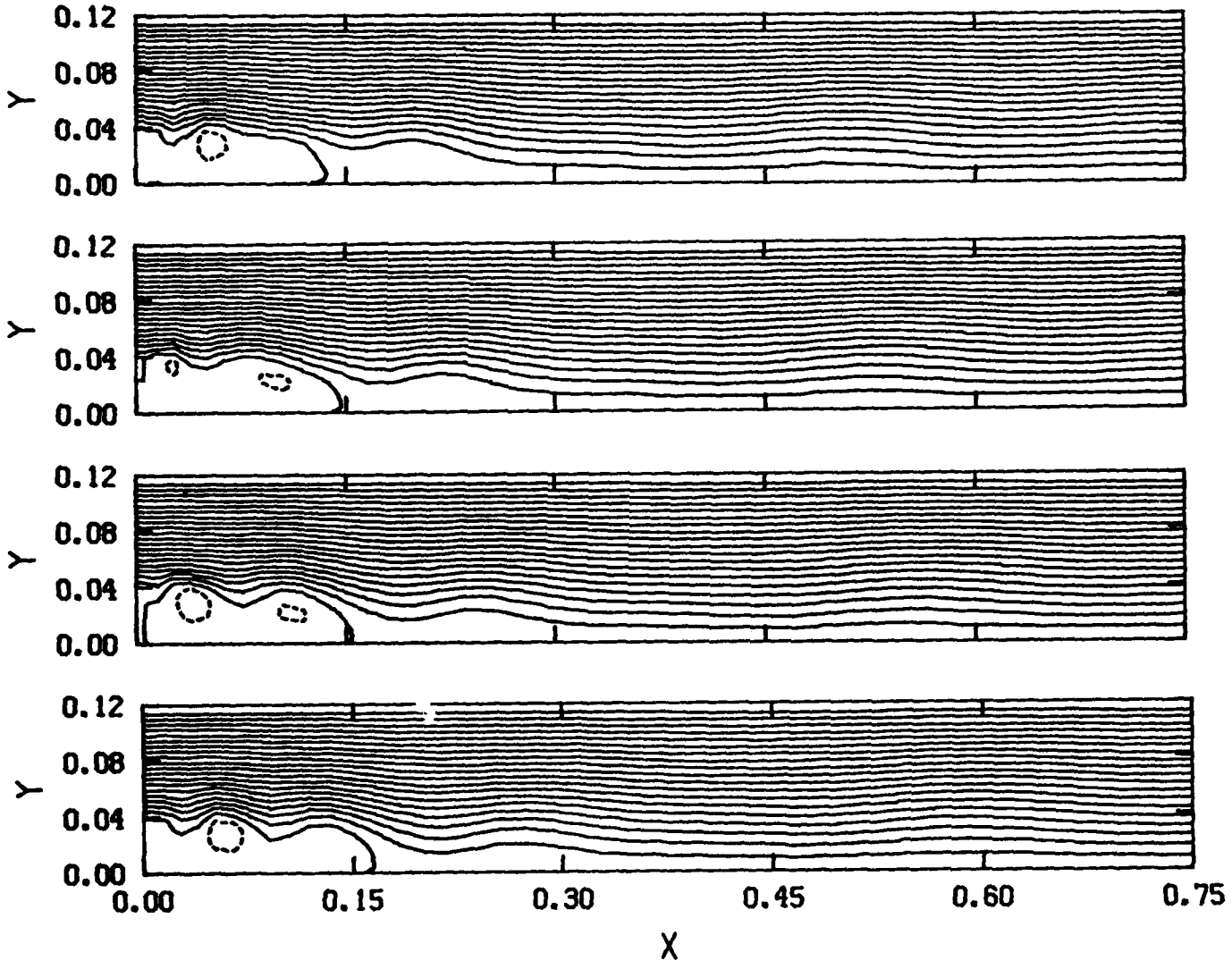

Figure 82 (a-d). Unsteady streamline pattern behind the backward facing step of Case 0421, shown at several times during approximately one period of oscillation of the separated region. Total time duration of approximately 0.02 seconds. a. (top) T = .357, b. T = .360, c. T = 363, d. (bottom) T = .366.

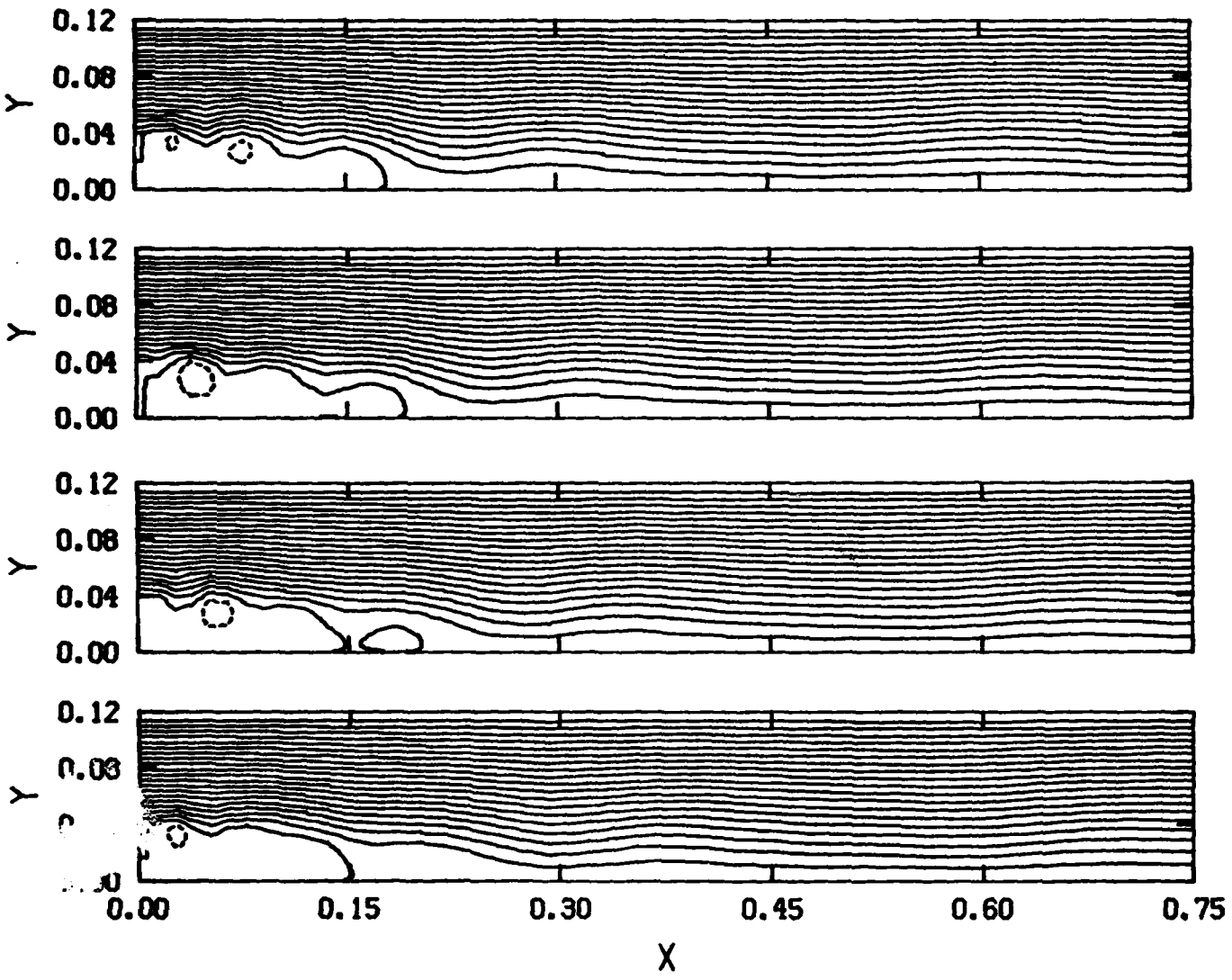

Figure 82 (e-h). Unsteady streamline pattern behind the backward facing step of Case 0421, shown at several times during approximately one period of oscillation of the separated region. Total time duration of approximately 0.02 seconds. e. (top) T = .369, f. T = .372, g. T = .375, h. (bottom) T = .378.

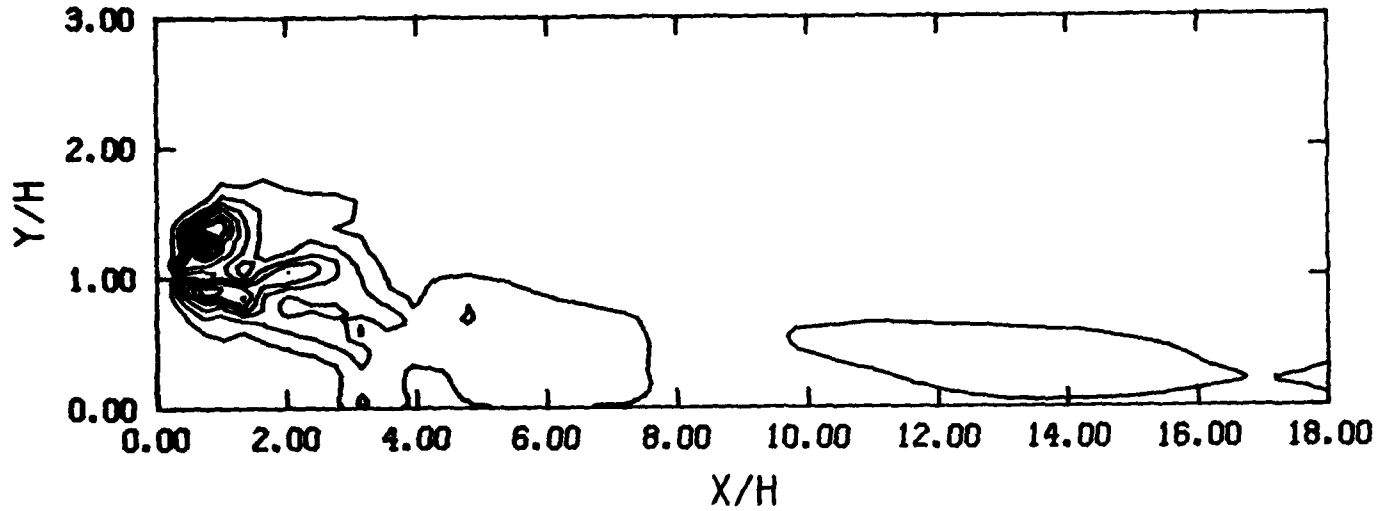

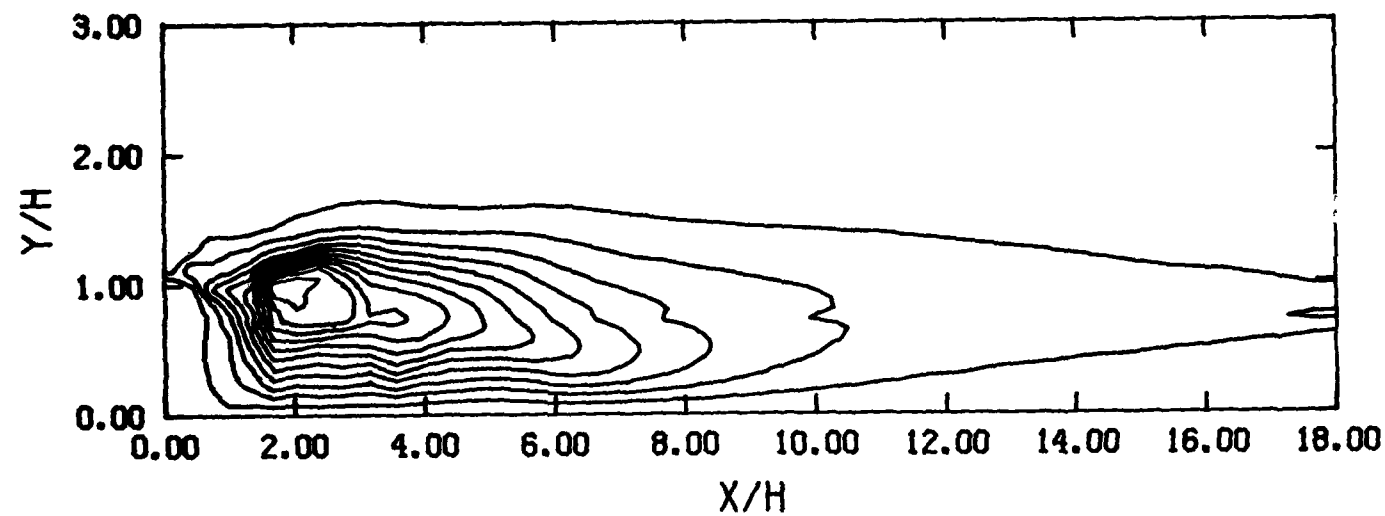

Figure 83. Contours of constant values of longitudinal velocity fluctuations predicted for the flow of Fig. 81. a. Contribution from the 2-D resolved eddies. Contours shown at an interval of 0.006 U_0^2 from 0 to a maximum value of 0.06 U_0^2. b. Contribution from the 3-D modeled turbulence. Contours shown at an interval of 0.004 U_0^2 from 0 to a maximum value of 0.044 U_0^2.

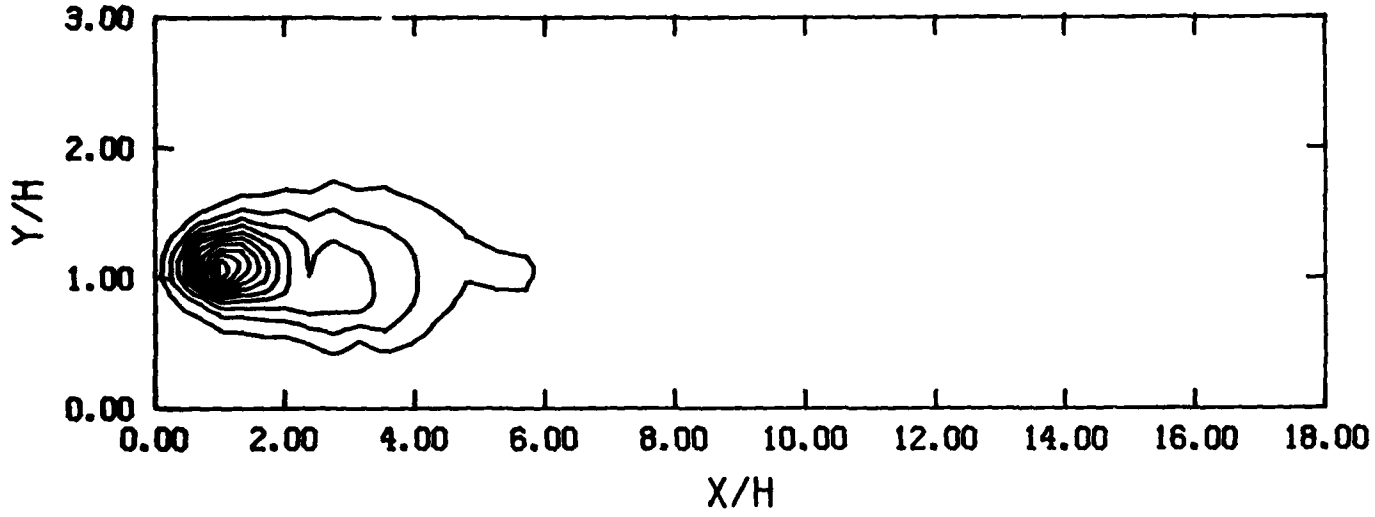

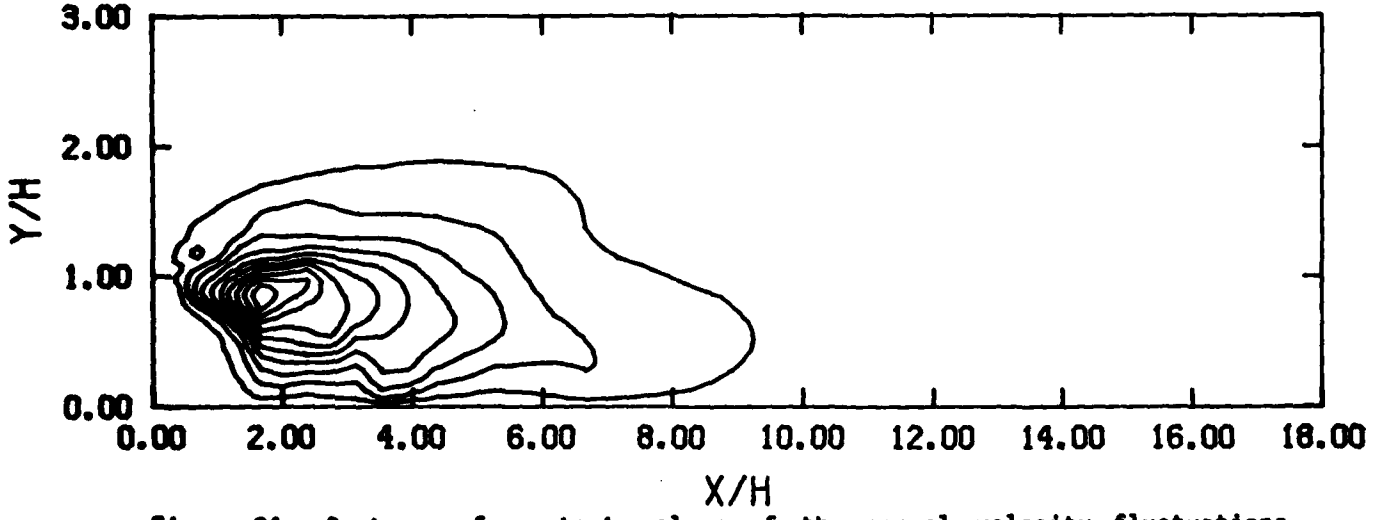

Figure 84. Contours of constant values of the normal velocity fluctuations predicted for the flow of Fig. 81 a. Contribution from the 2-D resolved eddies. Contours shown at an interval of 0.006 U_0^2 from 0 to a maximum value of 0.06 U_0^2. b. Contribution from the 3-D modeled turbulence. Contours shown at an interval of 0.003 U_0^2 from 0 to a maximum value of 0.03 U_0^2.

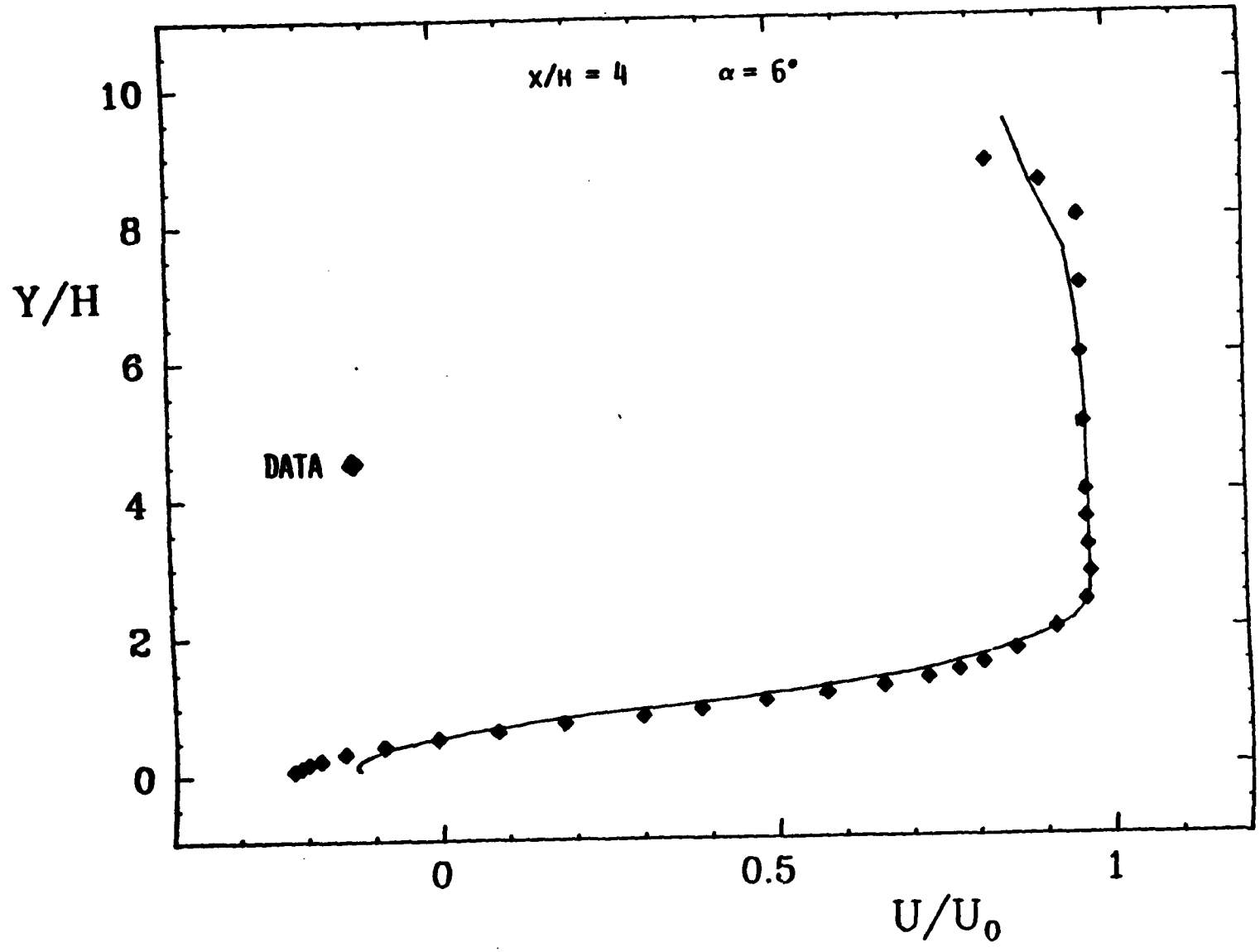

Figure 85. Mean velocity profile at one station downstream of the backward facing step with a six degree angle to the wall opposite the step, Case 0242.

PREDICTIVE CASE P2

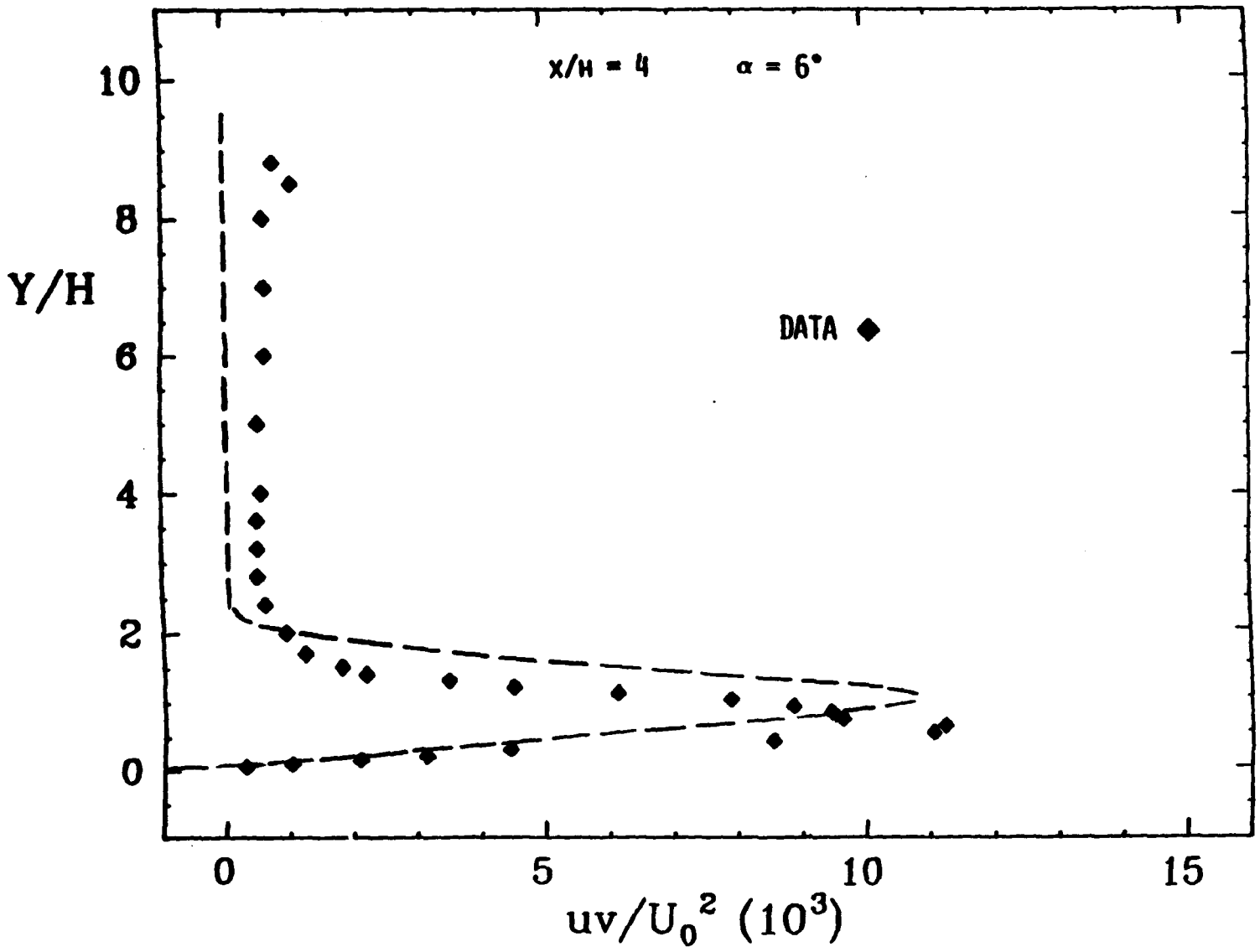

Figure 86. Mean shear stress profile at the same station as given in Fig. 85.